A DETERMINATION OF THE ^{27}SI(P,γ) REACTION RATE USING ITS MIRROR AND ITS IMPORTANCE IN X-RAY BURST NUCLEOSYNTHESIS

A Dissertation

by

ALEXANDRA ELENA SPIRIDON

Submitted to the Office of Graduate and Professional Studies of
Texas A&M University
in partial fulfillment of the requirements for the degree of

DOCTOR OF PHILOSOPHY

Chair of Committee,	Robert E. Tribble
Committee Members,	Carl A. Gagliardi
	Che-Ming Ko
	Charles M. Folden III
Head of Department,	Peter McIntyre

December 2017

Major Subject: Physics

ABSTRACT

X-ray bursts are the most frequent thermonuclear explosions occurring in the universe and represent one of the sources of heavier element nucleosynthesis. In order to determine how much X-ray bursts influence the abundances of these heavier nuclei there is a need for critical nuclear information such as: nuclear masses, β-decay rates and reaction rates.

Due to this need, the field of experimental nuclear physics has been focusing on developing unstable beams and new or improved indirect methods of studying nuclei and reactions, as well as detection systems of higher capability.

In light of this perspective, the focus of this dissertation was twofold. One part involved performing a low-cost, low-modification upgrade to the Oxford focal plane detector using Micromegas technology. The upgrade was very successful in improving the total energy loss resolution by as high as a factor of 3 and thus improving the particle identification ability of the detector. This leads to an increase in the mass range of nuclei possible to study from A=16 to A=32.

The other part of this dissertation project was aimed at studying the proton-capture reaction ^{27}Si$(p,\gamma)^{28}$P using an experimental indirect method called the Asymptotic Normalization Coefficient method. This reaction is part of the thermonuclear runaway network of an X-ray burst suggested by the theoretical models. The spectroscopic factor of ^{28}P was evaluated for the first time in literature at $S_{2s_{1/2}} = 1.11 \pm 0.56$. The direct capture reaction rate was found to be in agreement with the theoretical predictions, and it was confirmed experimentally that at astrophysical energies, the non-resonant component is overwhelmed by the contributions of the resonances.

DEDICATION

To my autistic brother, Cristian. I sacrificed too many years. I should have been there for you and I didn't want it to be for nothing.

ACKNOWLEDGMENTS

I would like to start by expressing my sincere gratitude to my advisor, Prof. Robert Tribble. When he accepted me as his student, he gave me the chance to find a direction at a point in my life when I couldn't see one. I am grateful for his support and especially his patience through the many highs and lows of my time as his student. He has provided me with many opportunities to meet other researchers around the world and he has encouraged me in my studies of related fields. It has been a pleasure working with him.

I would like to convey my thanks to Prof. Carl Gagliardi, Prof. Che-Ming Ko and Prof. Charles Folden for giving up time to be in my committee and for their advice and input to this work, as well as to Prof. John Hardy for agreeing to substitute during my defense.

Dr. Livius Trache has been an appreciated mentor and a pillar of support. I am thankful for the hours he spent patiently instructing me and answering my questions, as well as his help with this work and his strong encouragement in completing my study.

I would like to express my gratitude to Prof. Florin Carstoiu for his help and advice on the analysis of the heavy-ion elastic scattering. I am sincerely thankful to Dr. Emmanuel Pollacco for his guidance and his teachings about Micromegas technology. Additionally, I would like to express my gratitude to the Micromegas groups at CEA Saclay and CERN for their help with the detector. Without them the upgrade wouldn't have been possible.

I would also like to thank the members of the RET group for their help with setting up the experiments that were needed for this work and with the long periods of measurements, specifically Dr. A. Saastamoinen, Dr. B. Roeder, Dr. M. Dag and Mr. R. Chyzh. Special thanks go to former member, Dr. V. Goldberg, for all his advice and general support. Additionally, I must thank the DHY group for their assistance with the experimental setup on the multipole-dipole-multipole (MDM) spectrometer and for sharing their significant

experience in working with the equipment, in particular Dr. Y.-W. Lui and Dr. J. Button.

I would like to convey my deep appreciation to the Cyclotron Institute support staff, the cyclotron operation group, the machine shop staff and Mr. S. Molitor, for their help with the work behind this project and their assistance during all my time here.

Last, but not least, I am deeply grateful towards Prof. Sherry Yennello, Ms. Sharon Jeske and Ms. Paula Barton. Their help and support made it possible for me to return and finish my degree.

CONTRIBUTORS AND FUNDING SOURCES

Contributors

This work was supported by a dissertation committee consisting of Professor Robert E. Tribble [advisor], Professors Carl Gagliardi and Che-Ming Ko of the Department of Physics and Astronomy and Professor Charles Folden of the College of Science. The data analyzed for Chapters 4 and 5 was collected with assistance from Antti Saastamoinen, Brian Roeder, Murat Dag and Roman Chyzh.

All other work conducted for the dissertation was completed by the student independently.

Funding Sources

Graduate study was supported by a research assistantship from Cyclotron Institute and Texas A&M University. The dissertation work was funded in part by the US DOE under Grants DE-FG02-93ER40773 and DE-NA0001785.

TABLE OF CONTENTS

Page

LIST OF FIGURES

FIGURE Page

LIST OF TABLES

1. INTRODUCTION

Nuclear astrophysics is the field of study focused on nuclear processes occurring under stellar conditions and their influence on nucleosynthesis and energy production in stars and stellar explosions [3]. As the name states, nuclear astrophysics relies heavily on the fields of nuclear physics, astronomy and astrophysics.

Nuclear physics provides necessary information on isotopic abundances, masses, half-lives and nuclear reaction cross-sections. The field of astronomy contributes with observational data related to the various celestial bodies, such as positions, luminosity, motion, and radiation spectra. Last, but not least, astrophysics uses spectral measurements and the laws of physics and chemistry to estimate elemental or isotopic abundances and to formulate theories on stellar and galactic evolution [4].

The world around us is made of atoms. In turn, each atom consists of a nucleus, made of neutrons and protons, surrounded by electrons. Atomic nuclei, or nuclides, are classified in a two-dimensional chart according to the number of neutrons and protons. Figure 1.1 shows the chart of nuclides that have been observed until now [5].

Those nuclides that are naturally occurring in our universe were created through various processes of nucleosynthesis occurring during Big-Bang Nucleosynthesis (BBN), as well as inside stars, on the surface of them or even in the regions between stars [6]. It is important to understand these different processes and where they occur in order to interpret correctly the nuclide abundances obtained through various sources including, but not limited to, the observational data collected by the many detectors pointed at the sky.

For example, Figure 1.2 shows the distribution of abundances in the Solar System, plotted as a function of the mass number. The data for this plot was obtained mostly from observations of the solar photosphere and from the analysis of certain meteorites,

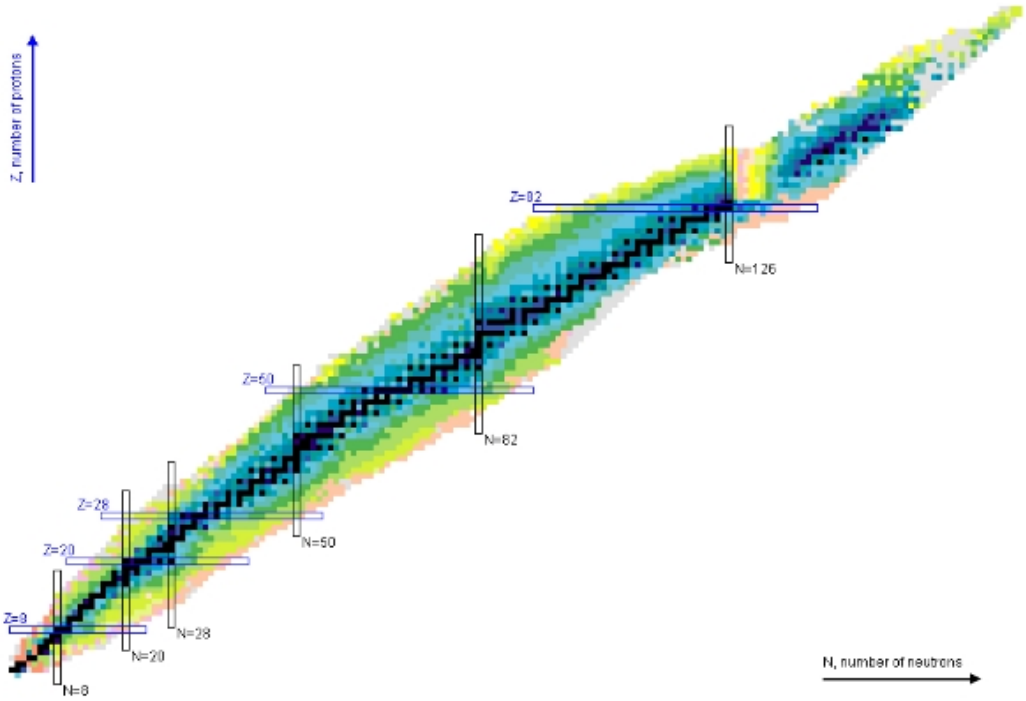

Figure 1.1: The chart of nuclides. Stable nuclei are indicated in black. (print-screen taken from [5])

called CI carbonaceous chondrites. It can be seen that H and He are the most abundant nuclides. In general, the behavior of the distribution is a decreasing one with increasing mass number. But this is not smooth and there are a number of exceptions. Li, Be and B are extremely under-abundant with respect to their neighbors, whereas the Fe region exhibits a pronounced peak. Smaller peaks appear for A $\geq$ 100 in either the odd-A or even-A distributions, or in both. This complicated pattern has generated a number of debates over the years regarding its causes [7].

The current assumption is that the nuclides in these regions of maxima and minima can be attributed to specific mechanisms of nucleosynthesis. As such, these abundances offer powerful clues to stellar evolution, as well as the evolution of the Universe as a whole. It is thought that all of the ^{1}H and most of the ^{2}H, ^{3}He and ^{4}He, were produced in the Big Bang. Figure 1.3 shows the most important reactions involved in BBN. In addition to these four

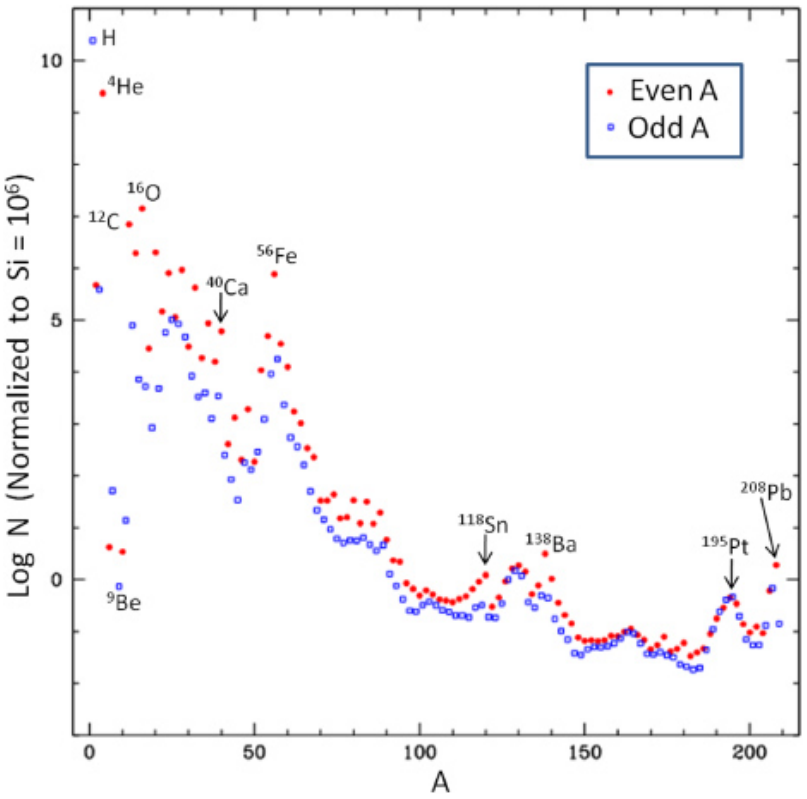

Figure 1.2: The distribution of nuclide abundances in the Solar System. [7]

isotopes, the reaction network of the Big Bang also produces ^{7}Li. It is widely accepted now that nuclei heavier than that are all produced in stars [8].

Following the Big Bang and an initial cooling stage, stars are born in large clouds of interstellar gas through gravitational contraction. During this process, temperature and density increase until they reach a critical point where thermonuclear fusion begins. A star exists in thermodynamic equilibrium when the gravitational force is balanced by the internal, thermal pressure generated by nuclear reactions occurring inside [7].

Thermonuclear fusion occurs in stages, called *burning stages*. In each stage, the lighter nuclei fuse in order to produce heavier ones, thereby changing the composition of the gas. When most of the initial 'fuel' is consumed gravitational contraction begins again, leading to an increase in temperature and density. Once the critical values are reached, the next

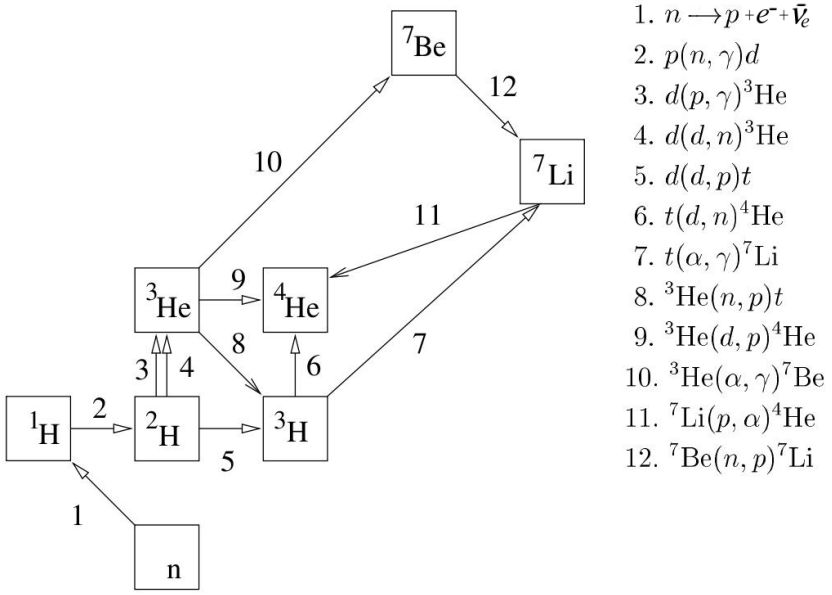

Figure 1.3: Diagram of the most important reactions occurring during BBN. (figure adapted from Ref. [9])

burning stage begins, where the previously produced nuclei, the 'ashes', start fusing into heavier ones. The number of burning stages, and shells, depends on the initial mass of the star but the maximum possible number is 6: hydrogen, helium, carbon, neon, oxygen and silicon burning. By the final stage of thermonuclear fusion, the star gains an 'onion' structure as shown in Figure 1.4.

The first stage, *hydrogen burning*, is the process in which four ^{1}H nuclei fuse into one ^{4}He nucleus. Each such transformation releases an energy of 26.7 MeV independent of the details involved in the process. There are 2 main methods of production of ^{4}He that occur in this stage: the pp-chains and the CNO-cycles.

The three reaction chains referred to as *pp-chains* are shown in Figure 1.5, (a). Each sequence starts from the same reaction, $p(p, e^+\nu)d$, and ends with the production of ^{4}He. The four sets of reactions called *CNO cycles* are shown in Figure 1.5, (b).

The rate of occurrence for each method depends on the temperature, T, of the stellar

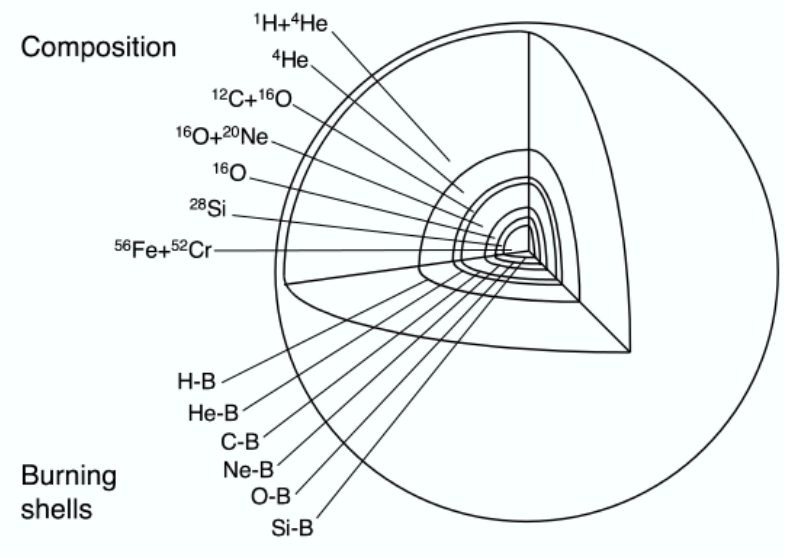

Figure 1.4: The 'onion' shell structure of a massive star. Top-left shows shell labels according to their respective 'ashes'. Bottom left shows the 'fuel' burning in each stage, i.e. H-B for hydrogen burning. [8]

gas. The slowest reaction in the pp-chains is the weak interaction $p(p, e^{+}\nu)d$ and its rate is proportional to T^4 [6]. In the CNO cycles, the slowest reaction is the electromagnetic interaction $^{14}\mathrm{N}(p,\gamma)^{15}\mathrm{O}$ and its rate is proportional to T^{20} [6]. As such, stars like the Sun ($M \approx 1.5\ M_{Sun}$) burn their hydrogen mainly through the pp-chains. Whereas, stars that are heavier and have a higher core temperature will consume their hydrogen through the CNO-cycles. In both cases, the temperature range is $0.015\ \mathrm{GK} \leq T < 0.06\ \mathrm{GK}$.

Theoretical predictions state that in order for a star to reach this first burning stage, its initial mass must be at least $0.08\ M_{Sun}$. If the mass is lower than that then the star ends its evolution as a brown dwarf, when electron degeneracy sets in balancing the gravitational contraction. The ashes of the hydrogen burning stage consist mainly of helium. A star that maintains hydrostatic equilibrium by burning hydrogen at its core is called a *main-sequence star* [8].

When all the hydrogen fuel is consumed, gravitational contraction begins again, caus-

pp1 chain	pp2 chain	pp3 chain
$p(p,e^+\nu)d$	$p(p,e^+\nu)d$	$p(p,e^+\nu)d$
$d(p,\gamma)^3He$	$d(p,\gamma)^3He$	$d(p,\gamma)^3He$
$^3He(^3He,2p)\alpha$	$^3He(\alpha,\gamma)^7Be$	$^3He(\alpha,\gamma)^7Be$
	$^7Be(e^-,\nu)^7Li$	$^7Be(p,\gamma)^8B$
	$^7Li(p,\alpha)\alpha$	$^8B(\beta^+\nu)^8Be$
		$^8Be(\alpha)\alpha$

(a)

CNO1	CNO2	CNO3	CNO4
$^{12}C(p,\gamma)^{13}N$	$^{14}N(p,\gamma)^{15}O$	$^{15}N(p,\gamma)^{16}O$	$^{16}O(p,\gamma)^{17}F$
$^{13}N(\beta^+\nu)^{13}C$	$^{15}O(\beta^+\nu)^{15}N$	$^{16}O(p,\gamma)^{17}F$	$^{17}F(\beta^+\nu)^{17}O$
$^{13}C(p,\gamma)^{14}N$	$^{15}N(p,\gamma)^{16}O$	$^{17}F(\beta^+\nu)^{17}O$	$^{17}O(p,\gamma)^{18}F$
$^{14}N(p,\gamma)^{15}O$	$^{16}O(p,\gamma)^{17}F$	$^{17}O(p,\gamma)^{18}F$	$^{18}F(\beta^+\nu)^{18}O$
$^{15}O(\beta^+\nu)^{15}N$	$^{17}F(\beta^+\nu)^{17}O$	$^{18}F(\beta^+\nu)^{18}O$	$^{18}O(p,\gamma)^{19}F$
$^{15}N(p,\alpha)^{12}C$	$^{17}O(p,\alpha)^{14}N$	$^{18}O(p,\alpha)^{15}N$	$^{19}F(p,\alpha)^{16}O$

(b)

Figure 1.5: (a) The pp-chains. (b) The CNO-cycles. [8]

ing an increase in temperature and density. If the initial mass of the star is less than 0.4 M_{Sun}, then the star eventually evolves into a red dwarf. If the initial mass is larger than 0.4 M_{Sun}, then the temperature and density can reach critical values of $\sim$0.1 GK and 10^3 g/cm^3, respectively, and *helium burning* begins. Two sets of reactions dominate this stage of stellar nucleosynthesis. The first is called the *triple-α reaction* because it converts ^{4}He into ^{12}C:

$$^4He + ^4He \rightarrow ^8Be$$
$$^8Be + ^4He \rightarrow ^{12}C$$

This path proceeds through the unstable nucleus ^{8}Be and is inhibited by the short lifetime of ^{8}Be ($\sim 10^{-16}$ s). Despite that, the temperature and density conditions allow for

a small abundance of ^{8}Be to build up and for the second reaction to occur. This set of reactions is responsible for most of the ^{12}C produced in the universe.

The second 'set' is actually the reaction $^{12}C(\alpha,\gamma)^{16}O$. Once the ^{12}C nuclei start to build up, this reaction starts to occur, further consuming ^{4}He and competing with the triple-α reaction. As such, the ashes of the helium burning stage consist mainly of ^{12}C and ^{16}O.

Further stellar evolution will depend again on the initial mass of the star. If it exceeds 9 M_{Sun}, the subsequent stage of gravitational contraction will lead to the initiation of *carbon burning* and produce ashes consisting mainly of ^{20}Ne. If the mass is insufficient, the star's evolution will end in a carbon-oxygen white dwarf. Similarly, in order for *neon burning* to start, the initial mass of the star needs to be $\sim$11 M_{Sun}. If the mass is lower than this threshold then the star will eventually become an oxygen-neon white dwarf and stop evolving [8].

The result of the neon burning stage is the production of ^{16}O and ^{24}Mg which will fuel *oxygen burning*. Theory predicts that a mass of $\sim$11 M_{Sun} is enough to complete this stage as well, producing mainly ^{28}Si, and even proceed to the last of the burning stages, *silicon burning*. The ^{28}Si nuclei are consumed mainly by (γ,α) and (α,γ) reactions. The α-particles produced in the photo-nuclear process can then be captured by other silicon nuclei to produce higher mass compounds. Other processes contribute to the complex reaction network until the products reach the tightly-bound ^{56}Fe and ^{64}Ni, where higher mass nucleosynthesis stops.

At the end of the Si-burning stage, the star has a core of iron and nickel nuclei and there is no further thermonuclear fusion occurring as it produces no further energy. In that situation, the thermodynamic equilibrium is broken and gravitational contraction restarts. When it reaches a critical point, the star becomes unstable and the core starts to collapse. As that happens, the iron nuclei are photo-disintegrated and electrons are removed from

the gas through electron capture. Both processes speed up the collapse leading to a massive explosion. The star is destroyed, leaving behind either a neutron star or a black hole [3]. Figure 1.6 summarizes the different evolutionary paths available to protostars depending on their starting mass.

It can now be seen how the nuclear processes occurring inside stars take the basic building blocks produced in the Big Bang and transform them into a range of heavier nuclei that reach the iron region of the chart of nuclides. But there is still the question of how, where and in what circumstances the species beyond iron are made.

The first theories regarding that were published in 1957 by Burbidge, Burbidge, Fowler and Hoyle, who proposed a number of nuclear processes for heavy nucleosynthesis and their potential locations [10]. These can be roughly split into two categories, those that produce neutron-rich nuclei and those that produce proton-rich nuclei.

On the neutron-rich side of the nuclide chart, there are two processes that lead to nuclei heavier than iron: the s-process (slow) and the r-process (rapid). Both involve the capture of neutrons by preformed seed nuclei. The difference between the two processes comes from the timing, slow or rapid, between successive captures relative to the typical β-decay times of the nuclei involved. Due to this, the theorized sites of occurrence are also different. The s-process is thought to take place during helium burning, in AGB (asymptotic giant branch) stars. Whereas for the r-process there are two working models: neutron star mergers and core-collapse supernovae [6].

In contrast, production of heavier nuclei on the proton side of the chart is governed by two completely different processes: the rp-process and the γ-process. The *rapid proton (rp)* process consists of successive proton capture reactions, interspersed with the occasional β^+-decays and e^- captures. This method of synthesis takes place as long as the Coulomb barrier of a nuclide allows the process to take place. When the barrier becomes too high, synthesis stops. Or, if the temperature is high enough, the γ-process takes over.

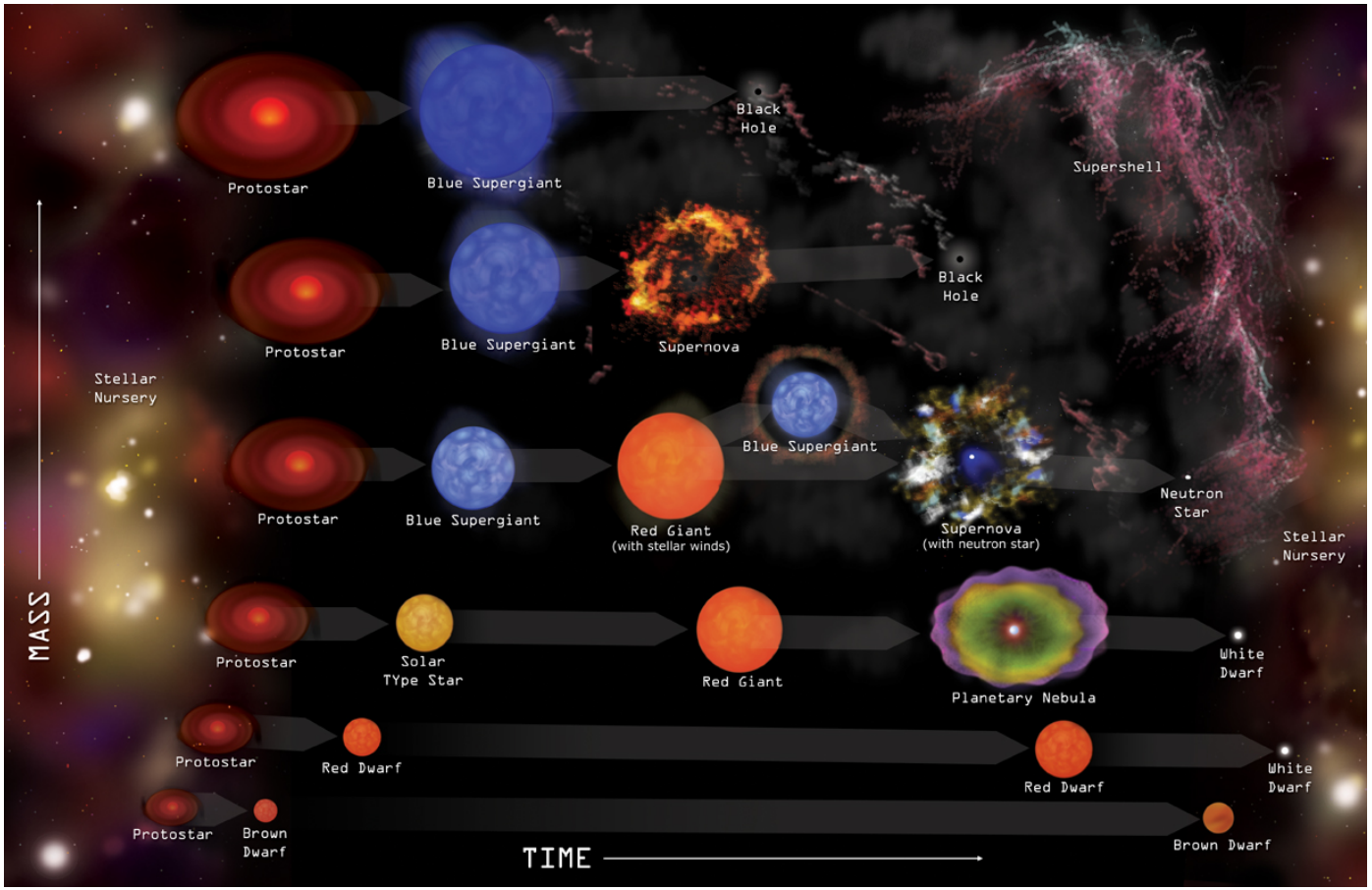

Figure 1.6: Stellar evolution depending on the initial mass of a star. [11]

As the name indicates, the latter process consists of photo-nuclear reactions, such as (γ, α) and (γ, n). In order for these processes to occur, they need a high-temperature, hydrogen-rich environment like the ones created when matter accretes on the surface of a (1) neutron star or a (2) white dwarf, as well as in (3) type I or II supernovae [6].

Of interest to the subject of this dissertation is the first case. In binary systems consisting of a neutron star and a main sequence (MS) companion, matter transfers from the MS star and accumulates on the surface of the neutron star. Due to the stage in evolution of the companion, the transferred material usually consists of H, He or both. As this material is gathered onto the neutron star, it is subjected to the star's intense gravitational field. The matter gradually becomes compressed, leading to an increase in both density and temperature and consequently triggering a thermonuclear runaway. The culmination of this chain of reactions is an explosive event called an X-Ray Burst (XRB) (Figure 1.7) [12].

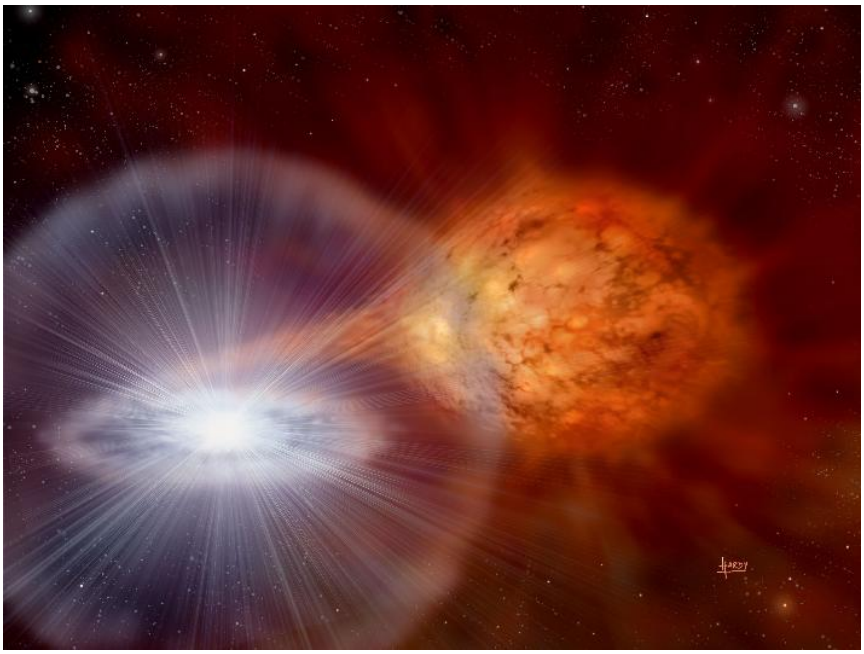

Figure 1.7: An artist's rendition of the X-Ray Burst phenomena. [13]

The first XRB was observed, and identified as such, in 1975 by the Astronomiche Nederlandse Satelliet [14]. Over the last 42 years, 108 burst sources have been identified [15]. XRBs are classified into type I and type II bursts according to their characteristics, the specific burst profile and the proposed mechanism of production. *Type I* bursts are thought to be associated with thermonuclear instabilities and are currently the most numerous of the two types. The profile of a type I XRB shows a rapid rise in luminosity followed by a slow decline. The duration of the burst can be anywhere between $\sim$10 s and several minutes, the frequency of occurrence can vary from hours to days and the energy released can be on the order of 10^{39} ergs. *Type II* bursts are linked to accretion instabilities and are much rarer to occur. The luminosity profile of a type II XRB shows a rapid rise as well as a rapid decline, without a gradual decay from peak luminosity. This type of burst lasts between $\sim$2 s and $\sim$700 s, with an interval from 7 s to 1 h between successive bursts [12].

Type I XRBs were first associated with thermonuclear runaways by Woosley and Taam, in 1975. Their model, called the *thermonuclear flash model*, states that the matter from the MS star is first heated to 0.1-0.2 GK by the impact with the surface of the neutron star [16]. Further accretion eventually leads to a critical level of temperature and density, at which point the bottom layer of accreted matter becomes unstable and the thermonuclear runaway is triggered. The maximum temperature and density that can be reached before the trigger occurs are thought to be T $\sim$ 1-2 GK and $\rho \sim 10^6$ g/cm^3 [17]. Different accretion rates lead to XRBs with different behavior and characteristics.

Creating accurate models of these bursts is particularly difficult. One part of the challenge comes from the necessity of detailed, computationally intensive hydrodynamic studies. Another part comes from the sheer extent of the nucleosynthesis simulations, which involve complex reaction networks including several hundreds of isotopes and several thousands of nuclear processes. And yet another contributor to the difficulty is the lack of experimental nuclear physics information related to these reaction networks, such as

Q-values, decay times and reaction rates [17].

There are different types of models according to how each deals with these issues. One category of models relies on parametrized one-zone calculations and has been in use since 1981 [18]. These models use a set of parameters (T, ρ, X) to characterize a single layer of the envelope, where T is the temperature, ρ is the density and X is a composition array describing the fractional concentration of each isotope. The thermodynamic quantities are usually determined through semi-analytical models, or are sometimes extracted from 1-D hydrodynamic models [12, 19]. These models have a very simplified perspective of the physical conditions governing neutron star envelopes, but they reduce significantly the computational time that other, more complex, models require.

Recently, advances in computer processing power have enabled researchers to rely more on 1-D hydrodynamic models for XRB nucleosynthesis calculations. These models work on the assumption that the bursts occur uniformly over a spherical shell and are limited by their treatment of the manner in which thermonuclear runaways are initiated (presumably as point-like ignitions) and propagate.

The relevant types of reaction sequences in XRBs have been discussed in various studies (see [18,20–24]). It was found that the main reactions are (p, γ), (α, γ) and (p, α). Just as important are the β-decay rates between the valley of stability and the proton drip line. These reaction rates are important up to the endpoint of the rp-process [25].

A point of intense debate has been identifying which reaction rates are critical in XRBs. One method to determine this would be to test each of them one by one. However, that would be extremely time consuming as there are a large number of permutations that would need to be tested. Instead, different research groups used different methods of 'guessing'. Woosley *et al.* [26] changed groups of decay rates and narrowed the rates down to several important candidates. Fisker *et al.* ([27, 28]) relied on 'inspired guesses' and found individual important rates. Amthor *et al.* [29] used a one-zone model and individually varied

a large number of reaction rates with the intent of verifying 'one-zone'-candidates with a multi-zone model. Using Monte Carlo methods, L. F. Roberts varied random groups of reaction rates and similarly identified the most significant candidates for later verification with multi-zone models [25, 30]. However, to date, there have been no published nuclear abundances predictions from multi-zone models.

The variety in the reactions proposed in these studies shows that it is very important to reach an accurate definition of the astrophysics theory behind modeling the X-Ray Burst phenomena, as different models yield different critical reactions. At the same time, these reaction rates need to be determined with lower uncertainties in order to constrain the model.

Determining such reaction rates experimentally has been a motivation for research studies for quite some time. The main issue in this regard is that the nuclei involved in XRBs are almost all unstable with short lifetimes. Some of the reactions can and have been studied reliably through indirect methods with stable beams. Most of them, however, require the use of accelerated unstable beams. In light of this, a number of facilities worldwide have started, and in some cases, completed upgrades to produce such beams. In cases where these are unavailable, research groups have continued to use indirect methods and/or are designing more efficient detection systems [31].

The Cyclotron Institute at Texas A&M University is part of this group of facilities. Its currently in-progress T-REX (Texas Re-accelerated EXotics) upgrade will provide high-quality re-accelerated secondary beams. In addition and because of the future availability of such beams, many of groups at Cyclotron Institute have also started developing better detection systems or making improvements to existing ones.

As such, the focus of this dissertation project was two-fold. The main part involved performing an upgrade to the existing so-called Oxford focal plane detection system, in use by the Nuclear Astrophysics group at Cyclotron Institute. The goal was to improve

the energy loss resolution of the detector in order to expand its particle identification range beyond the nuclide mass A=22. Using the increasingly popular Micromegas technology, it was possible to achieve this aim at lower cost, faster and with minimal changes to the existing detection components of the Oxford system.

The second part of this dissertation was focused on using the upgraded Oxford detector to study an astrophysical test-case reaction. Given that one of the first unstable light beams to be produced with the T-REX will be ^{27}Si, the reaction that was chosen was $^{27}\mathrm{Si}(p,\gamma)$.

This proton-capture reaction was one of the reactions considered by various groups as important in explosive nucleosynthesis. The reaction rate was first estimated by Wallace and Woosley in 1981 [18], then by Wiescher *et al.* in 1986 [32]. In both studies, the XRB models were run for a temperature range of 0.1-0.5 GK and density 5×10^3 g/cm^3, conditions required for nova explosions. The rates agreed at higher temperatures and both papers concluded that, at its estimated rate, the reaction had a significant contribution to the network flow [32] and recommended measurements with radioactive beams.

In 1999, Iliadis *et al.* used a method based on the reaction Q-value to find critical reactions in XRBs. In their study, they performed a nuclear reaction network calculation for explosive hydrogen burning. The result is shown in Figure 1.8, where the different colors indicate short-lived nuclei with proton-capture reaction Q-values in different ranges. The assumption with this method was that if the (p,γ) reaction has high enough Q-value (> 2 MeV, green, blue and purple squares) then the level density in the compound nucleus is high enough that the statistical model of nuclear reactions can be applied to estimate stellar reaction rates, therefore bypassing the need for experimental data. If the Q-value is very small (< 0.5 MeV, red squares) then the inverse (γ,p) reaction becomes important at the high temperatures typical of explosive hydrogen burning [2].

In this situation, the nucleosynthesis path depends mainly on the ratio of forward (proton capture) to backward (photo-disintegration) reaction rates. This ratio is determined by

the (p, γ) reaction Q-value and not by the particular reaction cross section [2].

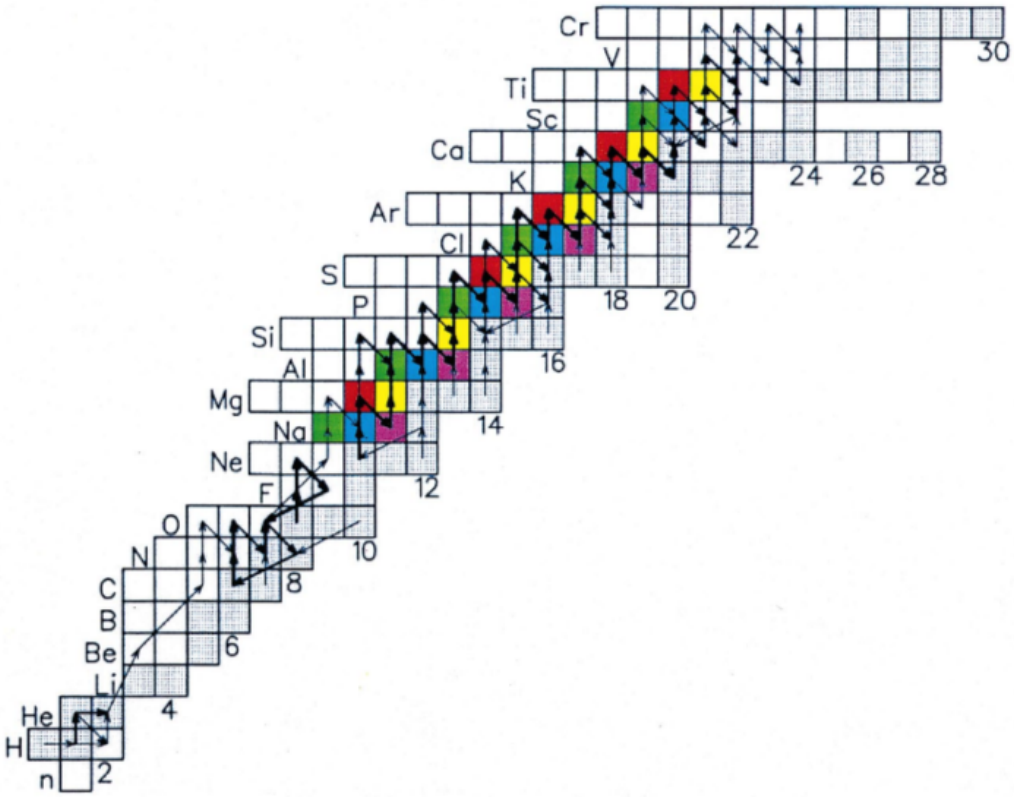

Figure 1.8: Simulated nuclear reaction network for explosive hydrogen burning. Nuclides are color coded according to proton capture Q-value: red(Q<0.5 MeV), yellow(0.5<Q<2 MeV), green(2.5<Q<3.5 MeV), blue(3.5<Q<5.5 MeV) and purple(5.5<Q<7.5 MeV). Additionally, the gray squares represent stable nuclei, while the whites ones indicate unstable nuclei. [2]

The remaining nuclei, indicated by the yellow squares, have (p, γ) Q-values between 0.5 MeV and 2 MeV. As such, the two assumptions mentioned above cannot be applied here. These nuclei are ^{23}Mg, ^{27}Si, ^{31}S, ^{35}Ar, and ^{39}Ca. Iliadis *et al.* focused their study on estimating the proton capture reactions involving these nuclei and determining their influence on the outcome of XRB nucleosynthesis. The ^{27}Si$(p, \gamma)^{28}$P reaction rate was estimated using theoretical calculations and experimental information on the ^{28}P energy

levels. For T > 0.07 GK, the results agreed with the ones found by Wiescher *et al.*, as can be seen in Figure 1.9.

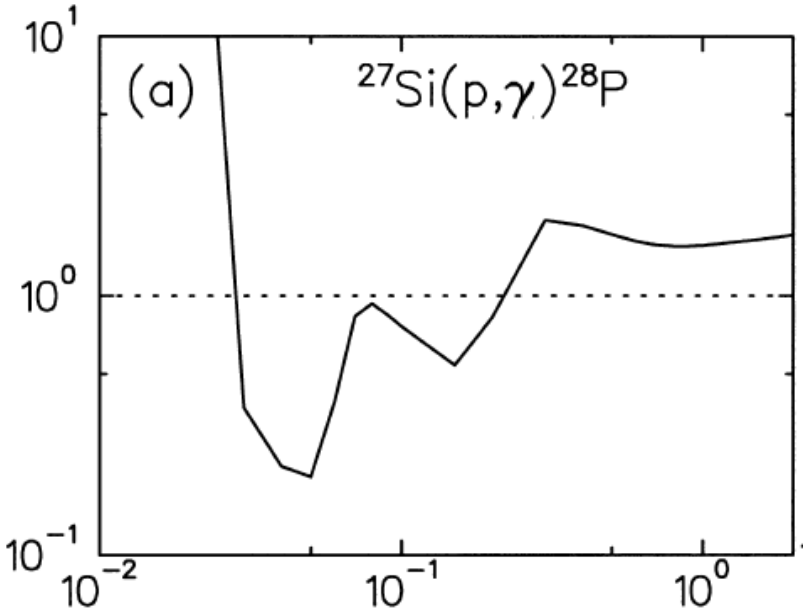

Figure 1.9: Ratio between rate found by Iliadis and rate found by Wiescher as a function of stellar temperature (GK). [2]

This rate was used in an XRB model with temperature range of 0.2-1.5 GK and density 10^7 g/cm^3. It was found that varying the rate within ±σ produced no noticeable effect on the final XRB abundances. A much larger variation, of a factor of 10, produced a change in the final abundances of less than 40%.

A later study by Parikh *et al.* used the same estimated reaction rate as above but different burst models. They reached the same result regarding final abundances but found that an increase in the ^{27}Si(p,γ) rate by a factor of two did produce a corresponding change in the overall nuclear energy production [33].

All the theoretical estimations of the ^{27}Si(p,γ) rate, mentioned above, assumed that

the non-resonant component of the reaction rate was negligible. As a ^{27}Si beam is not yet available, the resonant reaction rate could not be studied. Instead, the present study was focused on providing an experimental determination of the direct capture rate for the ^{27}Si(p,γ) reaction to compare with the theoretical predictions, and more importantly on demonstrating that the upgraded detection system is capable of distinguishing nuclei of masses 27 and 28.

This dissertation is structured in 6 chapters. Chapter 1 presents an introduction to the astrophysical concepts in stellar nucleosynthesis and a summary of the current research related to the topic of this study. Chapter 2 will provide the necessary theory regarding nuclear reactions, the indirect experimental method used, called the Asymptotic Normalization Coefficient (ANC) method, and the calculation models involved in obtaining the results. Information on the experimental set-up and procedures will be presented in Chapter 3. It will also include a detailed description of the upgrade of the detection system. Chapter 4 will present the tests done for the upgrade and the corresponding results. The analysis steps for the astrophysical study and the results of the ANC calculations will be shown in Chapter 5. Last, chapter 6 will present the ^{27}Si(p,γ) reaction rate results and conclusions.

2. THEORY

This chapter contains descriptions of the basic concepts in nuclear physics and related formulas relevant to this study. Additionally, the last section of the chapter will present the sequence of calculation steps taken to reach the final result.

2.1 Nuclear Reactions

A typical nuclear reaction, where the projectile a interacts with the target A to give two products b and B, can be written as:

$$a + A \rightarrow b + B\,, \tag{2.1}$$

or in a shorter form as:

$$A(a,b)B\,. \tag{2.2}$$

Most commonly, the notation (A,a) denotes the entrance channel of the reaction and (b,B) the exit channel. For simplicity, in this chapter they will be denoted as α and β, respectively.

2.1.1 Conservation laws and basic kinematics

There are several conservation laws that determine the exit channel of the reaction [34]. These laws are:

- Conservation of total energy:

$$E_A + m_A c^2 + E_a + m_a c^2 = E_b + m_b c^2 + E_B + m_B c^2\,, \tag{2.3}$$

where $E_i = \frac{1}{2} m_i v_i^2$ represents the non-relativistic kinetic energy and $m_i c^2$ represents

the mass-energy. This equation can be rewritten as:

$$E_\alpha + Q = E_\beta \, . \tag{2.4}$$

Here, Q is called the 'Q-value' of the reaction and is determined from the mass-energies:

$$Q = (m_A + m_a - m_b - m_B)c^2 \, . \tag{2.5}$$

If $Q > 0$ then the reaction is called exothermic and if $Q < 0$ then the reaction is endothermic.

- Conservation of linear momentum:

$$\sum \vec{p_i} = \sum \vec{p_f} \, . \tag{2.6}$$

- Conservation of total angular momentum:

$$\sum \vec{J_i} + \vec{J}_{rel,i} = \sum \vec{J_f} + \vec{J}_{rel,f} \, , \tag{2.7}$$

where $\vec{J_i}$ and $\vec{J_f}$ represent the angular momenta of the initial and final nuclei and $\vec{J}_{rel,i}$ and $\vec{J}_{rel,f}$ represent the relative angular momenta in the entrance and exit channels.

- Conservation of charge and neutron number: In purely nuclear reactions, this law states that the total number of protons and neutrons in the entrance channel must equal the total number of protons and neutrons in the exit channel.

- Conservation of parity:

$$\pi_A \cdot \pi_a \cdot \pi_{(A,a)} = \pi_b \cdot \pi_B \cdot \pi_{(b,B)} \,. \tag{2.8}$$

The kinematics of a nuclear reaction are determined by the first two laws mentioned above, conservation of energy and conservation of momentum. Most often, the experimental results need to be compared to the theoretical calculations. However measurements are done in the laboratory reference frame, while theory prefers the center-of-mass (C.M.) frame which is fixed and as such more convenient. Kinematics can be used to convert results between the two systems. Figure 2.1 shows the reference frames side by side for the case most commonly found in experiments, where the projectile is an accelerated nuclide and the target is stationary.

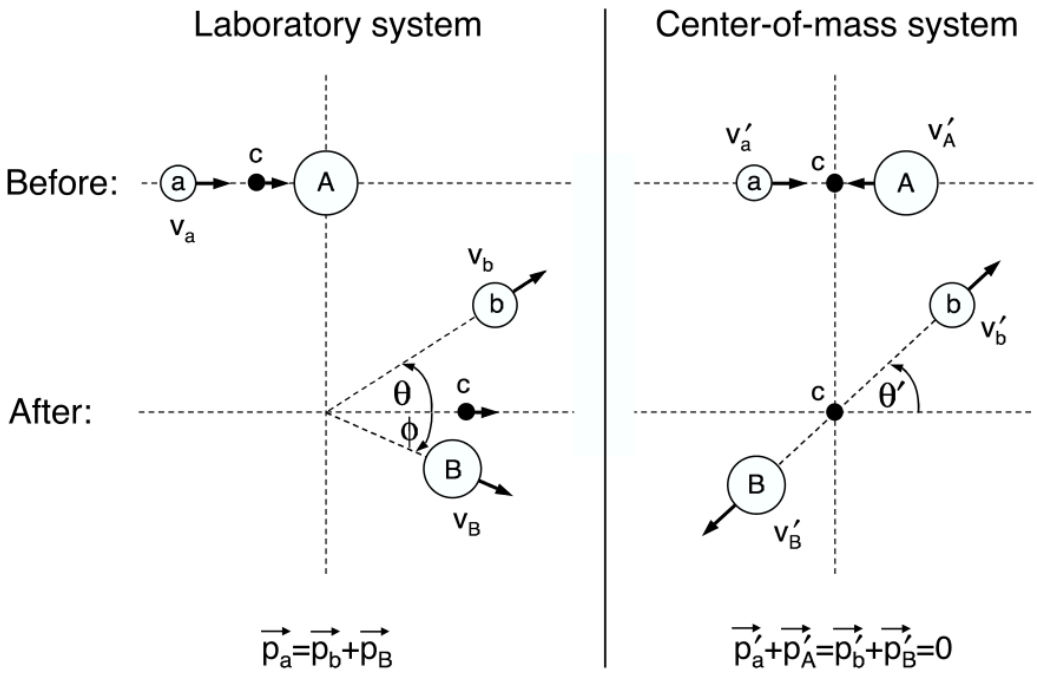

Figure 2.1: Kinematics of nuclear reaction $A(a,b)B$, side by side comparison between the laboratory and center-of-mass system. [8]

To begin with, the velocity of the center of mass, $\vec{V}_{CM}$, is defined as:

$$\begin{aligned}\vec{V}_{CM} &= \frac{m_a\vec{v}_a + m_A\vec{v}_A}{m_a + m_A} \\ &= \frac{m_a}{m_a + m_A}\vec{v}_a \,. \end{aligned} \tag{2.9}$$

The relative velocity of a and A is:

$$\vec{v} = \vec{v}_a - \vec{v}_A \,. \tag{2.10}$$

As such, the energy in the C.M. frame can be written as:

$$E = \frac{1}{2}MV_{CM}^2 + \frac{1}{2}\mu v^2 \,, \tag{2.11}$$

where $M = m_a + m_A$ is the total mass and $\mu = \frac{m_a m_A}{m_a + m_A}$ is called the reduced mass. Relating Eq. 2.11 to the quantities expressed in Eq. 2.3 gives a conversion from laboratory kinetic energy to the C.M. kinetic energy:

$$E^{CM} = \frac{m_A}{M}E_\alpha^{Lab} \,. \tag{2.12}$$

Many experiments involve measurements dependent in some manner on the angle of interaction. Therefore, a conversion between laboratory and C.M. angles is also necessary. This can be extracted from the geometry shown in Figure 2.1:

$$v_b' \cos\theta' = v_b \cos\theta - V_{CM} \tag{2.13}$$

$$v_b' \sin\theta' = v_b \sin\theta - 0 \,. \tag{2.14}$$

From the above two expressions, the relationship between laboratory angle and C.M. angle is derived as:

$$\cos\theta = \frac{\gamma + \cos\theta'}{\sqrt{1+\gamma^2+2\gamma\cos\theta'}}\,, \tag{2.15}$$

$$\text{where } \gamma = \sqrt{\frac{m_a m_b}{m_A m_B}\frac{E_a}{(1+m_a/m_A)Q+E_a}}\,. \tag{2.16}$$

2.1.2 Types of reactions

For an interaction defined by Eq. 2.1, the nuclei A and a are typically in their ground states. Depending on the characteristics of b and B, reactions can belong to one of the following categories.

1. *Elastic scattering* – is written as $A(a,a)A$. The nuclei remain in their ground states but the angle between their outgoing velocities, called scattering angle θ, will change.

2. *Inelastic scattering* – is written as $A(a,a')A^*$. Either or both nuclei can be in an excited state in the exit channel. The Q-value of the reaction is then given by the energy of excitation, $Q = -\epsilon_A$ for endothermic reactions and $Q = \epsilon_A$ for exothermic reactions.

3. *Transfer reaction* – is written as Eq. 2.1 and can be of two types: pick-up and stripping. In a pick-up reaction, the projectile receives one or more nucleons, x, from the target such that $A = B + x$ and $b = a + x$. In a stripping reaction, particle x leaves the projectile a and binds to the target nucleus A to form new nucleus B. The outgoing particles may be in their ground states, or they can be in excited states. The reaction Q-value is given by $S_b^x = S_A^x + Q$, where S_b^x and S_A^x are the separation energies of particle x in b and A [35].

4. *Radiative capture* – is written as $A(a,\gamma)B$. Nuclei a and A form a nucleus by γ emission.

5. *Photo-disintegration* – is the reverse process of the one above.

6. *Breakup reaction* – is written as $A(a,b+c)A$. Nucleus a is broken up into two or more fragments b and c.

In the scope of this thesis, types 1 to 4 are of interest and will be touched upon in more detail.

2.1.3 Experimental cross-section

In a typical experiment, the target-beam interaction $A + a$ is characterized by some potential $V(r)$. The projectile a comes in the form of a beam with an incident flux, $\vec{j}$. Then the outgoing flux of particles b for a specific channel β is counted with a detection setup. The probability of occurrence of this specific channel is described using the concept of cross-section. In particular, the angular distribution of outgoing particles b is usually described by the differential cross-section:

$$\frac{d\sigma_\beta(\Omega)}{d\Omega} = \frac{N_\beta(\Omega,\Delta\Omega)}{\Delta\Omega \cdot n \cdot j}\,, \tag{2.17}$$

where n is the number of scattering centers in the target, $\Delta\Omega$ is the solid angle and $N_\beta(\Omega,\Delta\Omega)$ represents the number of ejectiles scattered inside $\Delta\Omega$. The total cross-section can then be determined by integration over the angular range:

$$\sigma_\beta = \int_{4\pi} d\Omega \left(\frac{d\sigma_\beta(\Omega)}{d\Omega}\right)\,. \tag{2.18}$$

Given that σ is a measure of the total number of incident particles that are deflected by target A, the frame of reference doesn't matter. However, for the differential cross-section

it is necessary to have a conversion between laboratory and C.M. This relation is given by the formulas:

$$\frac{(d\sigma/d\Omega)_{CM}(\theta_{CM})}{(d\sigma/d\Omega)_{Lab}(\theta_{Lab})} = \frac{d(\cos\theta_{Lab})}{d(\cos\theta_{CM})} = \frac{1+\gamma\cos\theta_{CM}}{(1+\gamma^2+2\gamma\cos\theta_{CM})^{3/2}}\,, \tag{2.19}$$

where γ is given by Eq. 2.16. For the data analysis done in Chapter 4, the necessary lab to C.M. conversion factors where determined using a small FORTRAN program called KINE.

2.2 Scattering Theory

In order to determine the cross-section for a reaction like Eq. 2.1, it is necessary to solve the Schrödinger equation that describes the system and find the total wave function. The non-relativistic motion of particle a is described by:

$$(H-E)\Psi = 0\,. \tag{2.20}$$

H is the total Hamiltonian and can be written to describe any channel:

$$H = H_\alpha + T_\alpha + V_\alpha = H_\beta + T_\beta + V_\beta = \ldots \tag{2.21}$$

H_α represents the sum of the intrinsic Hamiltonians for a and A, with:

$$\begin{aligned}(H_a-\epsilon_a)\Phi_a &= 0\\ (H_A-\epsilon_A)\Phi_A &= 0\,,\end{aligned} \tag{2.22}$$

where Φ_X denotes the eigenstates of the intrinsic Hamiltonians and ϵ_X, their respective eigenvalues. Additionally, in Eq. 2.21, T_α is the kinetic energy of their relative motion and V_α describes their mutual interaction. The intrinsic state of channel α is denoted by

$\Phi_\alpha = \Phi_a \Phi_A$ and it satisfies the equation $(H_\alpha - \epsilon_\alpha)\Phi_\alpha = 0$. Eq. 2.20 can be rewritten as:

$$(E - H_\alpha - T_\alpha)\Psi_\alpha = V_\alpha \Psi_\alpha \,. \tag{2.23}$$

If there is no mutual interaction, $V_\alpha = 0$, then Eq. 2.23 becomes:

$$(E - H_\alpha - T_\alpha)\phi_\alpha = 0 \,. \tag{2.24}$$

The solution to the equation above can be written in terms of the internal wave functions from Eq. 2.22 and the eigenfunctions for the kinetic energy operator (which is a plane wave):

$$\phi_\alpha = e^{i\vec{k}_\alpha \cdot \vec{r}_\alpha} \Phi_\alpha \,, \tag{2.25}$$

where $\vec{r}_\alpha$ represents the relative coordinate between nuclei a and A and $\vec{k}_\alpha$ is the wavenumber corresponding to channel α:

$$\vec{r}_\alpha = \frac{1}{a}\sum_1^a \vec{r}_i - \frac{1}{A}\sum_{a+1}^{A+a} \vec{r}_i \tag{2.26}$$

$$h^2 k_\alpha^2 / 2\mu = E_\alpha = E - \epsilon_\alpha \,, \tag{2.27}$$

where a and A in Eq. 2.26 represent the mass numbers of the nuclei with the same name.

In order to determine the component of Ψ corresponding to a reaction with an entrance channel α and an exit channel β, Eq. 2.23 must be multiplied by Φ_β and then integrated over the internal coordinates:

$$(E_\beta - T_\beta)(\Phi_\beta, \Psi_\alpha) = (\Phi_\beta, V_\beta \Psi_\alpha) \,, \tag{2.28}$$

where E_β was defined in Eq. 2.27 and represents the kinetic energy of the relative mo-

tion corresponding to the β channel and the bracket notation denotes integration over all internal coordinates [36]:

$$(\Phi_\beta, \Psi_\alpha) = (\Phi_\beta|\Psi_\alpha) = \int \Phi_\beta^* \Psi_\alpha d(\text{internal coordinates}) \,. \tag{2.29}$$

Denoting the left side of the above equation as $\psi_\beta(\vec{r}_\beta)$, Eq. 2.28 becomes:

$$(E_\beta - T_\beta)\psi_\beta = (\Phi_\beta, V_\beta \Psi_\alpha) \,. \tag{2.30}$$

This equation can be transformed into a more useful form using Green's function:

$$(E_\beta - T_\beta) G_\beta^0(\vec{r}_\beta, \vec{r'}_\beta) = \delta(\vec{r}_\beta - \vec{r'}_\beta) \,. \tag{2.31}$$

Substituting Eq. 2.31 into Eq. 2.30 leads to a solution for ψ_β that can be written as:

$$\psi_\beta(\vec{r}_\beta) = \int G_\beta^0(\vec{r}_\beta, \vec{r'}_\beta)(\Phi_\beta, V_\beta \Psi_\alpha) d\vec{r'}_\beta \,. \tag{2.32}$$

Adding the plane-wave eigenfunctions of the kinetic energy operator (which were also used in Eq. 2.25) leads to the general form:

$$\psi_\beta(\vec{r}_\beta) = e^{i\vec{k}_\beta \cdot \vec{r}_\beta} + \int G_\beta^0(\vec{r}_\beta, \vec{r'}_\beta)(\Phi_\beta, V_\beta \Psi_\alpha) d\vec{r'}_\beta \,. \tag{2.33}$$

Then from Eq. 2.31, one can obtain a solution for G_β^0:

$$\begin{aligned} G_\beta^{0(+)}(\vec{r}, \vec{r'}) &= -\frac{2\mu_\beta}{4\pi\hbar^2} \frac{\exp\left(ik_\beta |\vec{r} - \vec{r'}|\right)}{|\vec{r} - \vec{r'}|} \\ &\xrightarrow[r\to\infty]{} -\left(\frac{2\mu_\beta}{4\pi\hbar^2}\right) \frac{\exp\left(ik_\beta r\right)}{r} \exp\left(-i\vec{k'}_\beta \cdot \vec{r'}\right) . \end{aligned} \tag{2.34}$$

Inserting this expression for G^0_β into Eq. 2.33 and taking into account that for the stated problem, $a + A \rightarrow b + B$, there is no incoming wave in the β channel, one obtains the desired solution for the scattered wave-function in the form of:

$$\psi^{(+)}_\beta(\vec{r}_\beta) \xrightarrow[r_\beta \to \infty]{} -\left(\frac{\mu_\beta}{2\pi\hbar^2}\right) \frac{\exp\left(ik_\beta r_\beta\right)}{r_\beta} \int \exp\left(-i\vec{k}_\beta \cdot \vec{r}\right)(\Phi_\beta, V_\beta \Psi^{(+)}_\alpha) d\vec{r}. \tag{2.35}$$

In the last two expressions, the (+) sign was used to show the outgoing direction of the wave at r$\rightarrow \infty$. From Eq. 2.35, the scattering amplitude is found to be:

$$f_{\beta\alpha}(\theta) = -\frac{\mu_\beta}{2\pi\hbar^2} \int \exp\left(-i\vec{k}_\beta \cdot \vec{r}\right)(\Phi_\beta, V_\beta \Psi^{(+)}_\alpha) d\vec{r}. \tag{2.36}$$

Here, θ denotes the scattering angle, specifically the angle between $\vec{k}_\beta$ and $\vec{k}_\alpha$. A concept often used instead of the scattering amplitude is the transition amplitude, T:

$$T_{\beta\alpha} = \left\langle \phi_\beta | V_\beta | \Psi^{(+)}_\alpha \right\rangle , \tag{2.37}$$

where the angle bracket notation has a similar definition to the one in Eq. 2.29, except the integration is over all coordinates. The set of amplitudes that correspond to different α and β is called the transition matrix, though the terms are often used interchangeably [36].

The scattering cross-section

Having determined an expression for the scattering amplitude, one can now use it to calculate the differential cross-section defined in Eq. 2.17. The flux associated with the wave-function ψ is given by:

$$\vec{j} = \frac{\hbar}{2i\mu}(\psi^* \nabla\psi - \psi \nabla\psi^*) . \tag{2.38}$$

This equation can be used to determine the number of projectiles scattered inside the

solid angle, $\Delta\Omega$:

$$N_\beta(\Omega, \Delta\Omega) = \vec{j}_\beta \cdot \Delta\vec{S} = (\Delta\Omega r_\beta^2)\hat{r_\beta} \cdot \vec{j}_\beta \,. \tag{2.39}$$

At a large distance from the scattering site, the gradient reduces to only the radial component. Using the asymptotic form for ψ at $r_\beta \to \infty$, one obtains:

$$d\sigma = \frac{\mu_\alpha}{\mu_\beta}\frac{k_\beta}{k_\alpha}|f_{\beta\alpha}(\theta)|^2 d\Omega \,. \tag{2.40}$$

A similar formula can also be obtained in terms of the transition amplitude, T:

$$\left(\frac{d\sigma}{d\Omega}\right)_{\beta\alpha} = \frac{\mu_\alpha\mu_\beta}{(2\pi\hbar^2)^2}\frac{k_\beta}{k_\alpha}|T_{\beta\alpha}|^2 \,. \tag{2.41}$$

2.3 The Optical Model Potential

In Eq. 2.37, the transition amplitude has a general form and it depends on knowing, exactly, the wave function $\Psi_\alpha^{(+)}$. This means that it must contain a description of all processes that can occur at a given projectile energy [36]. Such a complete description is extremely difficult to obtain and therefore an approximation of the transition amplitude is more useful.

To that end, it is helpful to introduce a potential $U(r_\alpha)$, called *optical model potential (OMP)*, describing the relative motion in the entrance channel. Given that the nuclear force has a short range, the nuclear part of this potential is expected to depend only on the relative coordinate between nuclei a and A. The choice of $U(r_\alpha)$ is usually a form that best describes the elastic scattering. For the situation where the interaction between a and A is solely described by $U(r_\alpha)$, the optical-model Schrödinger equation is written as:

$$(T_\alpha + U_\alpha - E_\alpha)\chi_\alpha(\vec{r}_\alpha) = 0 \,. \tag{2.42}$$

This is a direct result of substituting $\Psi = \Phi_\alpha \chi_\alpha$ into Eq. 2.23, with χ_α denoting the wave function describing the relative interaction. It should be noted that the number of open exit channels for a reaction depends on the energy of the projectile. At very low energies, only the elastic scattering channel is open. Conservation laws dictate that the particle flux is conserved, which requires a real potential U_α. At higher projectile energies, other exit channels open up (inelastic, transfer, etc...) and thus, some of the flux from the scattering channel is absorbed [36].

As such, $\vec{j}$ is not conserved anymore, which implies a complex form for the optical potential. Furthermore, using Eq. 2.42 and its conjugate, governing χ^*_α, one can find that:

$$\hbar \nabla \cdot \vec{j} = 2 \chi_\alpha \chi^*_\alpha \, \mathrm{Im}\, U_\alpha \, . \tag{2.43}$$

This shows that in order to correctly characterize the elastic scattering when other reaction channels are present, it is necessary to use a complex and negative optical model potential. The equation below shows the general form for the OMP:

$$U(r) = V(r) + i[W(r) + U_S(r)] + U_{SO}(r) + U_C(r) \, , \tag{2.44}$$

where $V(r)$ represents the real part of the potential. This describes the refraction of the incident flux and thus is most important for elastic scattering. The imaginary part may consist of a volume component, $W(r)$, as well as a surface component, $U_S(r)$. The third term in Eq. 2.44, $U_{SO}(r)$ represents the spin-orbit interaction and the last one stands for the Coulomb potential which is included if there are charged particles involved.

However, using the complete formula means that the number of parameters that need to be varied in order to match calculations to experimental data is much larger. This makes the process significantly more complicated and time consuming. For elastic scattering,

it's often possible to neglect the surface and spin-orbit terms leaving only the real and imaginary volume components.

Since the nuclear force is short range, the form of $U(r)$ is generally chosen to be short range and falling rapidly to zero near the surface of the nucleus, similar to the density distribution. The form most commonly used is called the *Woods-Saxon (WS)* potential. Another form that is frequently used is called the *double folding (DF)* potential. Both of these potentials will be described in more detail in the next subsections. Beside these two, other forms have been tried over the years but none were as successful as the WS and DF over a wide range of scattering reactions.

The Woods-Saxon form

Typically, the Woods-Saxon potential is described by the equation shown below:

$$U(r) = -(V f_V(r) + iW f_W(r)) \,, \tag{2.45}$$

where V and W represent the strengths, or depths, of the real and imaginary components of the potential, respectively. The form factor $f_x(r)$ is given by:

$$f_x(r) = \frac{1}{1 + e^{\frac{r - R_x}{a_x}}} \,, \tag{2.46}$$

where $x = V, W$, a_x is called the diffuseness and R_x denotes the nuclear radius. The latter is often parametrized as:

$$R_x = r_x(a^{\frac{1}{3}} + A^{\frac{1}{3}}) \,, \tag{2.47}$$

where a and A indicate the number of nucleons in the projectile and target, respectively, and r_x $\approx$1.2 fm. Sometimes, particularly at low projectile energies, it is necessary to take into account surface-peaked processes (for example, peripheral collisions resulting in

particle transfers). In this situation, the surface term $U_S(r)$ is added and expressed as:

$$U_S(r) = W_S \frac{df_W(r)}{dr} \,. \tag{2.48}$$

As mentioned before, when charged particles are involved, the Coulomb potential must also be included. At large distances, the potential is the standard one between two point charges. Near the target, however, the charge distribution between the two interacting nuclei determines the potential affecting the charged projectile. The easiest assumption to use is that of a uniform distribution. The Coulomb potential can then be written as:

$$U_C(r) = \begin{cases} \frac{Z_a Z_A e^2}{2R_C} \left[3 - \left(\frac{r}{R_C} \right)^2 \right] & r < R_C \\ \frac{Z_a Z_A e^2}{r} & r > R_C \end{cases} \tag{2.49}$$

If the Coulomb and surface are both included and independent geometries are used then the OMP has 10 parameters that have to be varied in order to fit the data. This number is not easy to work with and often the surface term is either neglected (if appropriate) or its geometry is set identical to the imaginary volume one, reducing the number of variables to 7 or 8, respectively.

A variation of the Woods-Saxon model that has also been used in this study is the squared WS form, or WS^2. This model is described by the equation below [37]:

$$U(r) = -(V f_V^2(r) + iW f_W^2(r)) \,, \tag{2.50}$$

The double-folding shape

A popular alternative method to obtain OMP parameters is to use double folding potentials. With this method, the potential chosen is obtained using the double integral below:

$$V_{fold}(r) = \int d\vec{r}_1 \int d\vec{r}_2 \rho_1(r_1)\rho_2(r_2)v_{eff}(\vec{s})\,. \tag{2.51}$$

Here, $\rho_1(r_1)$ and $\rho_2(r_2)$ are the nuclear density distributions of the two nuclei. They can be obtained from standard Hartree-Fock calculations [38]. $\vec{s}$ is the nucleon-nucleon (NN) separation distance and is given by $\vec{s} = \vec{R}+\vec{r}_1-\vec{r}_2$, where $\vec{R}$ is the interaction radius. v_{eff} is called the NN interaction potential and can have a number of forms corresponding to the various interaction models that have been tried. Three will be described briefly here. More detailed explanations can be found in Refs. [39] and [40].

The *Jeukenne, Lejeune and Mahaux (JLM)* [41] model is based on an effective interaction which is energy and density dependent. The NN interaction potential has both real and imaginary parts and is written as:

$$v_0(\rho, E) = \frac{V_0(\rho, E) + iW_0(\rho, E)}{\rho}\,. \tag{2.52}$$

The OMP in Eq. 2.51 then becomes:

$$V_{fold}(R) = \int d\vec{r}_1 \int d\vec{r}_2 \rho_1(r_1)\rho_2(r_2)v_0(\rho, E)\delta(\vec{s})\,. \tag{2.53}$$

Two forms of JLM have been used to fit the data in this thesis, distinguished by the

different approximations used for the local density, ρ [40]:

$$\text{JLM1:} \qquad \rho = \sqrt{\rho_1(\vec{r}_1 + \frac{\vec{s}}{2})\rho_2(\vec{r}_2 - \frac{\vec{s}}{2})}\,, \tag{2.54}$$

$$\text{JLM3:} \qquad \rho = \frac{1}{2}(\rho_1(\vec{r}_1 + \frac{\vec{s}}{2}) + \rho_2(\vec{r}_2 - \frac{\vec{s}}{2}))\,. \tag{2.55}$$

It was shown ([41], [42]) that the best results are obtained when the delta function in Eq. 2.53 is approximated by a Gaussian with the shape:

$$g(\vec{s}) = \left(\frac{1}{t\sqrt{\pi}}\right)^3 e^{-\frac{\vec{s}^2}{t^2}}\,, \tag{2.56}$$

where t is a range parameter. The final expression for the JLM DF potential is then:

$$U(r) = N_V V_{fold}(r, t_v) + iN_W W_{fold}(r, t_W)\,. \tag{2.57}$$

N_V and N_W are renormalization coefficients and are usually the only parameters to be varied during the fitting procedure. The range parameters have optimum values at t_V=1.2 fm and t_W=1.75 fm [39], but if necessary, they can be varied as well. Even so, four parameters is still less than the six required by the WS potential.

The *M3Y* model is based on the Paris NN interaction [43]. In this case the effective potential is given by:

$$v_{eff}(r) = V_D(r) + P^{ex}_{1,2} V_{ex}(r)\,, \tag{2.58}$$

where D and ex indicate the direct and knock-on exchange components of the potential. V_D and V_{ex} are averaged over spin-isospin states [39]. Two versions of this model were used in this dissertation, labeled according to the form used for the knock-on exchange component. M3YZR indicates that a zero range potential was used and M3YFR indicates that a finite range potential was used. For the M3Y model, the final OMP was expressed

as:

$$U(r) = (N_V + iN_W)V_{fold}(r)\,. \tag{2.59}$$

2.4 Distorted-Wave Born Approximation

In the previous section, the OMP was introduced in order to characterize the elastic scattering channel of a reaction. The other channels are weaker and in some cases can be described successfully using approximations. Such is often the case for direct nuclear reactions and the *distorted-wave Born approximation (DWBA)*. The DWBA is an approximation applied to the transition amplitude in order to make the corresponding Shrödinger equation solvable. This model relies on the weakness of the direct interaction, treating it as a perturbation.

Therefore, in Eq. 2.30, if one subtracts the elastic contribution, by way of $(\Phi_\beta, U_\beta\Psi_\alpha)$, one obtains the Shrödinger equation describing the perturbation:

$$(E_\beta - T_\beta - U_\beta)\psi_\beta = (\Phi_\beta, [V_\beta - U_\beta]\Psi_\alpha)\,. \tag{2.60}$$

Using Green's function techniques similar to Eq. 2.31-2.34 one arrives at the solution for the wave-function [36]:

$$\psi_\beta \rightarrow -\left(\frac{\mu_\beta}{2\pi\hbar^2}\right)\frac{\exp\left(ik_\beta r_\beta\right)}{r_\beta}\left\langle \chi_\beta^{(-)}\Phi_\beta|V_\beta - U_\beta|\Psi_\alpha^{(+)}\right\rangle\,, \tag{2.61}$$

where χ_β is the solution to Eq. 2.42 but for channel β. It has a plane wave term and a spherical wave term. The (+) and (-) signs indicate outgoing and incoming spherical waves, respectively. At $U_\beta \rightarrow 0$ the wave-function reduces to a plane wave. Therefore, the matrix for the transition $\alpha \rightarrow \beta$ can be written as:

$$T_{\beta\alpha} = \left\langle \exp\left(i\vec{k'}_\alpha \cdot \vec{r_\alpha}\right)|U_\alpha|\chi_\alpha^{(+)}\right\rangle \delta_{\beta\alpha} + \left\langle \chi_\beta^{(-)}\Phi_\beta|V_\beta - U_\beta|\Psi_\alpha^{(+)}\right\rangle\,, \tag{2.62}$$

where the first term represents the elastic scattering and the second term denotes the DWBA amplitude of the nuclear reaction, $T_{\beta\alpha}^{DWBA}$:

$$T_{\beta\alpha}^{DWBA} = \left\langle \chi_{\beta}^{(-)} \Phi_b \Phi_B | V_\beta - U_\beta | \Phi_a \Phi_A \chi_{\alpha}^{(+)} \right\rangle . \tag{2.63}$$

Furthermore, in the DWBA model an assumption is made that the most important contribution to the transition matrix comes from the direct reaction $\alpha \rightarrow \beta$ and the others can be neglected. This approximation is valid for reactions that are peripheral and allows Eq. 2.63 to be rewritten as:

$$T_{\beta\alpha}^{DWBA} = \left\langle \chi_{\beta}^{(-)} I_B^A(\vec{r}) | V_\beta - U_\beta | I_b^a(\vec{r}) \chi_{\alpha}^{(+)} \right\rangle , \tag{2.64}$$

where I_B^A and I_b^a are overlap functions and will be discussed in more detail in the following section.

2.5 Asymptotic Normalization Coefficient

For a direct transfer reaction as shown in Figure 2.2, the information related to the nuclear structure and the relative motion in channels α and β is contained in the transition amplitude, Eq. 2.63, presented in the previous section. Another quantity that is often used to describe direct reactions is the spectroscopic factor, S_{nlj}, which gives a measure of the probability that a many-body system will be found in a specified configuration.

The spectroscopic factor depends on the overlap function and is given by the formula below:

$$S_{nlj} = N \int_0^\infty |I_{bx(nlj)}^a(\vec{r})|^2 \, r^2 dr \, , \tag{2.65}$$

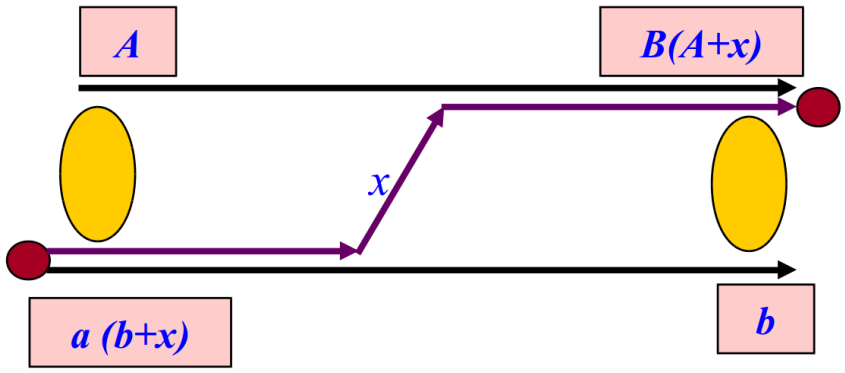

Figure 2.2: Schematic drawing of a transfer reaction, where a is the projectile, A is the target and x is the transferred nucleon.

where N denotes the antisymmetrization factor. In turn, the overlap function is given by:

$$\begin{aligned} I^{a}_{bx(nlj)}(\vec{r}_{bx}) &= \langle \Phi_b(\zeta_b)\Phi_x(\zeta_x)|\Phi_a(\zeta_b,\zeta_x;\vec{r}_{bx})\rangle \\ &= \sum_{l_a m_{l_a} j_a m_{j_a}} \langle J_b M_b j_a m_{j_a}|J_a M_a\rangle \, \langle J_x M_x l_a m_{l_a}|j_a m_{j_a}\rangle \\ &\times i^{l_a} Y_{l_a m_{l_a}}(\hat{r}_{bx}) I^{a}_{bx l_a j_a}(r_{bx}) \,, \end{aligned} \tag{2.66}$$

where $\Phi_{a,x,b}$ are the bound state wave-functions of nuclei a, x and b. The $\zeta_{b,x}$ terms represent the respective internal coordinates. $\vec{r}_{bx}$ is the relative coordinate for the center of mass between b and x, with $\hat{r} = \vec{r}/r$. J and M are the spin and spin projection. j_a and m_{j_a} represent the total angular momentum and its projection for particle x in nucleus a. Similarly, l_a and m_{l_a} represent the orbital angular momentum of the relative motion of b and x and its projection. $\langle j_1 m_1 j_2 m_2|j_3 m_3\rangle$ is a Clebsch-Gordon coefficient. Lastly, $Y_{l_a m_{l_a}}(\hat{r}_{bx})$ is a spherical harmonic function and $I^{a}_{bx l_a j_a}(r_{bx})$ represents the radial overlap. It should be noted that in the summation, l_a and j_a take only the values allowed by parity and angular momentum conservation laws for the virtual process $a \rightarrow b + x$ [44].

The radial overlap function is typically approximated using a model wave function of

the bound state a as:

$$I^a_{bxl_aj_a}(r_{bx}) = S^{1/2}_{bxl_aj_a}\Phi_{n_al_aj_a}(r_{bx})\,, \tag{2.67}$$

where $\Phi_{n_al_aj_a}(r_{bx})$ denotes the bound state wave function describing the relative motion of b and x and $S_{bxl_aj_a}$ is the spectroscopic factor corresponding to the configuration (bx) and its related quantum numbers. The DWBA cross-section can then be expressed in terms of the spectroscopic factors for the initial and final nuclei using the formula:

$$\frac{d\sigma}{d\Omega} = \sum_{j_aj_B} S_{bxl_aj_a}S_{Axl_Bj_B}\sigma^{DWBA}_{l_aj_al_Bj_B}\,. \tag{2.68}$$

This is how the experimental data are typically used to extract the spectroscopic factors which provide important information about the structure of the nuclear states involved. However, it became clear that the actual results may depend strongly on the intrinsic structure $a = b + x$ assumed and the WS parameters used. These parameters cannot be determined unambiguously.

It was then proposed and shown ([44]) that for peripheral reactions, there is another quantity that is more useful to extract. That quantity is the asymptotic normalization coefficient (ANC) that defines the amplitude of the tail of $I^a_{bxl_aj_a}$. This asymptotic behavior is described by:

$$I^a_{bxl_aj_a}(r_{bx}) \xrightarrow{r_{bx}>R_N} C^a_{bxl_aj_a}\frac{W_{-\eta_a,l_a+1/2}(2\kappa_{bx}r_{bx})}{r_{bx}}\,, \tag{2.69}$$

where $C^a_{bxl_aj_a}$ is the ANC; $W_{-\eta_a,l_a+1/2}(2\kappa_{bx}r_{bx})$ denotes the Whittaker function describing the asymptotic behavior of the bound state wave function of two charged particles; $\kappa_{bx} = \sqrt{2\mu_{bx}\epsilon_{bx}}$ is the wave number of the bound state a with ϵ_{bx} being the nucleon separation energy; and $\eta_a = Z_bZ_x\mu_{bx}/\kappa_{bx}$ is the Sommerfeld parameter.

Similarly, the asymptotic behavior of the normalized single-particle bound state wave

function $\Phi_{n_a l_a j_a}$ is given by:

$$\Phi_{n_a l_a j_a}(r_{bx}) \xrightarrow{r_{bx}>R_N} b_{bx l_a j_a} \frac{W_{-\eta_a, l_a+1/2}(2\kappa_{bx} r_{bx})}{r_{bx}} \,. \tag{2.70}$$

Here, $b_{bx l_a j_a}$ is called the single-particle ANC. Plugging Eq. 2.69 and Eq. 2.70 into Eq. 2.67, one obtains the relationship between spectroscopic factor and ANC:

$$S_{bx l_a j_a} = \frac{(C^a_{bx l_a j_a})^2}{(b_{bx l_a j_a})^2} \,. \tag{2.71}$$

Plugging Eq. 2.71 into 2.68, one obtains the cross-section in terms of the ANCs:

$$\frac{d\sigma}{d\Omega} = \sum_{j_a j_B} (C^a_{bx l_a j_a})^2 (C^B_{A x l_B j_B})^2 \frac{\sigma^{DWBA}_{l_a j_a l_B j_B}}{(b_{bx l_a j_a})^2 (b_{A x l_B j_B})^2} \,. \tag{2.72}$$

Unlike the situation for the spectroscopic factors, the ratio between $\sigma^{DWBA}_{l_a j_a l_B j_B}$ and the product of the single-particle ANCs is much less dependent on the geometry of the binding potential due to the fact that the individual dependencies in the two terms largely cancel each other. Therefore, with Eq. 2.72 it is possible to extract the ANC of the exit vertex, $C^B_{A x l_B j_B}$, if the ANC of the entrance vertex, $C^a_{bx l_a j_a}$ is known.

2.6 Astrophysical Reaction Rates

The rate of a nuclear reaction in stellar environments is defined as the number of reactions per second and per unit volume per unit time for the particle pair, $A + x$, involved in the reaction. It can be calculated using the nuclear cross section, σ_v, of the reaction using the formula:

$$R = \frac{n_A n_x}{1 + \delta_{Ax}} \langle \sigma_v v \rangle \,, \tag{2.73}$$

where n_i denotes the number density of particle i and the inclusion of the Kroenecker delta is to account for the case where the particles are identical. Typically, nuclei in stars move

non-relativistically and are nondegenerate and as such, their velocities can be described by a Maxwell-Boltzmann probability distribution [8]:

$$P(v)dv = \left(\frac{\mu}{2\pi k_B T}\right)^{3/2} e^{-\mu v^2/(2k_B T)} 4\pi v^2 dv \,. \tag{2.74}$$

Calculating the average of $\sigma_v v$ over this distribution results in the general form for $\langle \sigma_v v \rangle$:

$$\langle \sigma_v v \rangle = \left(\frac{8}{\pi\mu}\right)^{1/2} \frac{1}{(k_B T)^{3/2}} \int_0^\infty \sigma(E) E e^{\left(-\frac{E}{k_B T}\right)} dE \,, \tag{2.75}$$

where $E = \mu v^2/2$ and k_B is the Boltzmann constant. The standard practice is to use the quantity $N_A \langle \sigma_v v \rangle$ to present reaction rate results. N_A denotes the Avogadro constant and the units for the rate are cm^3 mol^{-1} s^{-1} [45].

Reactions occurring in stars can be categorized in various ways. One method is to split them into reactions involving charged particles (as target, projectile or both) and reactions induced by neutral particles. Given the topic of this dissertation, the following discussion will be focused on the former type, specifically proton capture reactions or (p, γ).

Furthermore, another classification that applies to not just capture reactions but other types of reactions as well (elastic and inelastic scattering, transfer reactions,...) separates reactions into non-resonant (where the cross-section varies smoothly with energy) and resonant (where the cross-section varies strongly around a particular energy value). Most often, the rate of a thermonuclear reaction will contain both of these contributions, therefore they will each be discussed below [8].

2.6.1 Non-resonant reaction

In a non-resonant proton capture reaction, the assumption is that the capture and photon emission occur in one process without an intermediate stage, as shown in Figure 2.3. At low energies, the cross-section is very low due to the Coulomb barrier and as such depends

on the penetrability of the proton through the barrier:

$$\sigma(E) = \frac{1}{E} \exp(-2\pi\eta) S(E)\,, \tag{2.76}$$

where $\exp(-2\pi\eta)$ is called the Gamow factor and $S(E)$ represents the astrophysical S-factor. The nuclear contributions are thus strictly contained in $S(E)$.

Figure 2.4, (top) contains a plot of Eq. 2.76 showing the cross-section dropping sharply with decreasing energy E, for the range below the Coulomb energy E_C. As $\sigma(E)$ drops towards zero, the intersect point between the cross-section curve and the energy axis gives E_L, the lowest energy at which experimental measurements can be made.

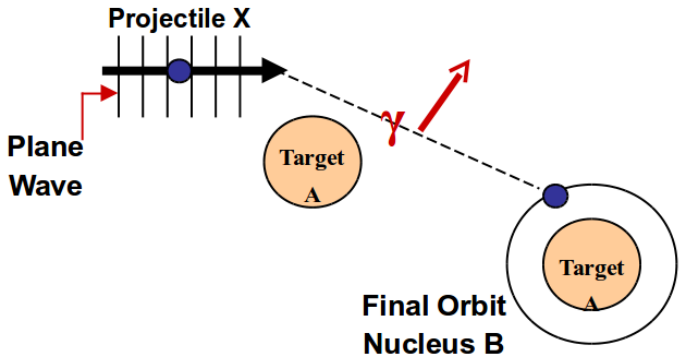

Figure 2.3: Schematic drawing of a direct capture reaction through a non-resonant process. A is the target and x is the captured nucleon.

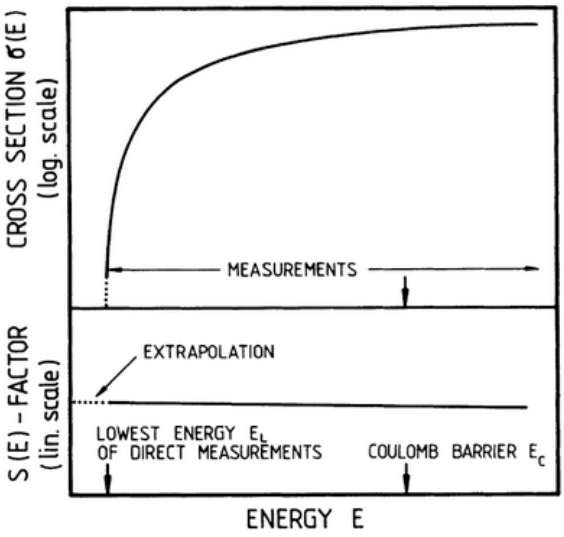

Figure 2.4: (top) Non-resonant capture reaction cross-section, $\sigma(E)$, as a function of the projectile energy. (bottom) Astrophysical S-factor, $S(E)$, as a function of energy. [3]

The bottom plot of Figure 2.4 shows S(E) varying smoothly with the energy and much less than the cross-section [3]. Substituting Eq. 2.76 into Eq. 2.75 leads to an expression for the reaction rate per particle pair in terms of the S-factor:

$$\langle \sigma_v v \rangle = \left(\frac{8}{\pi \mu} \right)^{1/2} \frac{1}{(k_B T)^{3/2}} \int_0^\infty S(E) \exp \left[-\frac{E}{k_B T} - \frac{b}{E^{1/2}} \right] dE \,, \tag{2.77}$$

where b^2 is called the Gamow energy, E_G, and is given by $b = (2\mu)^{1/2} \pi e^2 Z_1 Z_2 / \hbar$. Given that $S(E)$ varies comparatively little with the energy, the exponential term in the integrand is the one that governs the energy dependence of $\sigma_v v$. It is important to note that the Coulomb barrier transmission is reflected in the term $\exp(-b/E^{1/2}) = \exp(-\sqrt{E_G/E})$ which becomes small at low energies, whereas the Maxwell-Boltzmann distribution of the available particles is reflected in the other term $\exp(-E/k_B T)$, which vanishes at high energies.

Their product peaks in the region where both contributions are small and the shape of

it can be approximated by a Gaussian. This energy range is called the Gamow window and the Gaussian peak it contains is called the Gamow peak. This is illustrated in Figure 2.5.

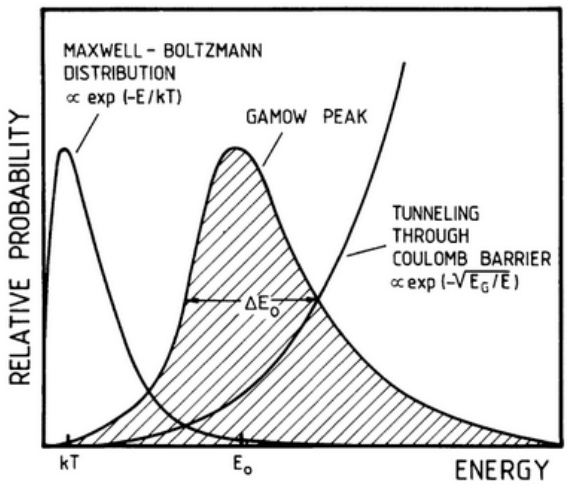

Figure 2.5: Plot showing the two energy-dependent contributions to the non-resonant reaction rate: the Maxwell-Boltzmann distribution and the Coulomb penetrability. Also shown is the Gamow peak resulting from their product. [3]

The position and width of the Gamow peak are given by:

$$E_0 = \frac{bk_BT}{2}^{2/3} = 1.22(Z_1^2 Z_2^2 \mu T_6^2)^{1/3} \text{ keV} \tag{2.78}$$

$$\Delta = \frac{4}{3^{1/2}}(E_0 k_B T)^{1/2} = 0.749(Z_1^2 Z_2^2 \mu T_6^5)^{1/6} \text{ keV} \ . \tag{2.79}$$

Therefore the exponential in the integral from Eq. 2.77 can be replaced by a Gaussian with the shape:

$$\exp\left[-\frac{E}{k_BT} - \frac{b}{E^{1/2}}\right] = I_{\max} \exp\left[-\left(\frac{E-E_0}{\Delta/2}\right)^2\right] , \tag{2.80}$$

where $I_{\text{max}} = \exp(-3E_0/k_BT)$ represents the height of the Gamow peak and is given numerically by the equation:

$$I_{\text{max}} = \exp\left[-42.46\left(\frac{Z_1^2 Z_2^2 \mu}{T_6}\right)^{1/3}\right] . \tag{2.81}$$

From Eq. 2.80 and Eq. 2.81 one can infer that the reaction rate $\langle\sigma_v v\rangle$ depends strongly on the Coulomb barrier. During each of the stellar burning phases described in chapter 1, the nuclei with the smallest barrier are consumed the most rapidly, whereas those with higher Coulomb barriers do not have any significant contribution to the energy production.

If $S(E)$ varies slowly with energy, E, then it can be expanded in a Taylor series around the Gamow peak, E_0 [3]:

$$S_{\text{eff}}(E_0) = S(0)\left[1 + \frac{5}{12\tau} + \frac{\dot{S}(0)}{S(0)}\left(E_0 + \frac{35E_0}{12\tau}\right) + \frac{\ddot{S}(0)}{S(0)}\left(E_0^2 + \frac{89E_0^2}{12\tau}\right) + \dots\right] , \tag{2.82}$$

where τ is a dimensionless parameter that is numerically given by:

$$\tau = 42.46\left(\frac{Z_1^2 Z_2^2 \mu}{T_6}\right)^{1/3} . \tag{2.83}$$

Eq. 2.77 can now be rewritten using Eq. 2.82 as well as Eq. 2.78 and Eq. 2.79 to obtain the reaction rate for a non-resonant process:

$$N_A\langle\sigma_v v\rangle = N_A\left(\frac{2}{\mu}\right)^{1/2}\frac{\Delta}{(k_BT)^{3/2}}S_{\text{eff}}(E_0)\exp\left(-\frac{3E_0}{k_BT}\right) . \tag{2.84}$$

2.6.2 Resonant reaction

A resonant reaction is a two-step process in which the projectile and target first form a compound nucleus in an excited state and then this excited state decays to a lower-

lying state releasing a γ ray. Figure 2.6 shows the schematic of a resonant proton capture reaction. In order for this process to occur the energy, $Q + E_R$, of the entrance channel must be same as E_r, the energy of the excited state in the compound nucleus [3], i.e.:

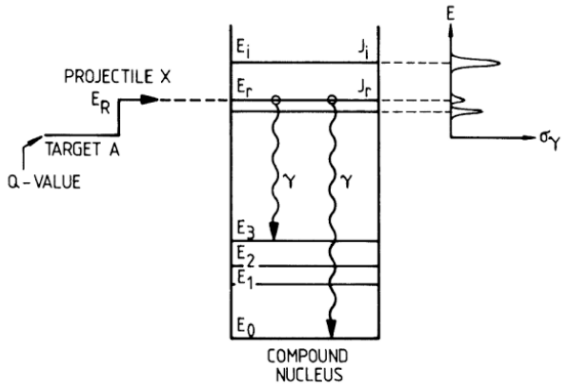

Figure 2.6: Schematic representation of the two-step process involved in a resonant proton capture reaction. [3]

$$E_R = E_r - Q\,. \tag{2.85}$$

This is called a resonant process because the reaction can only occur when Eq. 2.85 is valid. Subsequently, E_R is called the resonance energy. Unlike its non-resonant counterpart, the resonant cross-section is determined mainly from the energy region around the resonant state, provided it is within the Gamow window, and is obtained with the Breit-Wigner equation [6]:

$$\sigma(E) = \frac{\lambda^2}{4\pi}\frac{(2J_r+1)}{(2J_A+1)(2J_x+1)}\frac{\Gamma_x\Gamma_\gamma}{(E-E_R)^2+(\Gamma/2)^2}\,, \tag{2.86}$$

where J_x, J_A and J_r are the angular momenta of the projectile, target and resonant state, respectively. In order for the resonance to be formed parity and angular momentum con-

servation laws must be obeyed, i.e. $\vec{J_r} = \vec{J_A} + \vec{J_x} + \vec{l}$, where $\vec{l}$ is the relative orbital angular momentum of A and x. The last fraction in Eq. 2.86 is called the resonance term and it contains the characteristics of the resonance. The partial widths Γ_x and Γ_γ, respectively, give a measure of the probability that the resonance will be formed and that the channel of interest will be populated in the decay of the resonant state. Γ is the total width of the resonance and is given by the sum of the partial widths of all the open decay channels. And E_R, as mentioned before, denotes the resonance energy.

Substituting Eq. 2.86 at $E = E_R$ into the general form of the stellar reaction rate per particle pair (Eq. 2.75) gives:

$$\langle \sigma_v v \rangle = \left(\frac{2\pi}{\mu k_B T} \right)^{3/2} \hbar^2 (\omega\gamma)_R \exp\left(-\frac{E_R}{(k_B T)} \right) , \tag{2.87}$$

where $(\omega\gamma)_R$ is called the strength of the resonance and is given by:

$$(\omega\gamma)_R = \frac{(2J_r + 1)}{(2J_A + 1)(2J_x + 1)} \frac{\Gamma_x \Gamma_\gamma}{\Gamma} . \tag{2.88}$$

The resonance strength depends significantly on the Coulomb barrier. As a specific example, in the case of a (p, γ) reaction Γ_γ is typically, at most, on the order of a few eV. On the other hand, at resonance energies in the region of the Coulomb barrier, Γ_p can have values on the order of keV. If $\Gamma = \Gamma_p + \Gamma_\gamma$ then under these conditions, $\Gamma \simeq \Gamma_p$ and $\omega\gamma \simeq \omega\Gamma_\gamma$. This indicates that near the Coulomb barrier, the resonance strengths depend only on the γ-widths and are $\lesssim$1 eV.

Conversely, at resonance energies far below the Coulomb barrier, the penetration factor makes the proton width $\Gamma_p \ll \Gamma_\gamma$ and the total width $\Gamma \simeq \Gamma_\gamma$. Therefore, the strength of a very low-energy resonance depends only on the proton width, $\omega\gamma \simeq \omega\Gamma_p$, and this reduced strength makes it very difficult to study these low lying resonances in the laboratory.

2.7 Determining the Rate of the ^{27}Si(p,γ) Reaction

^{27}Si is an unstable nucleus and as such, the (p,γ) reaction cannot be studied directly without access to a facility capable of accelerating unstable beams. Previous studies on estimating this reaction rate indirectly were discussed in the previous chapter. The present work employed similar methods. Specifically, the resonant contribution was estimated empirically and the non-resonant contribution was determined experimentally using the ANC method described above.

In order to determine the resonant contribution, it was necessary to have specific nuclear structure information, i.e. resonance energies, proton partial widths, γ-ray partial widths and spectroscopic factors. Since this information is not available for the nucleus ^{28}P, data from its mirror, ^{28}Al, were used.

For the non-resonant component, the ANC method was used to study the mirror capture reaction, ^{27}Al$(n,\gamma)^{28}$Al, through the peripheral transfer reaction, ^{13}C(^{27}Al,^{28}Al)^{12}C. A ^{13}C target was preferred due to the fact that the virtual neutron capture ^{12}C+$n \rightarrow {}^{13}$C has been studied before and the ANC of ^{13}C is well known. For the first step, experimental data were taken to obtain the differential cross-section distribution of the elastic channel of ^{13}C+^{27}Al. Second, the OMP parameters were extracted from the model fits to the data and were then used to calculate σ^{DWBA} for the transfer reaction. Third, an experimental cross-section angular distribution was obtained for the neutron transfer channel of ^{13}C+^{27}Al. And then fourth, the DWBA calculations were used in Eq. 2.72 together with the experimental data to obtain the ANC of ^{28}Al.

Having this value, the ANC of ^{28}P can be determined from the equality between spectroscopic factors of mirror nuclei. With this ANC, the reaction rate of ^{27}Si(p,γ) can be determined using a radiative capture code called RADCAP.

3. EXPERIMENTAL SETUP AND PROCEDURES

3.1 Experimental Setup

There were 6 experiments conducted specifically for this research project. Four of them had the purpose of studying the reactions below:

1. ^{27}Al(^{13}C, ^{13}C)^{27}Al
2. ^{27}Al(^{13}C, ^{12}C)^{28}Al
3. ^{13}C(^{27}Al, ^{27}Al)^{13}C
4. ^{13}C(^{27}Al, ^{28}Al)^{12}C

The other two were focused on testing the upgrade of the detection setup. For this purpose, additional results were obtained from experiments done with other aims, where the opportunity was provided to take testing data. All of the experiments were done at the Texas A&M University Cyclotron Institute. The beams were obtained from the K150 cyclotron and sent to the MDM beam-line in cave 3 (Figure 3.1).

3.1.1 The MDM Spectrometer

The MDM beam-line consists of a number of magnetic elements - dipoles and quadrupoles - to transport and focus the beam followed by the target chamber, the collimator box, the MDM spectrometer and ends with the Oxford detection system. The target chamber is cylindrical in shape with a target ladder at the center. The standard targets used for this project were ^{197}Au, $\sim$200 μg/cm^2 thick, and ^{13}C, $\sim$100 μg/cm^2 thick, but for the astrophysical study Al targets of various thicknesses were used as well. Also placed in this chamber was the Faraday Cup, which was used to measure the incoming beam charge, for scattering angles larger than 5° (Figure 3.2).

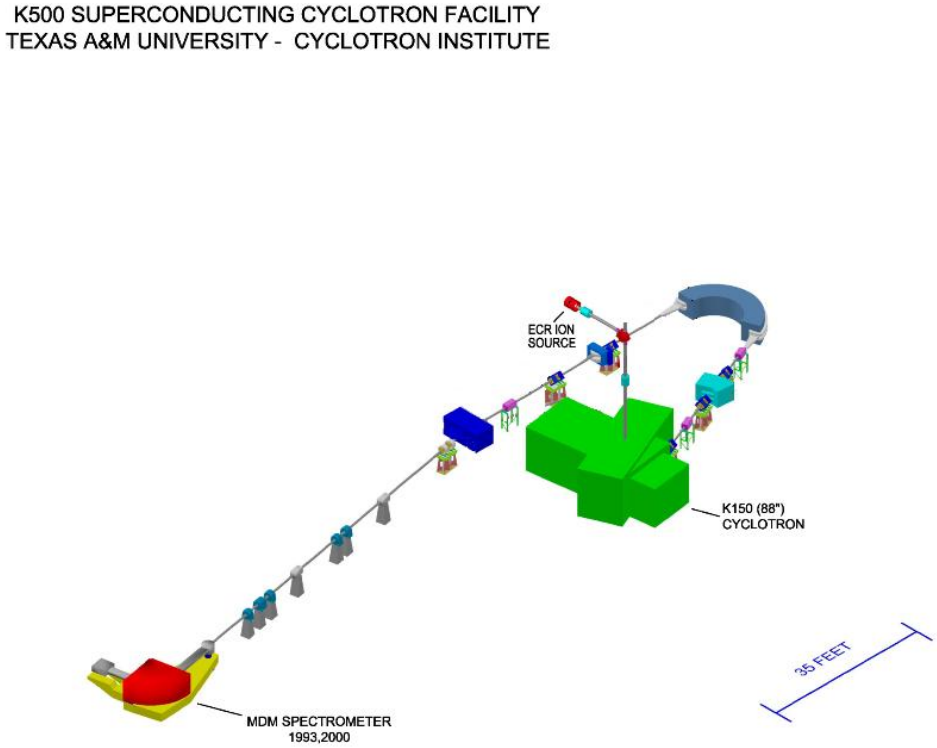

Figure 3.1: Schematic representation of the beam path from the K150 cyclotron to the MDM experimental area.

The collimator box, also called 'slit-box', is placed immediately after the target chamber and contains three collimation masks with each, when chosen, sitting at a distance of 65.25 cm from the target. The 'single slit' mask (Figure 3.3, (a)) has a rectangular opening of 0.1° (11.7 mm high and 1.6 mm wide). The '5-finger' mask (Figure 3.3, (b)) has 5 rectangular openings of identical size to the single slit, placed at 0°, ±0.77° and ±1.53°. The last mask is called the 'wide' or '4-by-1' mask (Figure 3.3, (c)) because its rectangular opening covers 4° by 1° (11.7 mm high and 45.5 mm wide). The masks are made of brass, with a backing of lead to stop the particles that don't go through the openings. They are also used to measure the incoming beam charge at angles smaller than 5°.

The Multipole-Dipole-Multipole (MDM) Spectrometer was originally built for the Na-

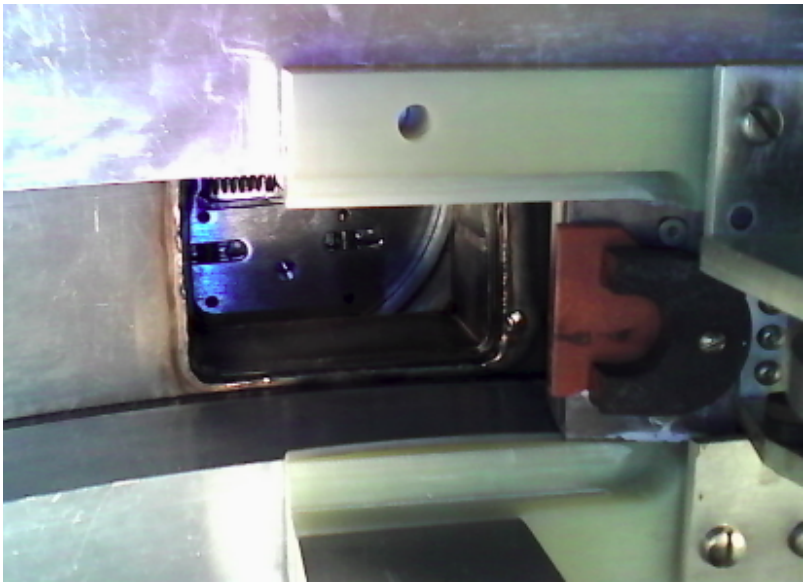

Figure 3.2: Photograph showing the Faraday Cup (on the right) mounted inside the target chamber.

(a) (b) (c)

Figure 3.3: Photographs showing the three collimation masks: (a) the Single Slit mask, (b) the 5-Finger mask and (c) the 4-by-1 mask.

tional Physics Laboratory at the University of Oxford. It became operational in early 1983 and was moved to Texas A&M University in the late 1990s. It has a maximum solid angle of 8 msr and a focal plane that is perpendicular to the detector. The resolving power, E/dE, of the spectrometer was observed to be $\sim$3000 for the center of the focal plane with a deterioration of $\sim$30% at the edges. A schematic representation is shown in Figure 3.4.

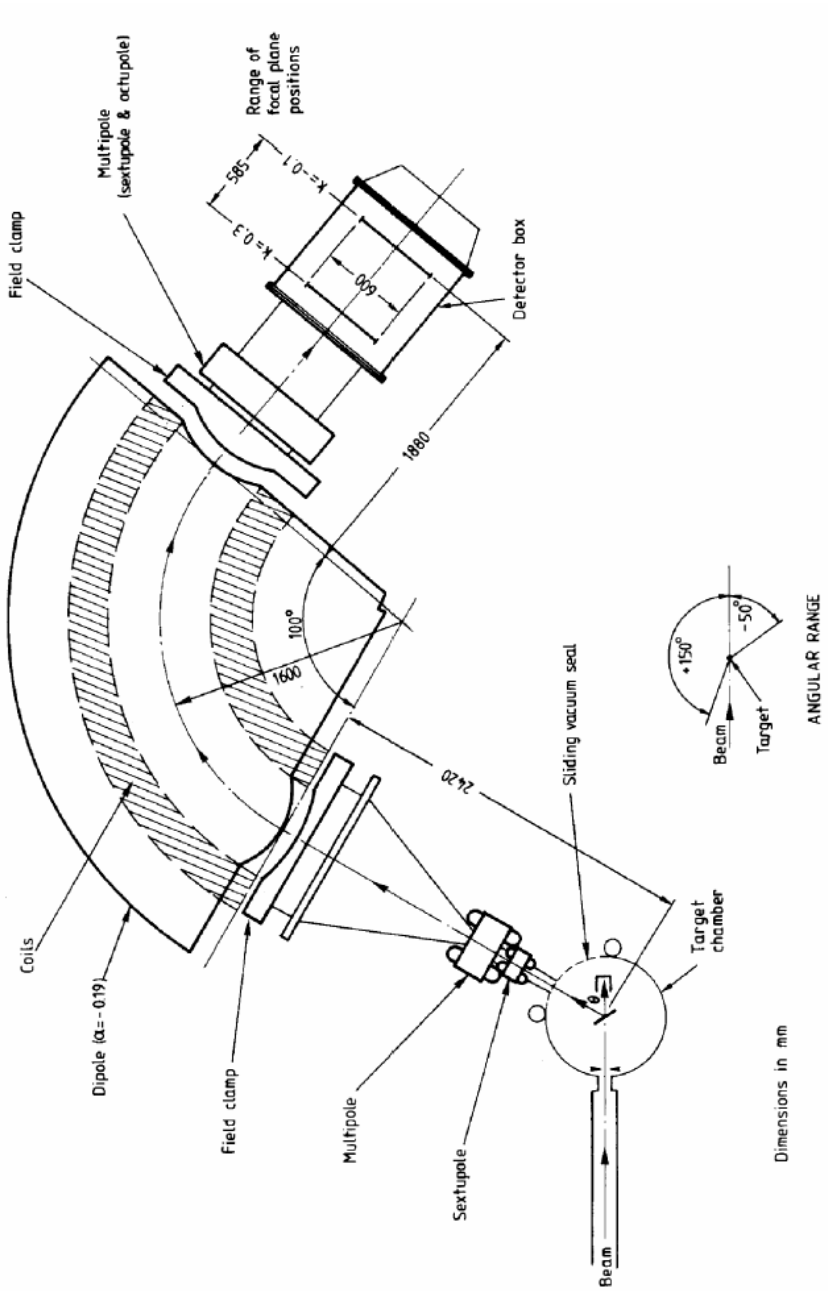

Figure 3.4: Schematic drawing of the MDM spectrometer. [46]

The layout of the spectrometer is as follows: entrance sextupole and multipole, gradient field dipole and exit multipole. The dipole has a central radius of 160 cm, an angle of deflection of 100° and a maximum field strength of 1.5 T. The original tests with a 27 MeV alpha particle beam scattered off a very thin gold foil showed an energy resolution of 9 keV, corresponding to a position resolution of 0.6 mm [46].

The magnetic elements of the spectrometer were used at settings determined by the RAYTRACE computer code [47]. With RAYTRACE it is possible to track the path of a particle from beginning - at the target - to the end - at the focal plane of the spectrometer - taking into account the effects of each element. An example of an input file can be found in Appendix A.

One of the major advantages of the MDM is that the entire spectrometer sits on a mobile platform. This allows it to be rotated around the target chamber in order to measure reactions at different scattering angles, from a minimum of -50° (to the right of the incident beam direction) to a maximum of 150° (to the left) (Figure 3.5).

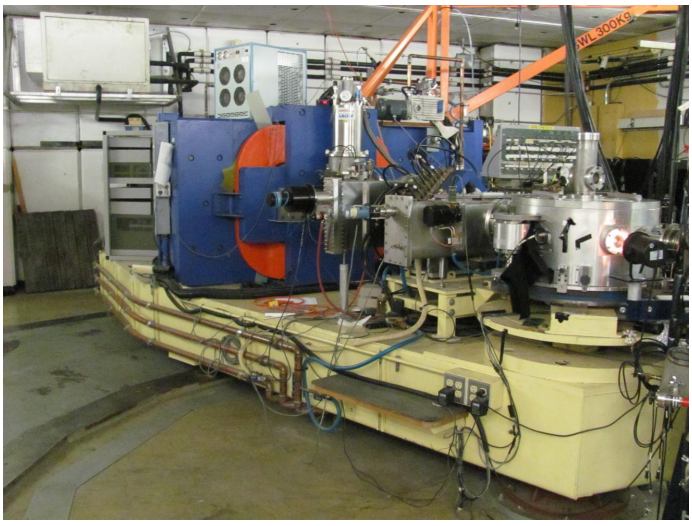

Figure 3.5: Photograph showing the MDM spectrometer and mobile platform (in yellow).

3.1.2 The focal plane detection system

At the back of the MDM spectrometer, we used a detection system, referred to below as the Oxford detector, consisting of a gas section with wires and anode plate readouts and a scintillator whose light output is read out with two phototubes.

'Before' the upgrade

The "Oxford" detector is called such because it arrived with the MDM spectrometer from the University of Oxford. This detector is a gridded ionization chamber with 4 resistive avalanche counters. The chamber is made of stainless steel in a rectangular shape, 77 cm by 60 cm by 31 cm (w x l x h). The walls are 1.27 cm thick attached between 2.54 cm thick frames in a design meant to support the heavy weight. Inside, the detector components and wiring are designed to be supported solely on the front flange (Figure 3.6, (a)). This allows us to easily remove everything simply by unscrewing the flange and sliding it out. A schematic of the longitudinal section is shown in Figure 3.6, (b).

The entrance and exit windows for the gas section are made of Aramica foil with thicknesses of 25 μm and 50 μm, respectively. The height of each window is 6 cm and the width is 30 cm. The geometry of the windows sets an upper limit of $\sim$150 Torr on the gas pressure inside the chamber. Lower mass nuclei, like ^{6}Li or ^{13}C, can and have been studied using pressures as high as 100 Torr ([48–50]). Higher mass nuclei, like ^{22}Ne or ^{26}Mg, require pressures around 20-30 Torr.

The cathode and anode plates are made of aluminum with a gap between them of 12 cm. A grid of wires, called a Frisch Grid (FG), sits at 10.5 cm above the cathode and consists of multiple Be-Cu wires fixed to a frame made of G10 fiber glass. The wires are uniformly spaced, 40 cm in length and 80 μm in diameter, with a pitch of 1.5 mm [1]. In addition, there are fourteen banks of wires going around the detection area that are connected electronically to a voltage divider setup in order to complete the Faraday cage

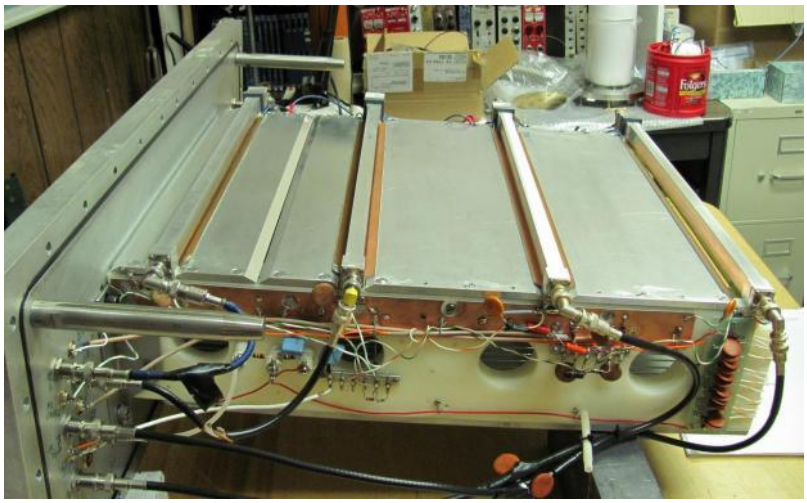

(a)

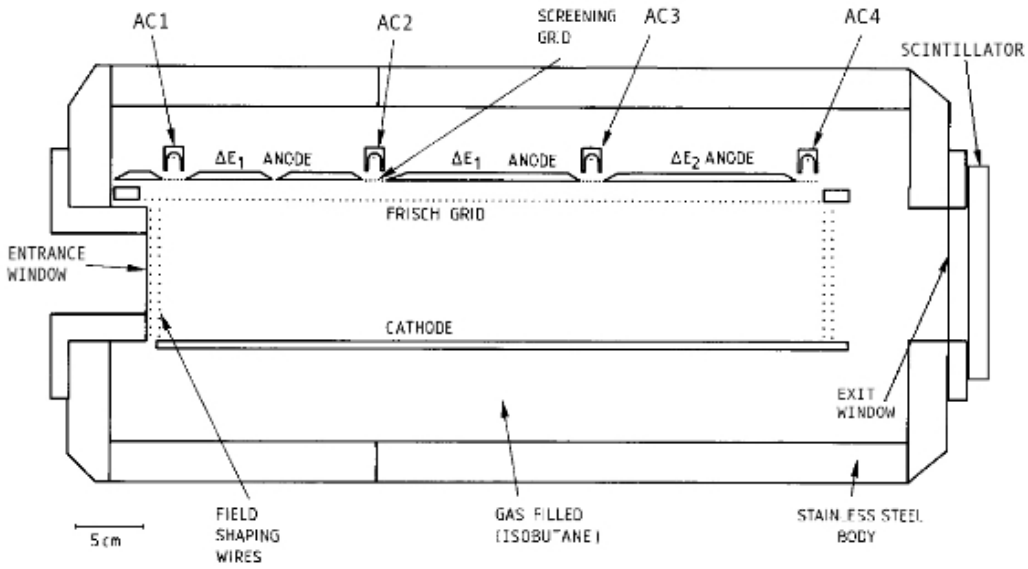

(b)

Figure 3.6: (a) Photograph taken of the inside components of the Oxford detector. (b) Schematic drawing taken from ref [1] and edited to show the current design. In both images, the orientation is the same, with the particles going into the detector from the left.

and ensure field uniformity at the edges.

When a charged particle (usually a heavy ion) travels through the gas, it interacts with the neutral gas molecules creating electron-ion pairs, also called primary pairs. The pos-

itive ions move towards the cathode, while the electrons drift towards the anode where they are eventually collected. The rapid motion of the electrons induces a fast signal. The positive ions, being slower (μ_- $\sim$1000 μ_+), induce a signal on the anode with a longer time. Due to these two contributions, the resulting charge pulse has a nonlinear response to the corresponding energy loss.

The presence of the FG, just below the anode, can reduce and even eliminate the problem. The grid's role is to screen the anode from the effects of the positive ions. The quality of shielding is called 'shielding inefficiency' and is calculated with Bunemann's formula [51] below:

$$\sigma \approx \left(\frac{p}{2\pi A}\right) \log\left(\frac{p}{\pi d}\right) . \tag{3.1}$$

Here, A is the FG to anode distance, d is the wire diameter and p is the pitch. Given the numbers presented above and A=1.5 cm, σ was found to be $\approx$2.8%. Additionally, the same paper by Bunemann provided the transparency condition below:

$$\frac{E_{\text{FG-Anode}}}{E_{\text{Cath-FG}}} \geq \frac{1+\pi d/A}{1-\pi d/A} . \tag{3.2}$$

When this inequality is satisfied all the field lines pass from the active volume of the detector through the FG and reach the anode. The right side was estimated as 1.03. For the entirety of this study, the cathode was set at -800 V. The FG was part of the voltage divider and as such had a voltage of approximately -170 V. With the anode at ground, the resulting field ratio was 1.9 ensuring that the FG was transparent to electrons.

The resistive avalanche counters (called ACs or wires) are used to measure position inside the detector. Each AC has a body (called 'shell') made of aluminum that is 40 cm in length. Inside the shell, a wire made of a Ni-Cr alloy (StablOhm 675 from California Fine Wire company) is soldered under tension to SHV connectors on each end. The voltage ap-

plied to the wires is generally between +800 V and +1500 V. Exceeding the recommended voltage can cause the wires to break. Such a circumstance necessitated the change of the wires before the last of the experiments mentioned at the beginning of this chapter. The 'old' wires had a diameter of 17.7 μm, while the 'new' ones have a diameter of 12.5 μm.

With the shell typically biased at +100 V and a wire voltage of +1000 V, the electric field produced is described by:

$$E = \frac{1000 - 100}{r\ln(7/0.018)} \approx \frac{150}{r}[\frac{V}{m}]\,. \tag{3.3}$$

Therefore, the field starts out small near the shell but gets much stronger towards the wire. Electrons produced in the region below the ACs, drift through the FG and are strongly accelerated by this field. When they are ∼10-20 μm from the wire, the electrons have enough energy that in their collisions with neutral atoms in the gas they create secondary electron-ion pairs, which in turn create more pairs leading to the formation of an avalanche. Individual screening grids under each AC protect the Frisch Grid from the high number of positive ions generated in the avalanche process.

According to Eq. 3.3, the electric field created varies from 15-20 kV/m, near the shell, to 25-30 10^3 kV/m near the wire. Figure 3.7 shows the electric field variation with distance from the anode within the boundaries stated. For pressures of 30-50 Torr and this voltage range, gas multiplication factors are of the order 10^4-10^5 [52].

The production of the output signal is similar to the process previously described for the ionization part of the detector. The signal has two components. One comes from the charge induced by the drift motion of the electrons. The other is due to the charge induced by the motion of the positive ions. The electron component is much smaller and generally considered negligible. The charge induced due to the ions is then divided through the wire resistance and sent towards the two ends of the wire. Since the resistance of the

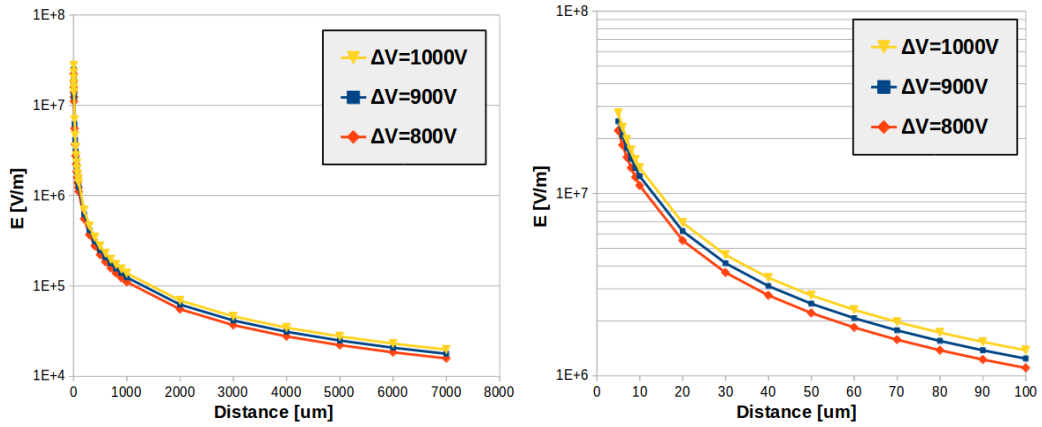

(a) (b)

Figure 3.7: Electric field strength variation with distance from the anode wire, for three values of the voltage difference between the wire and shell. There are two ranges plotted: (a) from 0 to 7 mm, near the AC shell and (b) from 0 to 100 μm, the avalanche region.

wire depends on the length from the interaction to the end of the wire, each charge pulse will be proportional to the resistance it encounters. Knowing that, we can determine the interaction location from the charge, Q_L (left) and Q_R (right), at each end of the wire using the formula

$$x_R = \frac{Q_L}{Q_L + Q_R} D \,, \tag{3.4}$$

where D is the total length of the wire, which is 40 cm as mentioned. The measured positions along the 4 wires can then be used to determine the angle in the detector as long as their placements with respect to each other are known. The first AC is 2 cm behind the entrance window. The other three ACs are placed 15.1 cm, 31.4 cm and 47.7 cm behind the first.

The actual detection region is 30 cm by 51 cm by 10.5 cm (w x l x h). The Oxford detector is generally operated with pure isobutane gas at pressures ranging from 20 Torr to 150 Torr, flowing at a constant rate ($\sim$ 0.2–0.4 l/min) with the help of a MKS250 control unit through a specifically designed system with 6.35 mm diameter copper tubing.

The pressure was monitored with a Barratron gauge. The appropriate gas ports for these were placed in the front flange (Figure 3.10). The MKS flow control unit cannot ensure a constant rate at pressures below 20 Torr which imposes this lower limit on the gas pressures that can be used.

The scintillator (type BC-400) is attached to the frame of the exit window with two wide clamps. An o-ring in the frame provides the seal needed to create a vacuum between the two surfaces. The light produced inside the scintillator is collected with two Hamamatsu photomultiplier tubes (Model Nr. H1949-50) coupled on the sides (see Figure 3.8). There was no optical grease used because the design did not allow us to apply it with complete certainty that there would not be imperfections. In order to minimize light impurities we covered the two couplings and the entire back assembly with black cloth.

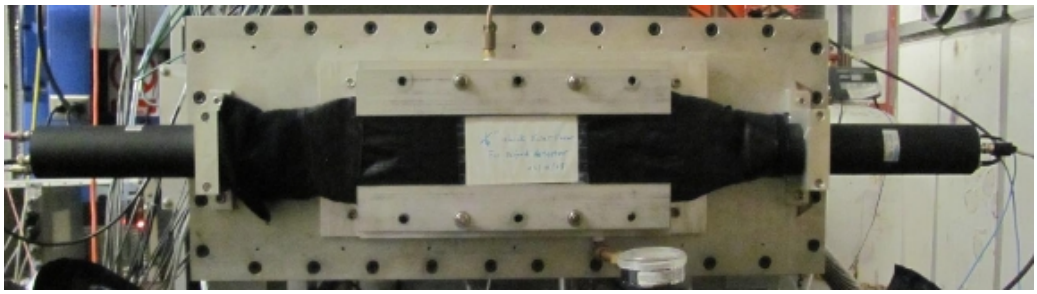

Figure 3.8: Photograph showing the back of the Oxford detector with the scintillator and 2 phototubes.

The specific gas pressure and scintillator thickness are chosen such that the particles of interest pass through the gas and are stopped in the scintillator. For these experiments, we used a 6.35 mm thick scintillator and 4 different pressures - 30, 50, 85 and 100 Torr - of isobutane.

In summary, the Oxford detector supplies us with 11 output signals. The ACs provide us with 8, corresponding to the left and right charges collected from each wire. The plates

between AC_1 and AC_3 give us one signal, called **dE1**, corresponding to the charge signal created from the energy lost in that region of gas. Similarly, the plate between AC_3 and AC_4 gives another energy loss signal called **dE2**. The energy lost by the particles as they stop in the scintillator is detected by the phototubes as 2 separate signals, called **PML** and **PMR**. The geometric average of the two is called $\mathbf{E_{res}}$ or **PM**.

For the internal components, the signals were guided through an electronic scheme using wires, cables, resistors and capacitors as shown in Figure 3.9. To access the signals from outside the chamber, we used two sets of feedthroughs placed on the front flange (Figure 3.10).

'After' the upgrade

Usually, the relative energy resolutions of dE1 and dE2 were between 6% and 17%, such that the lower the pressure, the poorer the resolution. Additionally, dE2 was consistently worse than dE1 because the signal is smaller (shorter path of travel) and the straggling effect from the particle passing through the previous sections becomes more significant. For heavier particles, A > 22, if one wants to reliably measure reactions at higher scattering angles (eg. larger than 10° lab) one would have to use gas pressures $\leq$ 30 Torr. In this case, the dE2 signal tends to blend into the electronic noise and is thus unusable. In cases like this, dE1 also tends to have poor enough resolution that particle identification (PID) is difficult. As explained in chapter 1, the highest mass particle that we tried to detect was ^{27}Mg and Figure 3.11 shows the PID spectrum that we obtained.

The upgrade of the Oxford detector was focused on improving this by improving the energy loss detection. When initial discussions about upgrading the detector started, we had just finished designing and testing a new detection system, called AstroBox. Its purpose was to detect low energy protons emitted during beta-delayed proton decay of nuclei of astrophysical interest [3]. The design relied on using Micromegas, a relatively new de-

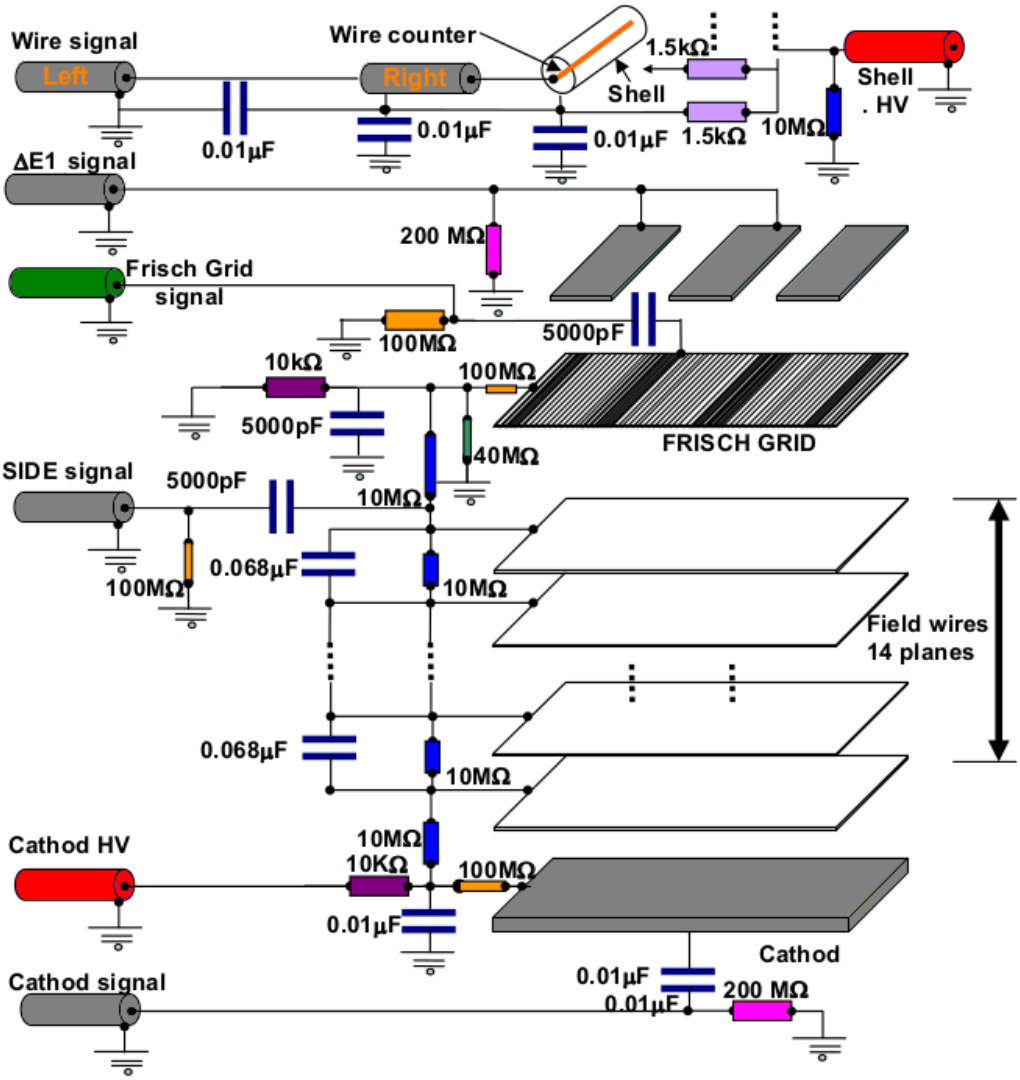

Figure 3.9: Internal electronics scheme for the Oxford detector.

tector technology that operates as a two stage parallel plate avalanche chamber. It consists of a small amplification gap (50-300 µm) and a much larger drift gap (on the order of cm) separated by a thin metallic micromesh. This technology was shown to provide gains of up to 10^5 [4].

With the right gas mix, pressure and field settings, AstroBox was capable of detecting proton energies as low as ∼200 keV without being overwhelmed by the beta background.

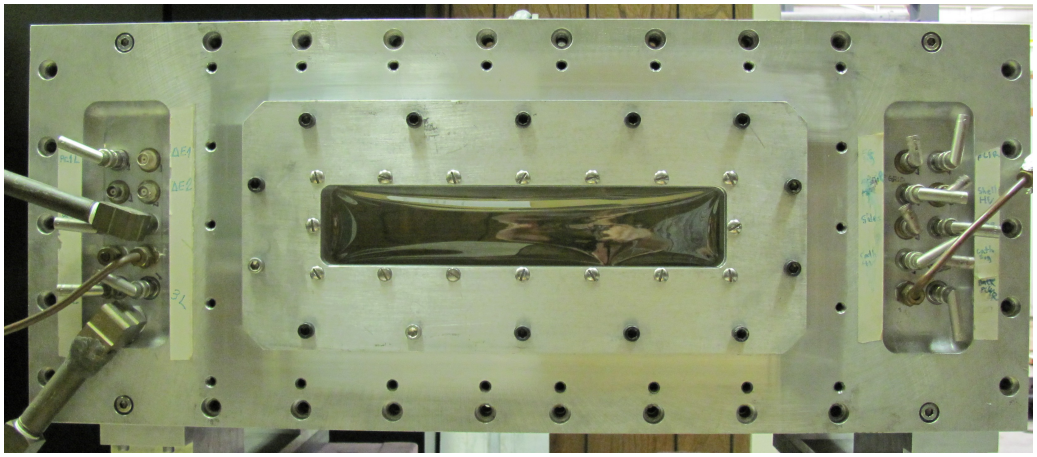

Figure 3.10: Photograph of the front flange of the Oxford detector showing the entrance window and the feedthroughs.

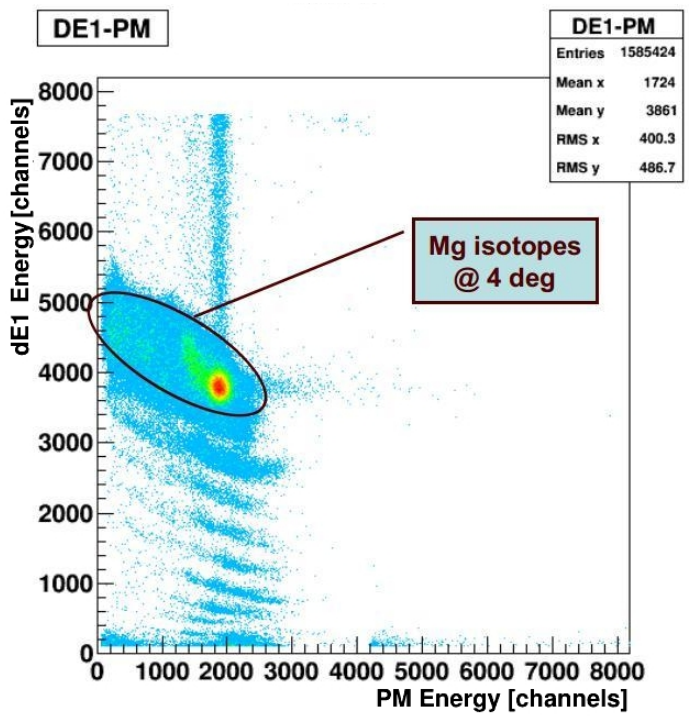

Figure 3.11: Two-dimensional PID plot of dE1 vs PM energy obtained from a beam of ^{26}Mg hitting a ^{13}C target. Reaction products are detected at an angle of 4° in the lab system. The Mg isotopes are indicated in the ellipse.

Moreover, during testing, we found that the Micromegas were also capable of detecting heavier ions with very good separation of various ions, close to the mass region that we use the Oxford detector for. Figure 3.12 shows a PID plot created with AstroBox, i.e. a two-dimensional plot of the energy lost in two consecutive gas sections equipped with Micromegas.

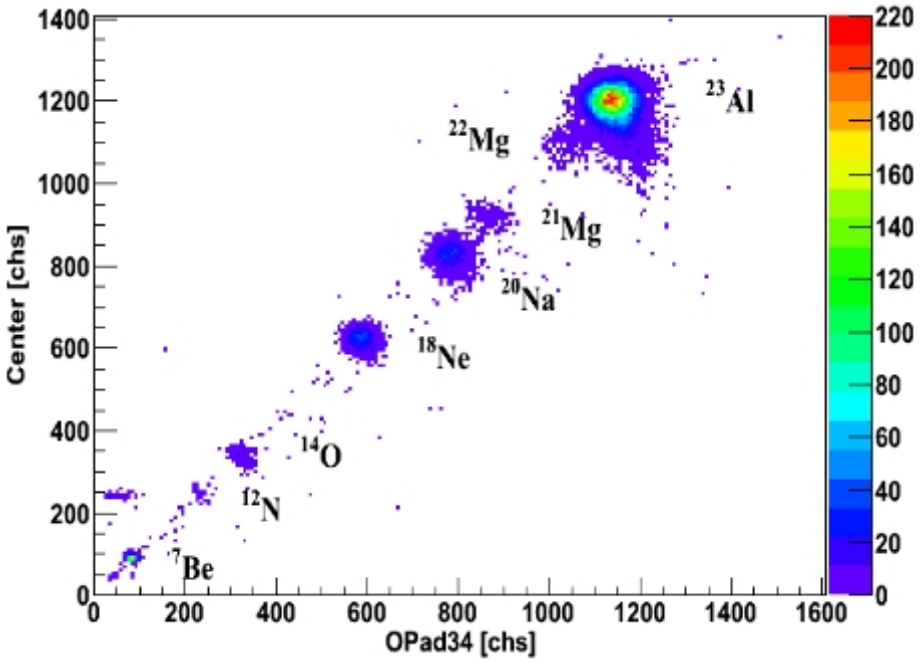

Figure 3.12: Two-dimensional plot of the energies deposited in the center vs exit pads of AstroBox detector. Various species are clearly identified. Gas pressure was kept at p=800 torr.

Given these positive results and the relatively easy operation of the Micromegas, we were leaning towards using this technology to upgrade the Oxford detector. Our first concern about it was that such a detection scheme, combining Micromegas with a gridded ionization chamber, had not been used before so we had no reference points. Our second concern was that at that time there were no published works documenting the operation of Micromegas detectors at the low pressures that we need to use in the Oxford detector.

This was the first attempt to operate a focal plane detector with micro pattern technology as far as we knew.

In light of the initial unknowns, we decided that the upgrade had to be reversible. If the modifications were not successful we could revert to the original design without losing significant time, while we determined what went wrong. The simplest method to achieve this that we found was to replace the dE2 anode with a Micromegas anode of identical size and shape (Figures 3.13 and 3.14).

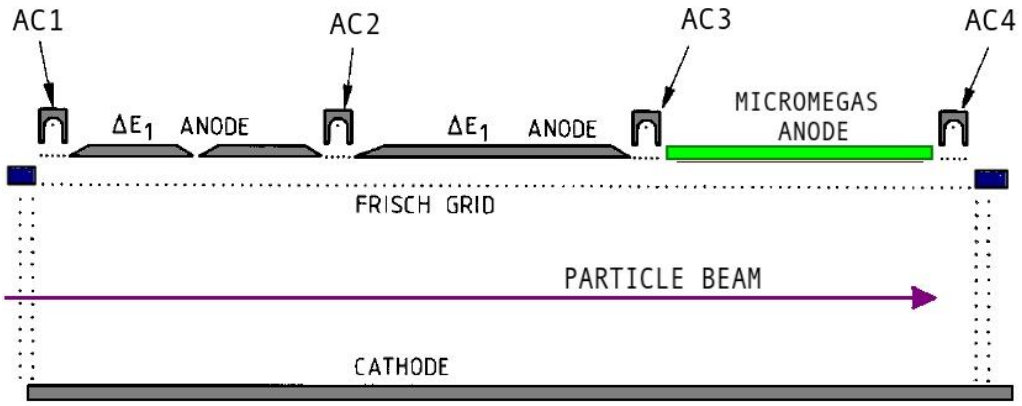

Figure 3.13: Schematic drawing of the inside components of the Oxford detector showing the position of the new Micromegas anode.

The components of the Micromegas plate about to be described are indicated in Figure 3.16 with capital letters. The new anode consists of a circuit board (Figure 3.16, A) printed with gold-plated copper pads (Figure 3.16, B). The PCB has a thickness of 6 mm to allow close to perfect planarity. It is made of multiple layers of circuit board, allowing for the signals between the pads and the connectors to have no capacitive connections to other pad-lines through the use of 6 grounded copper layers. Each pad is 32.5 mm high and 44 mm wide. The space between pads is $\sim$0.2 mm. There are 4 rows and 7 columns, 28 pads

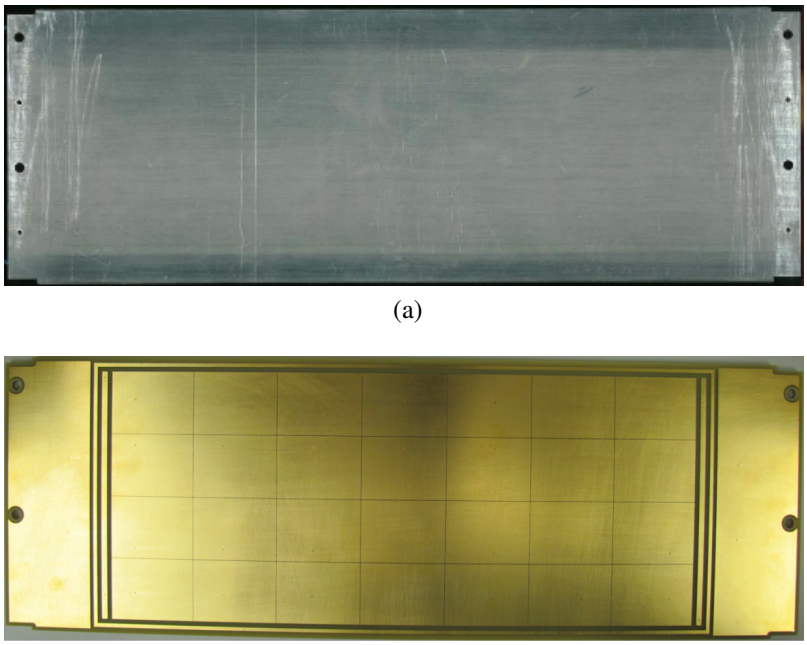

(a)

(b)

Figure 3.14: (a) Original dE1 anode. (b) Photograph of the MicroMegas anode showing the detection pads. The distortion of the shape is an optical effect due to the camera used to take the photograph.

total, forming a detection area of 13.5 cm by 30.9 cm.

In the final version the pads were polished to a mirror finish and Au coated. The inter-pad spaces are filled with resin. Sitting below the pads is a micromesh made of stainless steel inter-woven wires with diameter of 18 μm and a pitch of 63 μm (Figure 3.15, (b)). The thickness of the mesh at the intersection of the wires is 30 μm. The space between the pads and the mesh is called the amplification gap and is 256 μm thick (Figure 3.16, D). The mesh is supported at that distance by numerous insulating resin pillars (Figure 3.16, C), with diameter of 0.4 mm and a pitch of 5 mm (Figure 3.15, (a)). They ensure gap uniformity of the order of 1 to 2 microns. The 256 micron gap allows a relatively high gain at low pressures by giving the electrons a longer path to develop the avalanche.

When it is mounted on the Oxford detector plate, the mesh creates a drift gap with the

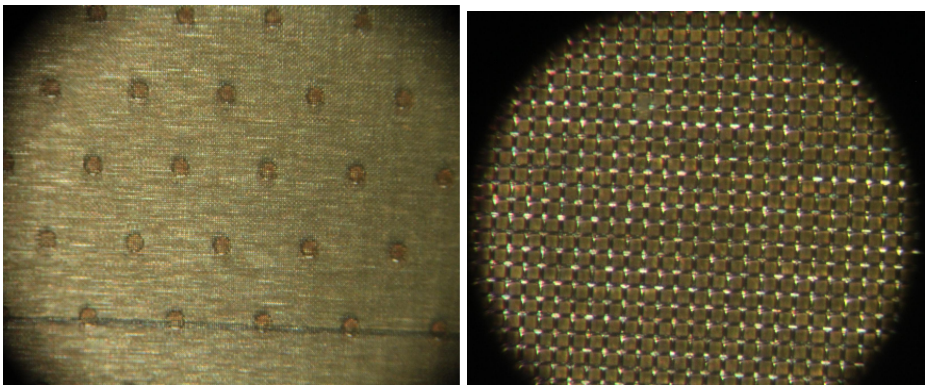

(a) (b)

Figure 3.15: Microscopic photographs taken in the clean room with the lenses focused on (a) the resin pillars and (b) the micromesh.

cathode of 12 cm. Field uniformity in this region is ensured by the Oxford detector Faraday cage. Just before the mesh, the field lines in the drift gap are compressed significantly towards the center of the mesh openings transitioning to the density of field lines expected in the amplification gap. Mesh transparency (opacity) to electrons (ions) depends on the ratio between the amplification field and the drift field. A ratio > 50 ensures better than 95% transparency (opacity) [5].

As explained previously for the ACs, ionization electrons move along the drift field lines toward the mesh and into the amplification gap. There, they are multiplied rapidly and the charge created is collected by the anode pads (Figure 3.16). The positive ions move in the opposite direction and most of them are collected by the mesh. Those that aren't move past the mesh and are collected by the FG. The signal obtained from each pad is the sum of the signal induced by the electrons and the one induced by the ions. The rise time is governed by the velocity of the ions in the gap, which in this case was $\sim$1 μs.

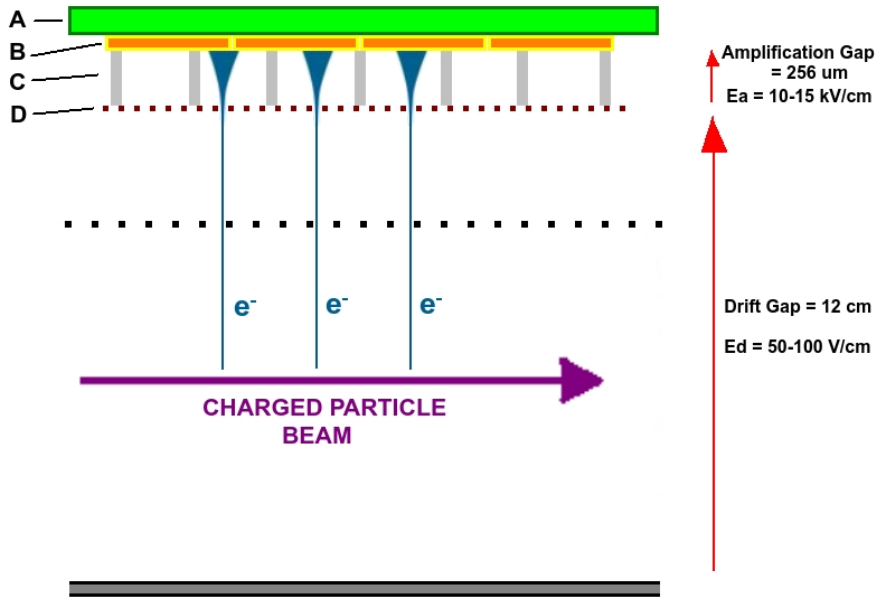

Figure 3.16: Schematic of the Micromegas detector. Sizes are not to scale. The main components of the Micromegas anode are indicated in capital letters: A - the PCB board, B - the gold-plated copper pads, C - the resin support pillars and D - the micromesh.

Initially, we wanted a single large area of detection, like the previous anode. However, in that case the capacitance would have been $\sim$2 nF, which would have given significant noise problems. The current pad dimension is the largest that could be used while keeping a reasonable signal to noise ratio ($\sim$300:1). Another worry was that the charge created by particles with high Z over the entire surface would be large enough, even at low voltages, to trigger significant sparking and detector breakdown.

In line with the low-modification aim of this upgrade, the mounting of the Micromegas anode involved minimal changes to the Oxford detector. The old anode and related grounding cables were removed and the new anode was screwed in place. The sides signal which can be seen in the schematics from Figure 3.9 was previously unused and thus could be disconnected from the front flange. The corresponding feedthrough was then connected to the mesh output on the Micromegas anode using a low-capacity coaxial cable. To create

the necessary electric fields, the mesh was grounded using a 50 Ω BNC terminator.

Additionally, in order to control the strength of the drift field just below the mesh, the 40 MΩ resistor pair between the FG and ground was replaced with a 'variable' resistor. This was done by connecting the FG to the feedthrough that was allocated as 'FG signal' (also previously unused) and using a resistor box outside the detector chamber. This allowed easy access to the voltage divider without repeatedly opening the detector chamber. Figure 3.17 shows the section of the electronics scheme from Figure 3.9 that was changed and the modifications. The 28 individual signals are routed through the internal circuit of

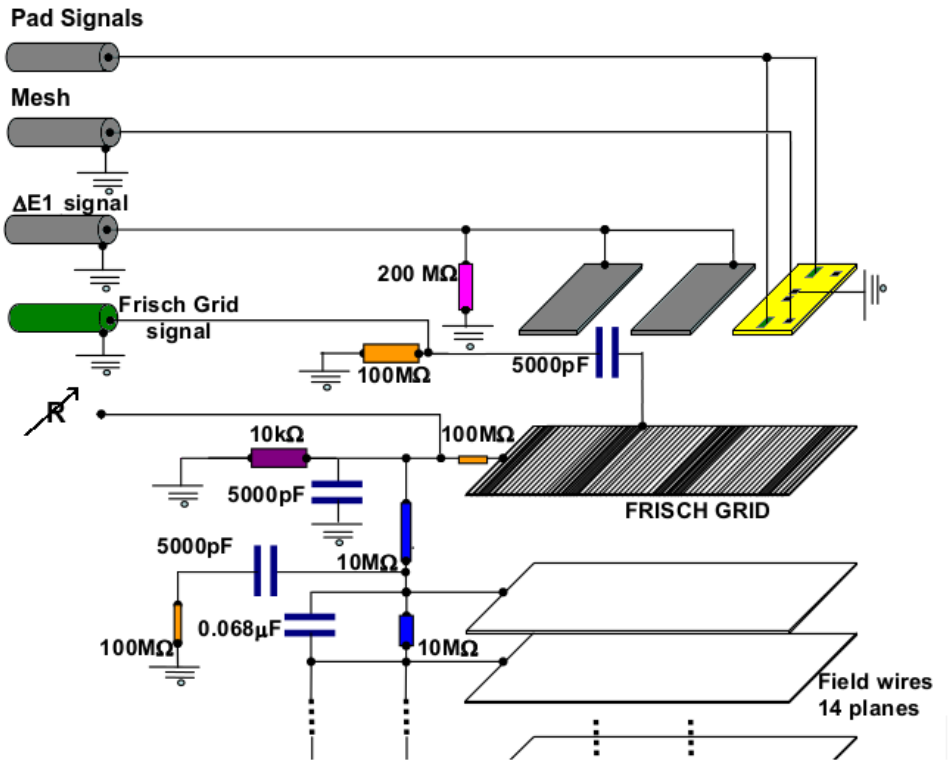

Figure 3.17: Section of the internal electronics scheme of the Oxford detector showing the modifications needed to have the Micromegas anode set up correctly.

the PCB to two DSub-25 connectors (Figure 3.18,(a)), the top 2 rows going to one connec-

tor and the bottom 2 going to the other (Figure 3.18,(b)). The printed circuit was designed to minimize noise and cross-talk between pads. From the DSub-25 connectors, the sig-

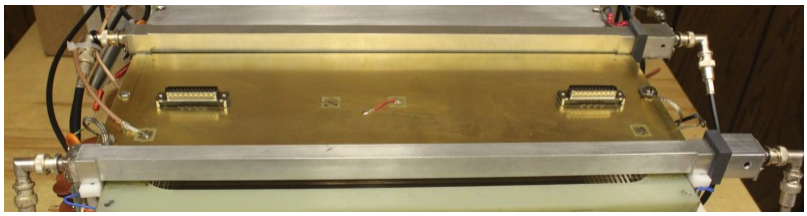

(a)

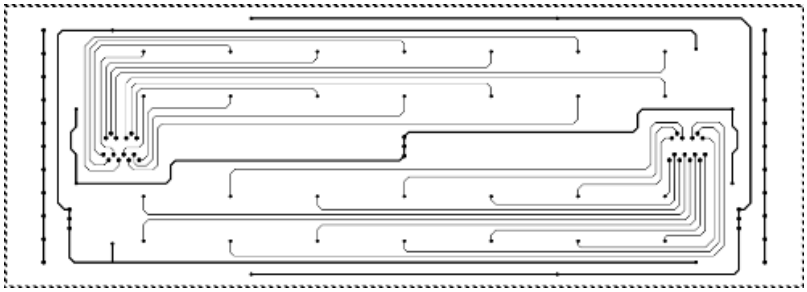

(b)

Figure 3.18: (a) Photograph taken of the Micromegas anode after it was mounted on the Oxford detector. (b) The printed circuit lines showing the mapping between pads and the connector pins for the Micromegas.

nals are sent outside the Oxford chamber using two flat cables. In order to reduce the noise from the cable length, we had to design and build a new mid-section for the detector chamber, one that would have two flanges with DSub-25 feedthroughs right above the two DSub-25 connectors. In this manner, the flat cables ended up being the shortest possible, $\sim$ 7 cm. Additionally, we did not want to have contamination from out-gassing of the new materials, so the cable connectors were made of PEEK (polyetheretherketone) and the wires were made of silver-plated copper with kapton insulation. Figure 3.19 shows the technical design for the new section of the chamber in (a) and a photograph of the complete chamber after mounting the Micromegas anode and before connecting the flat

cables, in (b).

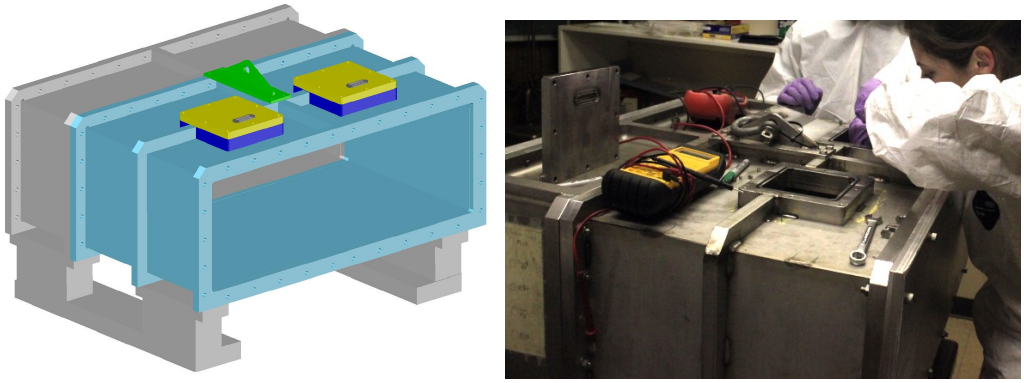

(a) (b)

Figure 3.19: (a) 3-D AutoCAD design of the Oxford chamber showing the new elements in color, while the old components are in gray. (b) Photograph taken of the complete chamber after mounting the Micromegas anode and before connecting the flat cables.

The electronic modules that were used and the manner in which they were connected in order to guide the signals from the detector chamber to the acquisition computer will be described in the next subsection. Throughout the rest of this chapter and the next, the Micromegas energy will sometimes be referred to as 'MuO Energy' or E_{MuO} in both the text and related figures.

3.1.3 The DAQ system

The data acquisition system was set to monitor and record 39 signals from the Oxford detector using preamplifiers, amplifiers, ADC modules and one VME electronics crate. For the 8 signals from the ACs we used 8 Canberra 2004 preamplifiers and one CAEN N568B 16-ch spectroscopy amplifier. In order to minimize noise, short SHV-SHV cables ($\sim$0.5 ns) were used from the feedthroughs to the preamplifier inputs and 8 ns BNC-BNC cables from there to the amplifier. The position along each wire was calculated in the DAQ

software with the formula:

$$POS = A\frac{L}{L+R}\,. \tag{3.5}$$

Here, A is the number of channels in the POS histogram (specifically, 1024), while L and R represent the charges induced at each end of a wire after ADC conversion. The angle of the path inside the detector was also calculated by the software from the positions along the first and last AC, using the formula:

$$ANG = POS_1 - POS_4\,. \tag{3.6}$$

Each AC wire was biased through the corresponding right preamplifier. The typical operation voltages were: +100 V for the shells and +800-1000 V on the wires themselves. Exact voltage settings were decided during each experiment in order to obtain the best possible position and angle resolution.

The cathode was biased to $\sim$ -800 V. The dE1 signal was first processed with a Canberra 2004 preamplifier and then shaped with a second N568B module. Two other input channels of this same module had the amplified (with a fast-timing amplifier) PM signals. The phototubes were typically operated at voltages between -1600 V and -1800 V. The resolution of dE1 depended on gas pressure, the energy and type of particle detected and the electronic settings used.

For the Micromegas pad signals, each set of 14 was shaped and amplified first with a Mesytec MPR16 preamplifier and then a Mesytec MSCF-16 amplifier. The Miromegas anode was operated in the region 250-400 V. A scan of the bias was necessary at the beginning of each experiment in order to determine the optimum voltage to use. More details on this will be provided in Chapter 4, Section 1.

All the processed signals were digitized using two VME-ADC 32-channels modules.

Figure 3.20 shows the schematic described above.

As the trigger for the acquisition, we decided to use the coincidence between the two phototube signals because the scintillator response is faster than both the ACs and the Micromegas .

Two anode outputs from the phototubes were filtered with a constant fraction discriminator (CFD) and used as inputs for a LeCroy 622 coincidence module. Two outputs from it were used for real time monitoring and counting purposes. A third output went into a Philips coincidence module, along with the DAQ veto (dead-time) signal. One logic output of this module was then used as the trigger for the acquisition. A second output was used in an Ortec 8010 Gate and Delay Generator module to create the logic gates for the ADC modules. This triggering scheme is also shown in Figure 3.20.

The FC placed inside the target chamber gave a signal that was measured with a TAMVEC Current Integrator (Model Nr. 1000c). The total beam charge was counted with an ORTEC 995 Counter using the formula

$$Q[nC] = I_{\text{beam}}[nA] \cdot \frac{FC_{\text{Counts}}}{1000}\,, \tag{3.7}$$

where, I_{beam} denotes the beam intensity expressed in nA units, FC_{Counts} represents the number shown by the digital display of the counter module and the number '1000' in the denominator represents the conversion factor of the integrator, in this case 1000 pulses/-counts per second.

Data events were observed, recorded and analyzed with a software created in Linux, using the C++ based ROOT framework [6].

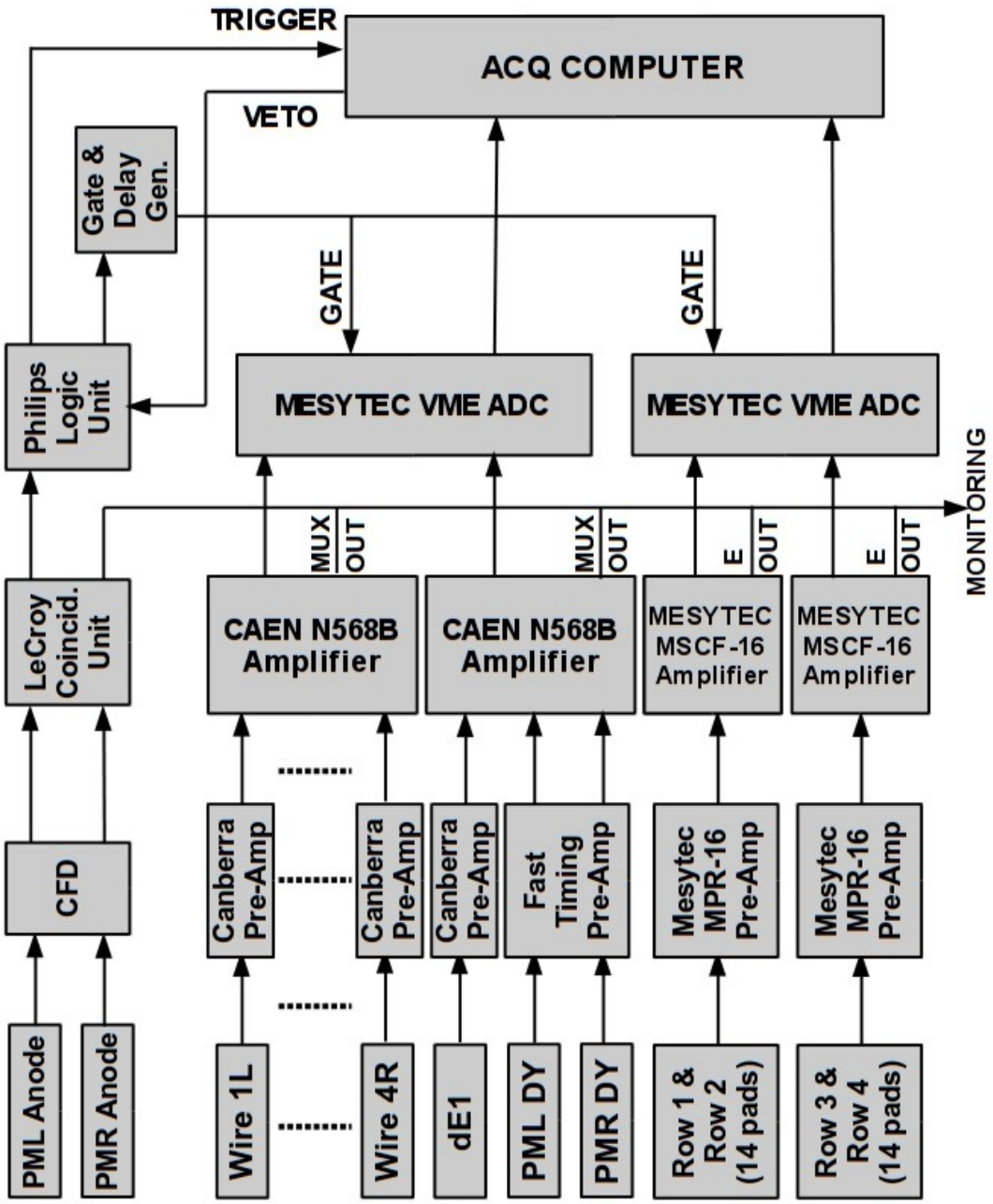

Figure 3.20: Schematic drawing of the electronic modules processing the signals from detector to acquisition computer.

3.2 Experimental Procedures

3.2.1 Gain-matching the wires (ACs)

Before each experiment the ACs have to be gain-matched. This procedure involves sending a charge pulse (from a pulser) through a 25 pF charge converter and then into the detector input of each amplifier. For each AC we changed the gains in the CAEN shaper to match the left and right pulses.

3.2.2 Beam energy determination

The energy of the primary beam is determined using the Single Slit mask and a ^{197}Au target of known thickness. The heavy target provides us with a secondary beam of mostly elastically scattered particles. The collimated beam is then sent through the MDM spectrometer and into the detector. Changing the dipole field allows us to sweep the beam across the detector. In this way, we can find the edges of the detector (specifically the B field values) and thus the center. Knowing the rigidity, we can calculate the energy of the central ray, which is also the energy of the secondary particles after the reaction on the gold target.

Before the upgrade, we did this by looking at the signals of the phototubes. Every time we reached an edge, the corresponding PM signal rate would decrease. After the upgrade, we used the Micromegas anode. But instead of finding the edges of the detector, we looked for the edges of the central column.

The accuracy of this estimation depends on a number of factors. One of them is the primary beam alignment. Before an experiment starts, the beam obtained from the cyclotron has to be focused and centered on “target" using a viewer with markings. If the beam is off-center or coming at an angle then the assumptions made about the kinematics of the reaction taking place are incorrect.

Another factor is the beam dispersion at the scintillator. It is difficult to determine

exactly when an edge is reached. However the biggest uncertainty comes from the target thickness. In general, we assume that beam misalignment is nonexistent and that the errors in estimating the edges of the scintillator are negligible. For the experiments done in this study, the target used to estimate the beam energy was ^{197}Au and its thickness was determined as described in subsection 3.2.6.

Therefore, the adopted uncertainty for the beam energy was 3.6%. This value was used in all the other error determinations were beam energy was a factor.

3.2.3 Position Calibration

As mentioned before, each AC provides two signals, left and right, which are used to determine the position of the particle along the x axis at that particular depth in the detector. These 4 positions can then be used to determine the angle of the path and to reconstruct the focal plane. However, in order to do that correctly each AC must be calibrated such that the raw measurements are converted to metric units. Specifically, for each AC, we need to obtain a set of parameters p_{ij}, where i is the AC number, j=0,1,2 and:

$$PSC_i[cm] = p_{i0} + p_{i1} \cdot POS_i[ch] + p_{i2} \cdot POS_i^2[ch]\,, \tag{3.8}$$

where POS_i is the raw position at each AC, as calculated with Eq. 3.7 and PSC_i is the calibrated position.

The procedure to determine these parameters involves scattering on a gold target at a low angle where the cross-section is large enough for the calibration to be done quickly. The secondary (scattered) beam is collimated using the 5-finger mask and the tracks of the particles are observed for 4 or 5 different B field values. Figure 3.21 shows the typical spectra obtained with AC_1 for a ^{27}Al beam and MDM angle of 4°. The small background of events sitting to the left of the peaks in Figure 3.21, (c) denotes inelastic scattering off the ^{197}Au target (lower energy results in less rigidity and particles that aren't bent as far

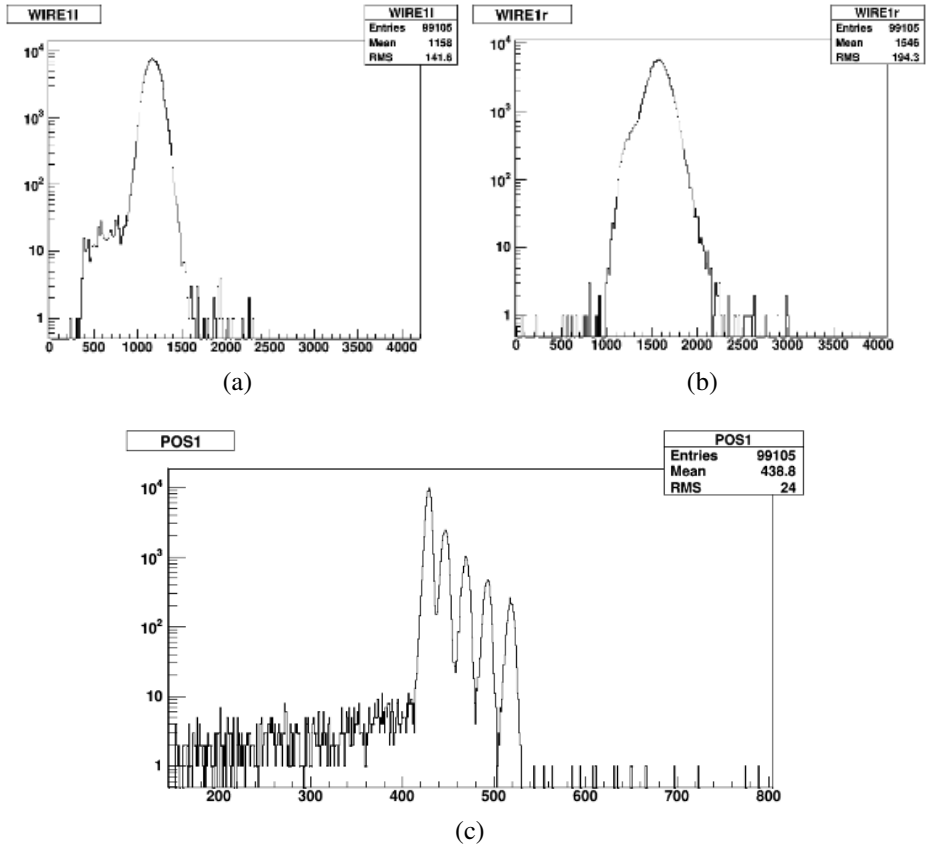

Figure 3.21: Typical spectra obtained with the first avalanche counter for calibration purposes. (a) Spectrum for the left signal. (b) Spectrum for the right signal. (c) Spectrum for the reconstructed raw position.

away from the left end of the wire as the elastic events).

Figure 3.22 shows an example of calibration fits for the 4 wires.

The X-axis error bars represent statistical errors. For the Y-axis, the RAYTRACE code does not give errors for the results it calculates. Instead, the uncertainties were determined by considering the experimental variables that go into the input file: beam energy and MDM magnetic field. The beam energy is used to determine the particle velocity at the beginning of its path. Therefore, the associated uncertainty was found as $\Delta v/v = (1/2)\Delta E/E$ =1.8%. The MDM magnetic field has an error of 0.5 G that comes

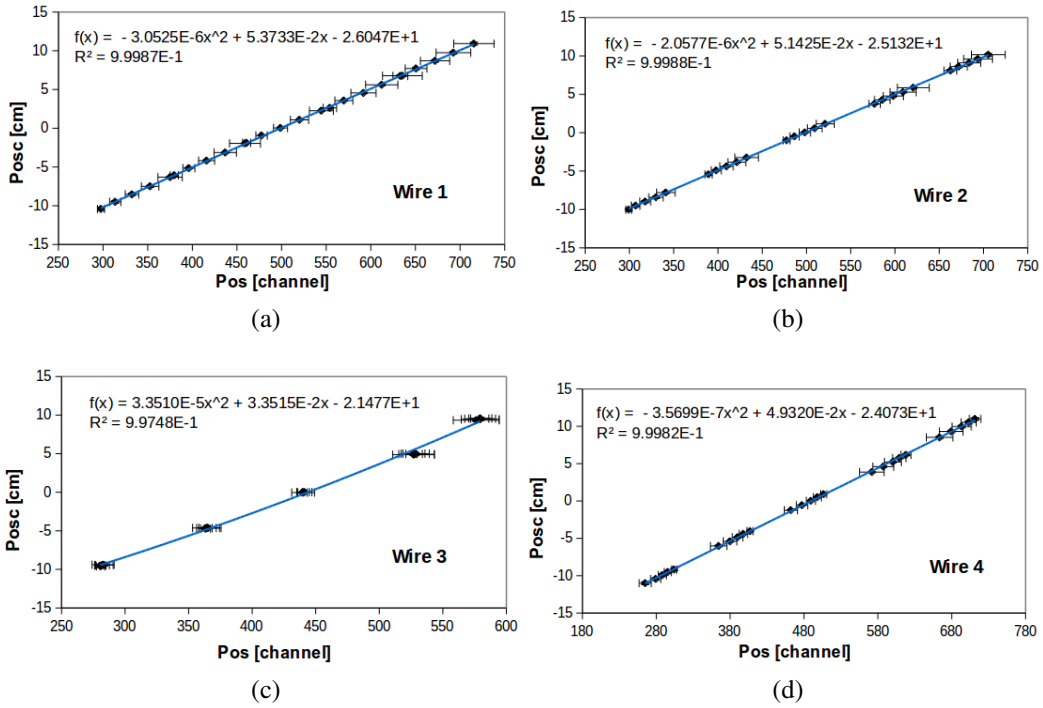

Figure 3.22: (a-d) Example of quadratic calibration fits for the avalanche counters. The error bars are explained in the text.

from the precision of the electronic equipment used to set the field. But such a variation did not produce a change in the RAYTRACE calculations and as such, this possible contribution to the total uncertainty was neglected. The Y-axis error bars that appear in Figure 3.22 reflect only the 1.8% from the beam energy.

As can be seen, having data from a higher number of field values allows for a better fit estimation, particularly when the focal plane is near one of the ACs (AC_3 in the figure).

3.2.4 Angular Calibration

The purpose of the procedure of angular calibration is to find the target angle as a function of the detector angle and is done solely using RAYTRACE simulations. The angle of a particle track in the detector, θ_d, is determined from the positions along any two wires. In order to determine the corresponding angle at the target, θ_t, we use RAYTRACE

to simulate the tracks of particles with several different energies, at the same B field. For each of these energies, we obtain a quadratic function relating θ_t to θ_d:

$$\theta_t = A + B\theta_d + C\theta_d^2 \,. \tag{3.9}$$

An example of this type of fit is shown in Figure 3.23, (a). Since these data points were solely generated with RAYTRACE the errors were the same, at 1.8%, for θ_t and θ_d.

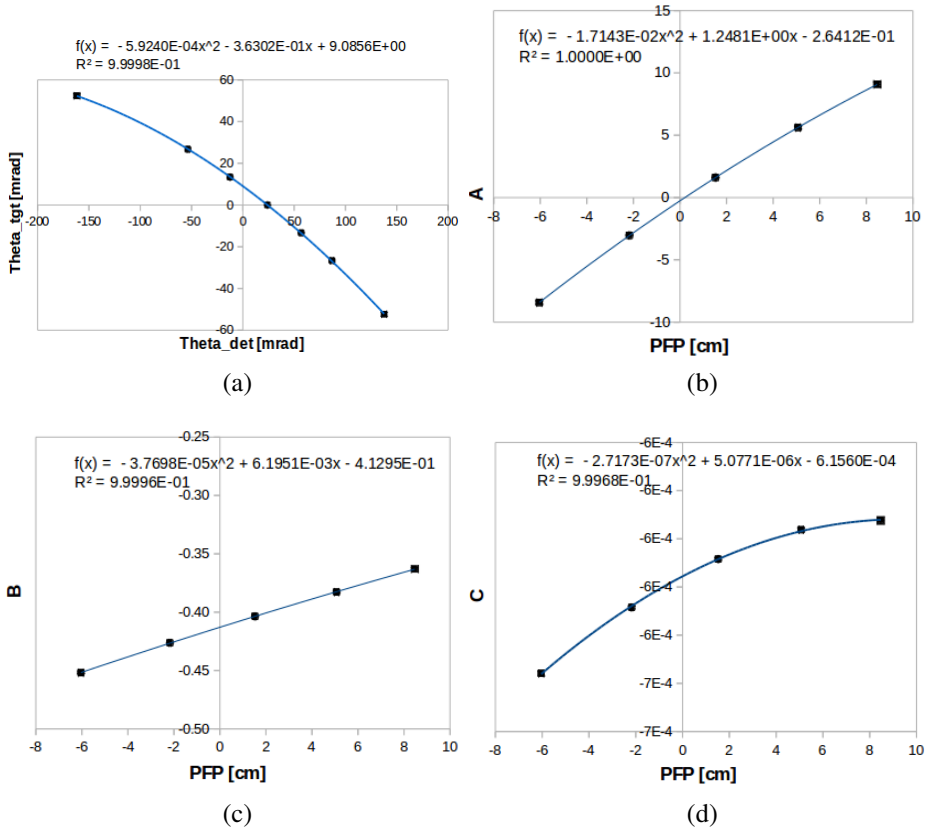

Figure 3.23: (a) Example of a quadratic fit of the θ_t versus θ_d calculations for angular calibration. (b-d) Quadratic fits of the calibration coefficients, A,B and C, as function of the position in the focal plane. In all four plots error bars are included but too small to see.

The coefficients A, B and C depend on the particle energy, which we don't know. However, particles with different energies have different positions in the focal plane, PFP. The relationship between the A, B and C coefficients and PFP was found to be described by the formulas below:

$$\begin{aligned} A &= A_1 + A_2 * PFP + A_3 * PFP^2 \\ B &= B_1 + B_2 * PFP + B_3 * PFP^2 \\ C &= C_1 + C_2 * PFP + C_3 * PFP^2 \,. \end{aligned} \tag{3.10}$$

The coefficients A_1, A_2,...C_3 are the final parameters required in the analysis. Figure 3.23, (b-d) shows the type of plots used in the calibration. The uncertainty of PFP was 1.8% while the errors of the A_1,...C_3 coefficients were determined using regression analysis. Using these quantities, the uncertainties for A, B and C were calculated with the formula:

$$\Delta y = \sqrt{\left(\frac{\delta y}{\delta x_1}\right)^2 (\Delta x_1)^2 + \left(\frac{\delta y}{\delta x_2}\right)^2 (\Delta x_2)^2 + \cdots}, \tag{3.11}$$

where, $y = f(x_1, x_2, \cdots)$, and found to be on average 2%, 0.2% and 0.2%, respectively. These values were used to plot the Y-axis error bars in Figure 3.23, (b-d). For the angular information in the experimental data, these uncertainties were calculated similarly, with the exception that ΔPFP was given by the position resolution in the focal plane.

ΔA, ΔB and ΔC were then used with Eq. 3.11 and Eq. 3.9 to determine the uncertainty in the target angle, $\Delta\theta_t$. It should be noted that in this case the detector angle uncertainty that was used, $\Delta\theta_d$, was found from the behavior of the detector at the time of the experiment.

The angular calibration procedure was done for every MDM angle where data were taken.

3.2.5 Faraday Cup normalization

The last of the calibrations needed to be done at the beginning of an experiment is for the Faraday Cup. In order to accurately count the number of particles in the beam it is necessary to make sure that the FC works properly and if necessary determine a correction factor. This check is done at small angles ($\leq 6°$) with a heavy target like gold where the expectation is that the elastic scattering is of the Rutherford type.

In that situation, data are taken for a set number of counts on the beam current integrator (typically 200,000) with the 5-finger or 4-by-1 mask in order to obtain a set of determinations that can be statistically averaged into a final result. The experimental cross-section is then calculated with Eq. 5.4 using the set number and compared to the theoretical Rutherford cross-section:

$$\sigma_{Ruth} = \left(\frac{Z_{\text{beam}} Z_{\text{target}}\, e^2}{4E} \right)^2 \sin(\theta/2)^{-4}\,. \tag{3.12}$$

An example is shown in Figure 3.24 for a beam of ^{13}C scattered on a gold target and measured at 6° using the 4-by-1 mask. The 4° acceptance range was split into 8 bins and the 2 cross-sections were calculated for each bin.

The large angular resolution is thought to be partly due to the beam dispersion after the cyclotron but mostly due to the effects of aging on the avalanche counters. Studies have shown that long-term use of gas counters leads to ionization deposits on the anode wire and such surface degradation. The effects of this degradation manifest as loss of gas gain, worsened energy resolution, increased leakage current and increased chances of breakdown.

The first and last points in Figure 3.24 show the typical under- and overestimation in counting that occurs due to the edges of the 4-by-1 mask. The correction factor for the FC was calculated using the formula below and averaged over the 6 values that align with the

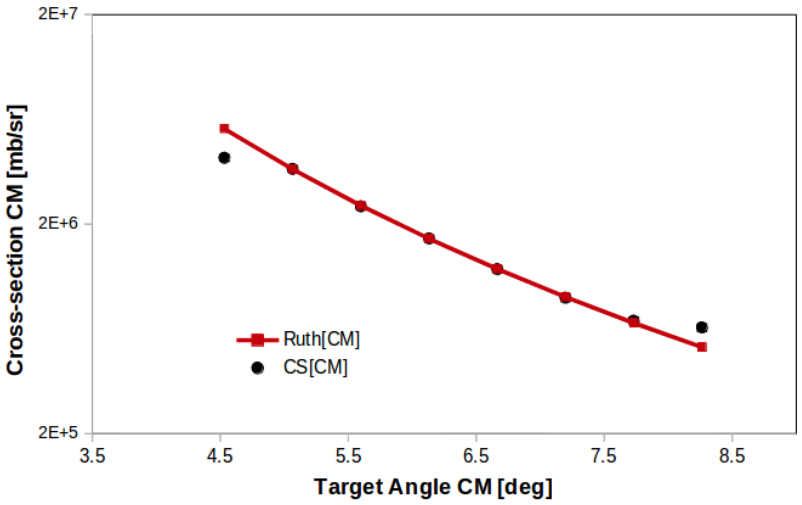

Figure 3.24: Comparison between experimental and Rutherford cross-section for FC calibration purposes. The X-axis error bars are given by the detector angular resolution of 0.52° multiplied by the statistical percentage error. The Y-axis error bars indicate the uncertainty in the experimental cross-section which is dominated by the target thickness error.

Rutherford prediction:

$$f = \frac{\sigma_{exp}}{\sigma_{Ruth}} \,. \tag{3.13}$$

Therefore, the corrected number of counts measured by the FC that was later used in the analysis in Eq. 5.4 is given by:

$$FC_{\text{corr}} = f \cdot FC_{\text{Counts}} \,. \tag{3.14}$$

The FC normalization procedure is done for each specific experiment and must be done with the FC at the position that is later used in taking reaction data.

3.2.6 Target thickness determination

The thickness of each target was determined by measuring the energy loss of charged particles in each target. Specifically, there were two methods applied. The on-line method used the projectile beam as a source of charged particles. The off-line method was done

with alpha particles from an alpha source. Each method is described in more detail below.

The off-line method

The source mentioned above contained a mix of 4 alpha-emitting nuclei:^{148}Gd, ^{239}Pu, ^{241}Am and ^{244}Cm. In order to prevent errors in determination due to particles coming at an angle (and passing through $T/\cos\theta$ instead of T), the source was collimated by placing a 2 mm thick Al mask over it, with a 1 mm diameter hole. The energy of the alphas was measured with a small silicon detector. Charge pulses were converted first to analog signals with a Mesytec charge preamplifier and then to digital signals with a pocket multichannel analyzer (MCA). The MCA was connected to a computer and the spectra were read and recorded with a software package called ADMCA. This setup is shown in Figure 3.25.

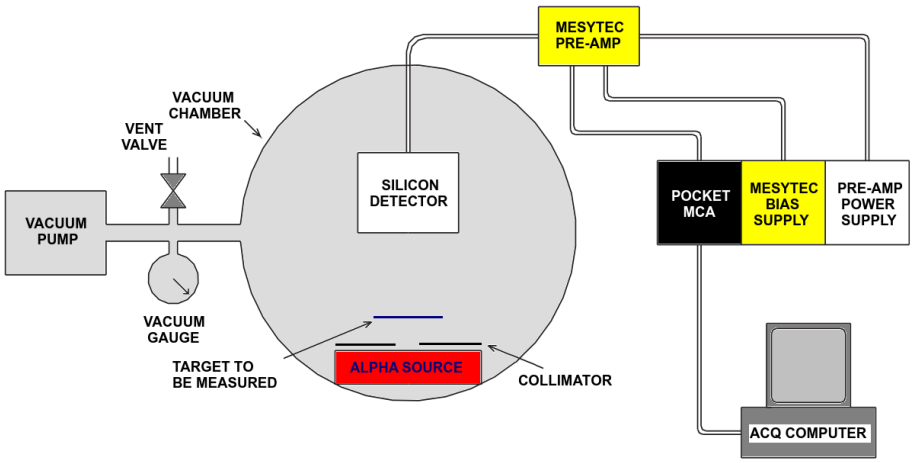

Figure 3.25: Schematic of the setup arranged for source measurements. Figure adapted from Ref. [53].

A target holder for the targets was placed between the source and the detector, as close as possible to the source, and all three were placed in vacuum. A spectrum was first taken

without any target in order to calibrate the detector and also to have a reference point for the energy loss calculation. After that, alpha spectra were taken in turn for each of the targets of interest. Figure 3.26 shows an example of the source spectrum overlapped with the one for alphas passing through Al(#1). The shift in the energy peaks due to the energy loss in the target is visible in the picture.

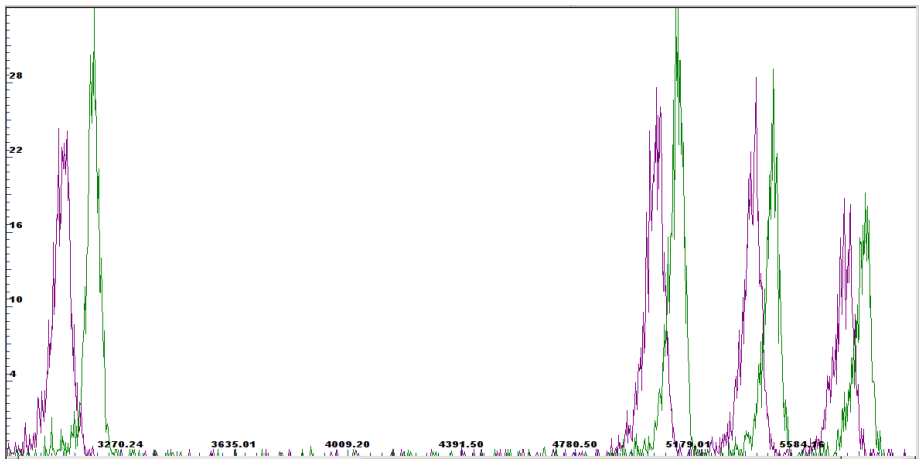

Figure 3.26: Overlapped alpha spectra when there is no target and with the target Al(#1) in the holder. Green indicates the alphas coming directly from the source, while purple is for the alphas that pass through the target.

Each of the four peaks was fitted with a Gaussian in order to obtain the centroid. The results for the energy shifts due to the 4 targets measured with this method are shown in Table 3.1. The reduction in energy measured by the detector without target is due to a protective layer of Al (1.05 μm thick) covering the detector.

Tables 3.2 through 3.5 show the energy loss in each target, labeled ΔE, and the corresponding thickness as determined with the LISE++ software [54]. It can be seen that the theoretical model used by LISE++ for particle transport through matter does not work well for the 3.2 MeV energy line as those results are in large disagreement with the other

Alpha Energy [MeV]	Energy after				
	no target	^{197}Au	^{27}Al (#1)	^{27}Al (#2)	^{27}Al (#3)
3.183	2.955	2.873	2.852	2.727	2.017
5.157	5.002	4.935	4.928	4.843	4.365
5.486	5.336	5.277	5.270	5.184	4.731
5.805	5.662	5.601	5.598	5.514	5.074

Table 3.1: Changes in each alpha energy according to the target measured.

Alpha Energy [keV]	Target ^{197}Au				
	ΔE [keV]	T [$\mu g/cm^2$]	T_{avg} [$\mu g/cm^2$]	ΔT [$\mu g/cm^2$]	$\Delta T/T_{avg}$
3182.69	77.5	271.2	200.1	16.6	8.3%
5156.59	49.1	210.4			
5485.56	41.9	185.2			
5804.77	44.8	204.7			

Table 3.2: Energy loss and corresponding thickness for the ^{197}Au target.

Alpha Energy [keV]	Target ^{27}Al (#1)				
	ΔE [keV]	T [$\mu g/cm^2$]	T_{avg} [$\mu g/cm^2$]	ΔT [$\mu g/cm^2$]	$\Delta T/T_{avg}$
3182.69	97.6	122.5	88.3	6.8	7.7%
5156.59	56.3	93.1			
5485.56	49.0	84.6			
5804.77	48.3	87.3			

Table 3.3: Energy loss and corresponding thickness for the ^{27}Al (#1) target.

Alpha Energy [keV]	Target ^{27}Al (#2)				
	ΔE [keV]	T [$\mu g/cm^2$]	T_{avg} [$\mu g/cm^2$]	ΔT [$\mu g/cm^2$]	$\Delta T/T_{avg}$
3182.69	217.2	269.4	231.3	18.5	8.0%
5156.59	140.9	231.6			
5485.56	133.4	229.1			
5804.77	129.6	233.1			

Table 3.4: Energy loss and corresponding thickness for the ^{27}Al (#2) target.

Alpha Energy [keV]	Target ^{27}Al (#3)				
	ΔE [keV]	T $[\mu g/cm^2]$	T_{avg} $[\mu g/cm^2]$	ΔT $[\mu g/cm^2]$	$\Delta T/T_{avg}$
3182.69	894.3	1044.0	974.2	81.8	8.4%
5156.59	605.4	976.7			
5485.56	578.6	968.8			
5804.77	560.2	977.1			

Table 3.5: Energy loss and corresponding thickness for the ^{27}Al (#3) target.

three. A check with the stopping range code SRIM [55] revealed the same disagreement between the 3.2 MeV determination and the 5-6 MeV ones. As such, the final thickness result shown in column 4 of each table was determined as an average of only the 3 numbers corresponding to the 5-6 MeV energies. The error of the mean was calculated with the standard method for small data sets, using the formula below:

$$\Delta\bar{T}_{\text{avg}} = \frac{T_{\text{max}} - T_{\text{min}}}{2\sqrt{N(=3)}}\,. \tag{3.15}$$

To this error, an uncertainty of 2% was added to account for the statistical errors, as well as 7% for target non-uniformities and 1.5% for uncertainties due to the model of energy loss in matter. Straggling was also accounted for, based on each energy. Columns 5 and 6 in each table reflect the total uncertainty (absolute and percent) for the corresponding target.

The on-line method

The in-beam method is also sometimes called the 'double-target' method. In this case, the first step was to have the projectile beam pass through a gold target and record a spectrum of the focal plane. Figure 3.27, (a), shows one such plot for a beam of ^{13}C. The elastic scattering peak present was fitted with a Gaussian shape to obtain the centroid. The second step was to place the target of interest in front of the gold target and have the beam

pass through both of them. The peak in the focal plane spectrum showed a shift reflecting the energy lost by the beam in the target needed to be measured, as illustrated in Figure 3.27, (b).

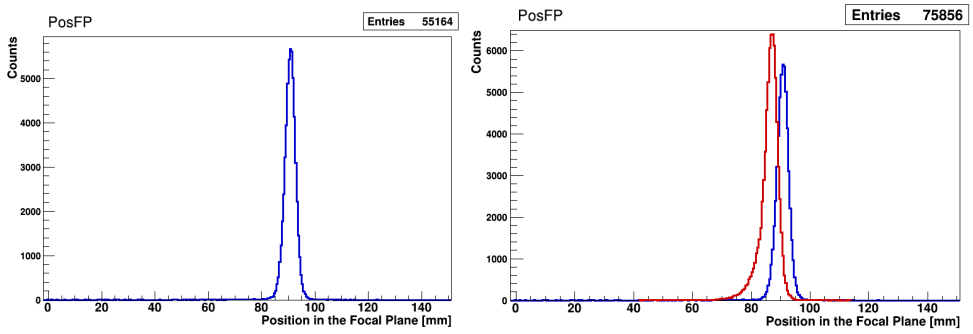

(a) (b)

Figure 3.27: Focal plane spectra for target thickness determination with ^{13}C beam. (a) Spectrum corresponding to the gold target on its own. (b) Overlapped spectra showing the shift in energy due to the presence of an aluminum target (red) in front of the gold one (blue).

The linear dependence of the beam energy on the focal plane position was determined with RAYTRACE. The ΔE obtained was then used with LISE++ to determine the thickness of the target. This method was applied to the 3 targets listed in table 3.6. For the ^{13}C target, the procedure worked as expected and the result is presented in the table. A test of uniformity was performed as well for this target, by putting the beam through a spot above the center and then below the center. This test revealed an uncertainty in the thickness determination due to non-uniformity of ∼7%. This uncertainty has been applied to all thickness determinations where the test wasn't done to account for possible non-uniformities in each target.

For both ^{27}Al targets, there were some issues with the data. Specifically, when the beam was sent through both Al and Au foils it seemed to produce a secondary peak and

not just the expected shift in the elastic peak. Figure 3.28 shows this phenomenon for the ^{27}Al (#2) target. The plot on left, (a), shows the data in focal plane position versus target angle with a second band corresponding to the second peak visible at the larger angles. The slight bend to the lines is an artifact of the RAYTRACE reconstruction. The plot on the right, (b), is a closer view of the red spectrum from Figure 3.27, (b), showing the tail trailing towards the lower positions corresponding to the second peak.

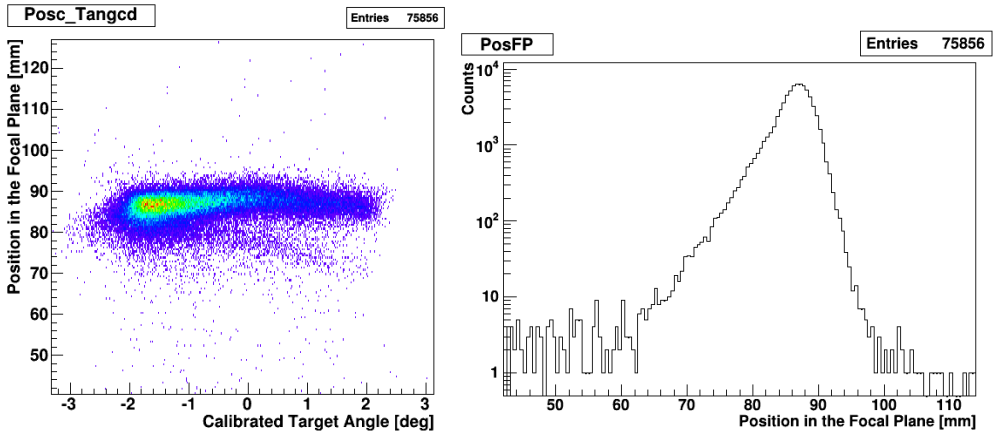

(a) (b)

Figure 3.28: (a) Spectrum showing data in a focal plane position versus target angle plot corresponding to the beam passing through the ^{27}Al (#2) target and scattering off the gold foil behind it. (b) Focal plane position spectrum showing the data in (a) projected on the Y-axis, with the second band appearing as a tail of the main peak.

It is uncertain where this second peak comes from. The fact that it appeared after the Al target was set in front of the Au foil suggests that the peak might be caused by scattering off of an impurity in the target. A rough estimation of the contamination percentage gives the value of 0.2% which disagrees with the material specifications of the Al sheet that the target was made of. Another possibility is that the distance between the Al and Au foils was large enough for the ^{12}C reaction product off of ^{27}Al to cause its own Rutherford

Target Name	Projectile Beam	ΔE [keV]	T_{avg} $[\mu g/cm^2]$	ΔT $[\mu g/cm^2]$	$\Delta T/T_{avg}$
^{13}C	^{27}Al	508.9	91.8	6.9	7.5%
^{27}Al (#2)	^{13}C	320.2	266.9	20.8	7.8%
^{27}Al (#3)	^{13}C	1053.3	983.9	69.4	7.1%

Table 3.6: Results for target thicknesses determined with a beam of projectiles.

Target	Online $[\mu g/cm^2]$	Offline $[\mu g/cm^2]$	Weighted Average $[\mu g/cm^2]$
^{13}C	91.8 ±6.9	not measured	91.8 ±6.9
^{27}Al (#1)	not measured	88.3 ±6.8	88.3 ±6.8
^{27}Al (#2)	266.9 ±20.8	231.3 ±18.5	247.0 ±13.8
^{27}Al (#3)	983.9 ±69.4	974.2 ±81.8	979.8 ±52.9
^{197}Au	not measured	200.1 ±16.6	200.1 ±16.6

Table 3.7: Summary of the target thicknesses measurements results.

scattering on gold. However, RAYTRACE calculations disprove this theory.

Unable to determine the cause of this second peak, it was decided to proceed with the target thickness determination by only considering the main peak. The angular range was divided into 8 bins that were used to obtain 8 independent evaluations of the thickness. The average result is presented in Table 3.6 along with similar results for the other two targets.

Table 3.7 shows a summary of the results obtained with both methods used to determine a target's thickness. It can be seen that the on-line and off-line values for ^{27}Al (#2) are rather different, even though they agree within the error ranges. It is very likely that the source of the double-peak phenomenon is responsible for that. However this discrepancy didn't occur for the ^{27}Al (#3) target, a fact that is inconsistent with this assumption. Therefore, this discrepancy in thickness evaluations was kept in mind as a possible source of similar discrepancies in the reaction data.

3.2.7 Particle identification

There are three types of figures that can be used to identify the particles of interest. The first is a plot of the energy lost as the particles travel through the detector gas versus the stopping energy left in the scintillator (PM). Figure 3.29 shows an example of such a particle identification (PID) plot, where the energy loss data come from the dE1 signal.

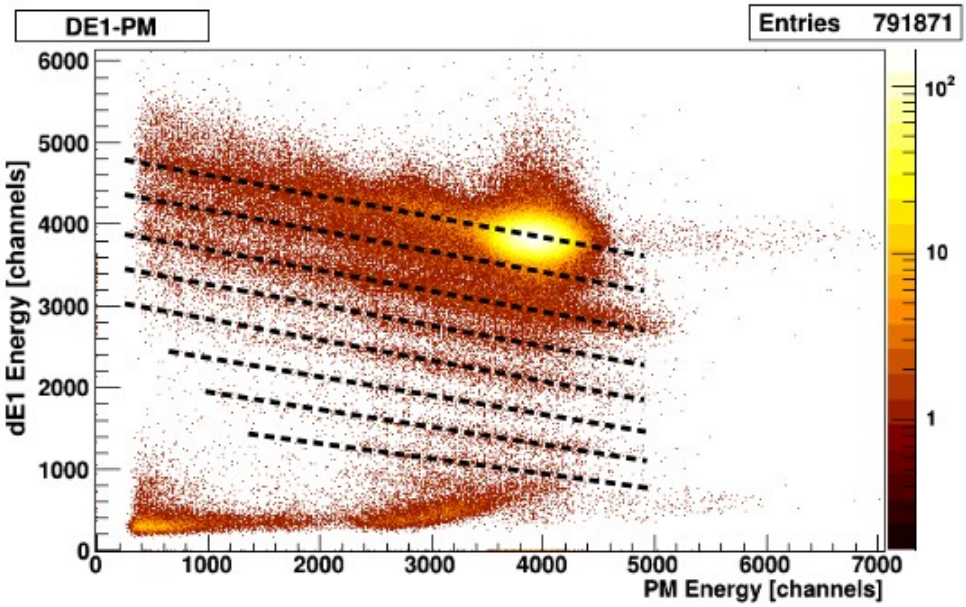

Figure 3.29: Particle identification plot of the dE-PM type. The data in this figure come from a ^{28}Si beam on a ^{13}C target. The energy loss information is given by the dE1 signal. The different black dashed lines indicate isotopes of different Z with the topmost line being Z=14.

The resolution of dE1 in this example, ^{28}Si beam on a ^{13}C target, isn't very good but it can still be seen that nuclei with the same proton number (Z) form bands roughly parallel to the horizontal axis. The topmost Z-band most often corresponds to the primary beam. Figure 3.30 shows two other examples of this type of plot. In (a), the energy loss information comes from the Micromegas anode signal (E_{MuO}), while in (b) the Y-axis

indicates the sum of the dE1 and E_{MuO} signals.

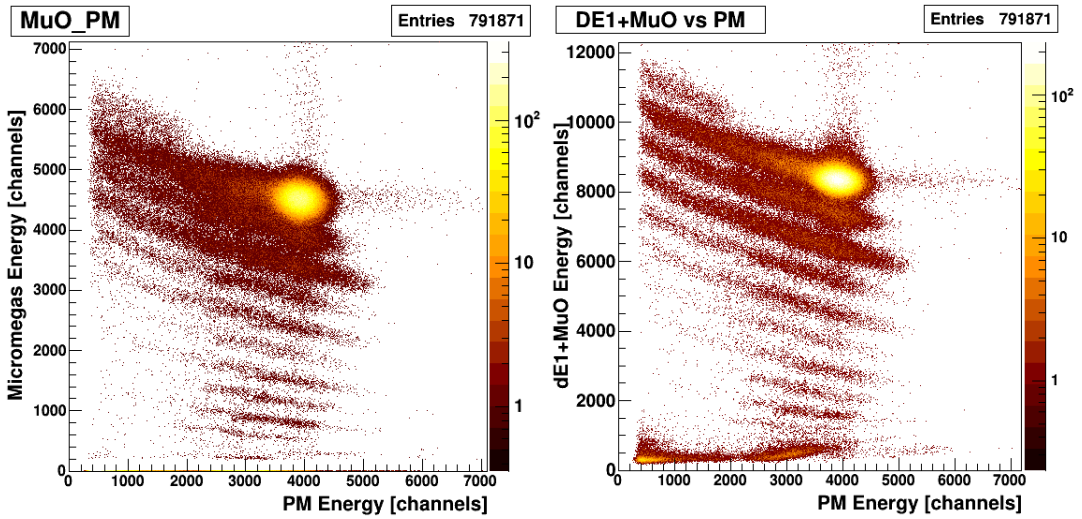

(a) (b)

Figure 3.30: Particle identification plots of the dE-PM type with data from a ^{28}Si beam on a ^{13}C target. (a) Micromegas energy versus PM energy. (b) Sum of dE1 and Micromegas energy signals versus PM energy.

The second method to determine the type of particles detected involves plotting the data in a 2-D histogram of position in the focal plane versus energy. The energy information can come from a ΔE energy loss signal (dE1, E_{MuO}, dE1+E_{MuO} or even the wire energy) or the stopping energy (PM). Figure 3.31 shows an example of this type of plot using the sum of the dE1 and E_{MuO} signals. Here, the roughly vertical bands correspond to specific nuclides and the horizontal bands correspond to excitation states in those nuclides. It can be seen that the data that overlap in ΔE become separated due to the added position criteria.

Usually, the analysis procedure involves using a first gate on the Z-band of interest in the ΔE-PM figure. The data inside that gate are then plotted in a position versus ΔE

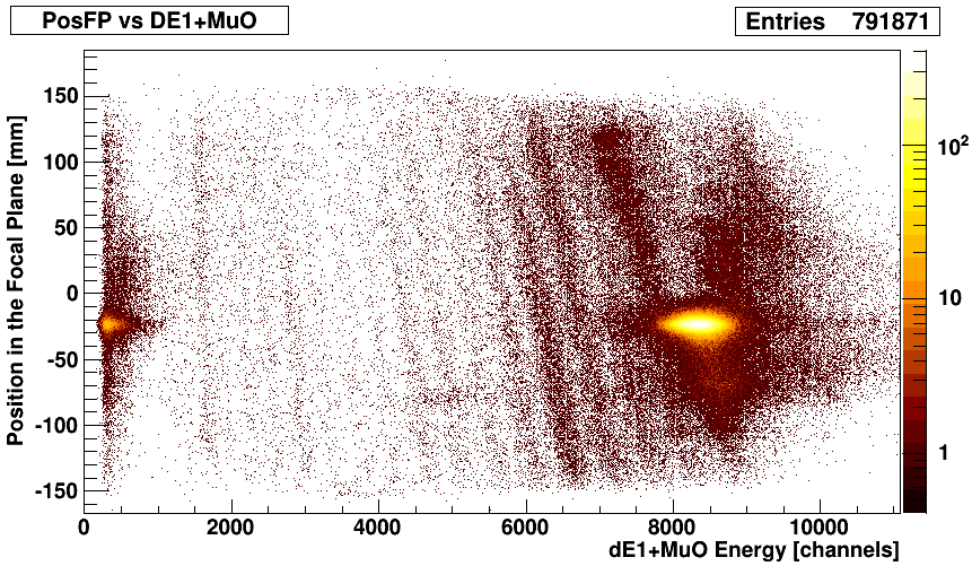

Figure 3.31: Particle identification plot of the PosFP-E type. The data in this figure come from the same ^{28}Si beam on a ^{13}C target as before. The energy information on the X-axis is given by the sum of the dE1 and Micromegas energy signals. The Y-axis shows the position of each particle in the focal plane.

histogram. This allows us to choose the specific isotope we need. However, the specifics of each PID selection used for analysis will be presented in chapter 5.

4. OXFORD DETECTOR UPGRADE TESTING AND RESULTS

In order to characterize the new Micromegas component, it was necessary to study the performance of the upgraded detector under different experimental conditions, as well as determine the limits of operation. In particular, it was important to determine the gain and energy resolution of the Micromegas and evaluate these parameters in relation to the original detector performance.

The gain of the Micromegas is given by the ratio between the number of electrons collected and the number of electrons produced in the initial gas ionization process. The gain depends on various factors that affect these two numbers, like gas mixture, gas pressure, energy and type of ionizing particle, amplification field and amplification gap.

The intrinsic energy resolution is a measure of the fluctuations in the number of secondary electrons created. It provides a way to characterize how precisely the detector can determine the energy deposited by the ionizing particle.

As mentioned in the previous chapter, the Oxford detector upgrade was tested off-line, as well as on-line with a variety of beams. Specifically, there were 7 beams used, ^{16}O, ^{22}Ne, ^{26}Mg, ^{27}Al, ^{28}Si and ^{32}S. In each case, the beam energy was approximately 12 MeV/A and the main target was ^{197}Au. The gas mixture used was isobutane and remained unchanged throughout the testing. Additionally, the amplification gap in the Micromegas was not changed from 256 μm.

The elastically scattered beam was collimated with the single slit corresponding to an opening angle of 0.1°. The Micromegas response was plotted in individual pad histograms containing the raw data (Figure 4.1, a-d), as well as a 2D histogram called 'Micromegas Hitmap' showing the particle track through that gas region of the detector (Figure 4.2).

From these histograms, others were derived as necessary and will be explained as they

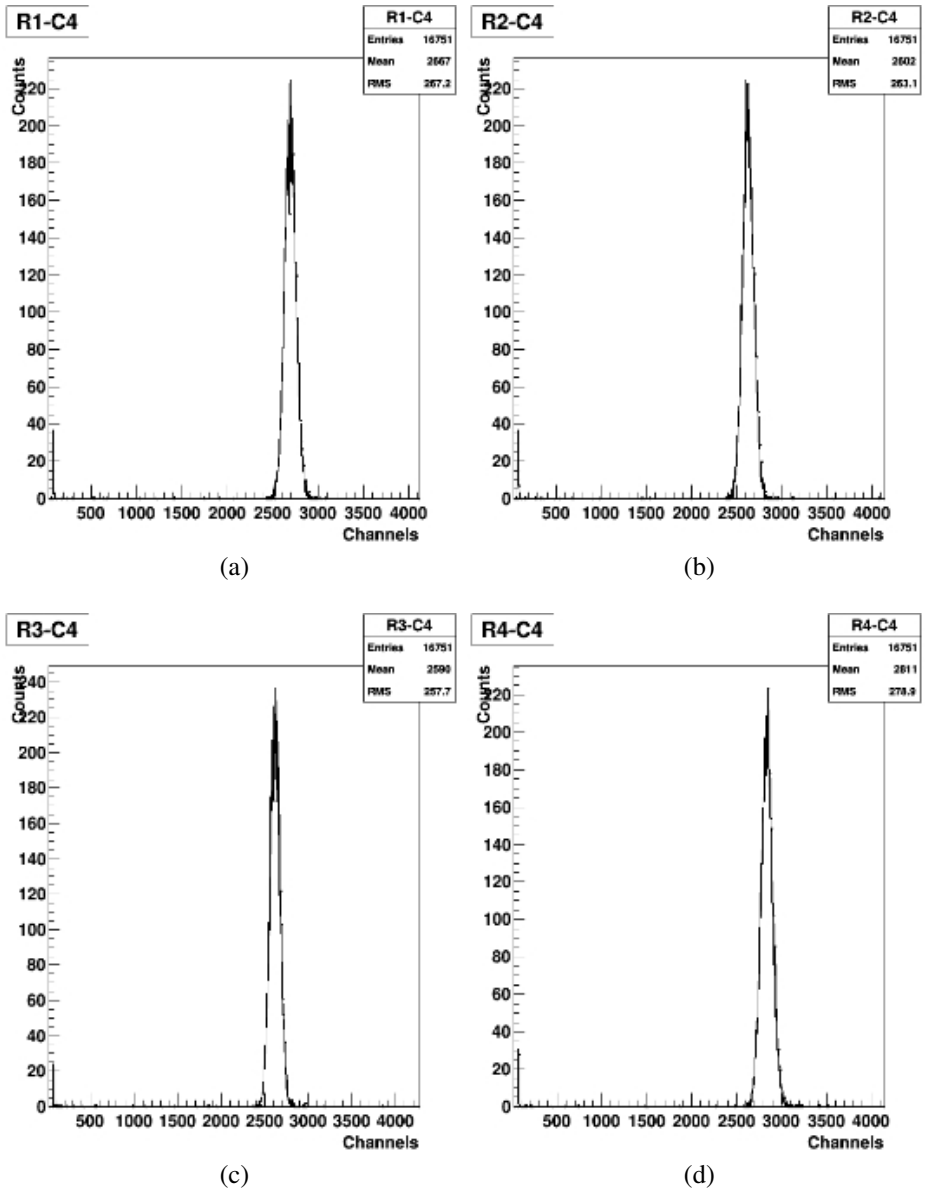

Figure 4.1: (a-d) Individual raw histograms for the Micromegas pads in column 4.

appear in the text. Throughout this chapter, individual pads will be referred to according to their row and column, for ex. R1-C1 represents the pad in row 1 and column 1.

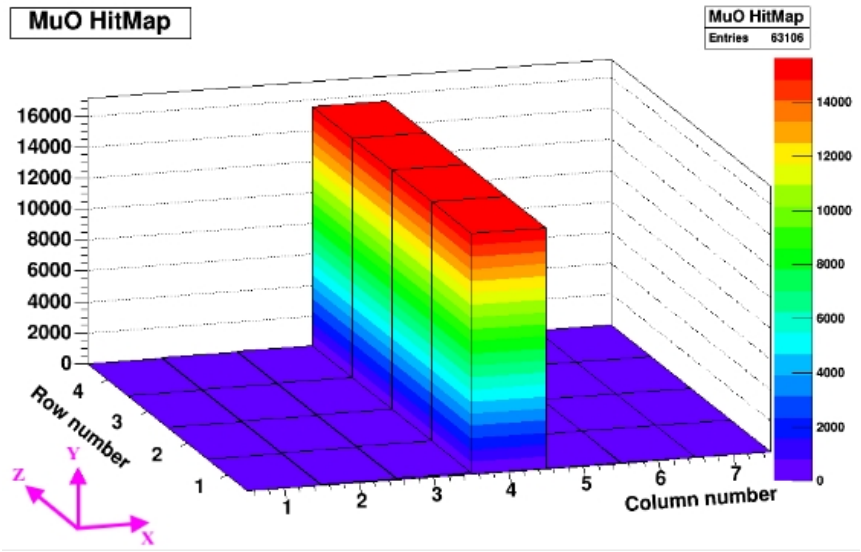

Figure 4.2: 3-D map of the column 4 pads 'hit' as a ^{16}O beam passes through the gas.

Throughout the following analysis, the pressure values mentioned are actually assumed values. The pressure gauge used in the experiments suffered a change in calibration that occurred very slowly over a period of years and was only discovered very recently. The true values are off by $\approx$ -15 Torr. However, the assumed values have been kept in the analysis as they don't affect the relative response of the Micromegas outside the breakdown region (which is around 5-10 Torr).

4.1 Off-line Tests

The electronic noise was one of the main points of concern and focus in the pre-experiment setup and testing. At the design level, the connections between the pads and the preamplifiers were made as short as possible in order to minimize noise pick-up in connector cables.

With the Oxford detector connected to the beam-line and the magnets powered on, there was a noise level between 10-50 mV, at minimal electronic gain. This showed up in the pad histograms as a pedestal at $\sim$100 channels. In the beginning of the testing,

the noise was sometimes up to 400 mV. The source in those cases was bad shielding or terminations that were not properly grounded.

Additionally, it was observed that grounding the mesh with a terminator that had even 50 Ω of resistance would add to the noise as well as affect the pad signals. Specifically, a pad 'hit' signal would produce reflected signals in all the other pads of amplitude $\sim$1/20 of the original. This was not an outcome that could be tolerated as it significantly affected the reconstruction process in the case of charge sharing between pads. But this phenomenon will be explained in more detail later in this chapter.

4.1.1 *Electronic chain calibration*

It is important to know the gas gains that the Micromegas pads can provide. However, it is impossible to determine an absolute measure of the charge created in the amplification process. So instead, the gain of each pad was estimated based on an off-line procedure that attempted to obtain a correlation between an 'ionization event' and the system response to it. This calibration was obtained using a series of pulser signals of different amplitudes sent through a 25 pF capacitor (with 10% tolerance) into the mesh. As the detector-electronics system responds differently to the pulser and the actual ionization process, this provides only a relative calibration. An example of the pad histograms obtained with this procedure is shown in Figure 4.3.

Each of the peaks was fit with a Gaussian and the position in channels was recorded. This was done for all the pads. Figure 4.4 shows the calibration plots for the 4 pads in the central column as they will be the most significant in the later analysis results.

This calibration was done for the case where the electronic shaper gain was 2. Figure 4.5 shows a similar calibration done for shaper gain 8. These plots will be the only ones included here as they were the only amplifier settings used in these experiments.

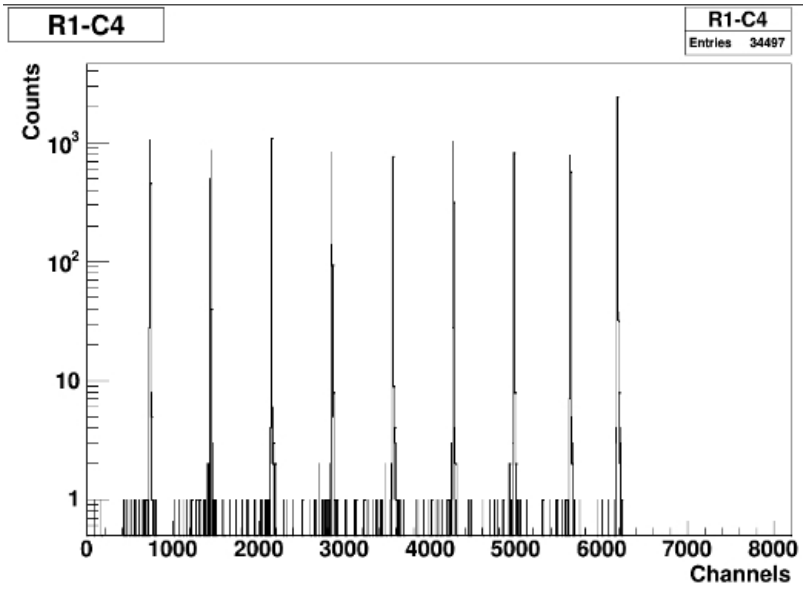

Figure 4.3: Pulser data recorded by pad R1-C4. Amplifier settings were CG=2, FG=1.

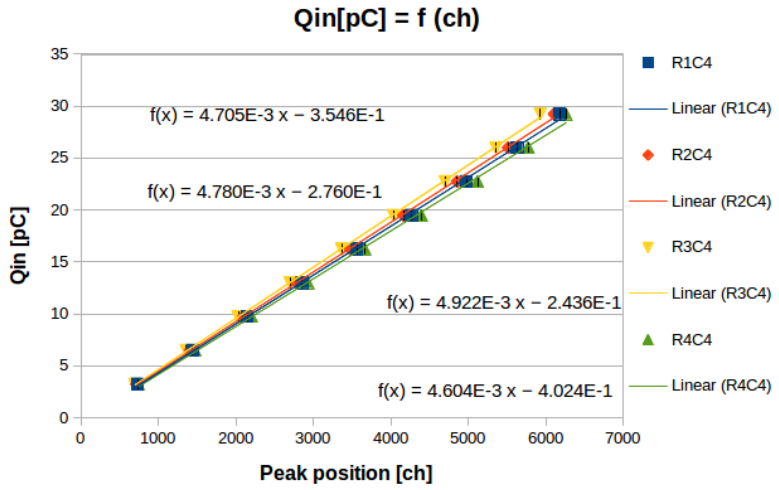

Figure 4.4: Calibration plot showing the pulser data for the central pads and the respective linear calibrations when the shaper gain is 2. The X-axis error bars indicate statistical uncertainties. There is a vertical scale uncertainty of 10% due to the capacitor tolerance.

4.1.2 *Source test*

The first test with particles was done using a mixed alpha source containing the decaying nuclei ^{148}Gd, ^{239}Pu, ^{241}Am and ^{244}Cm. Due to the design of the Oxford detector, the

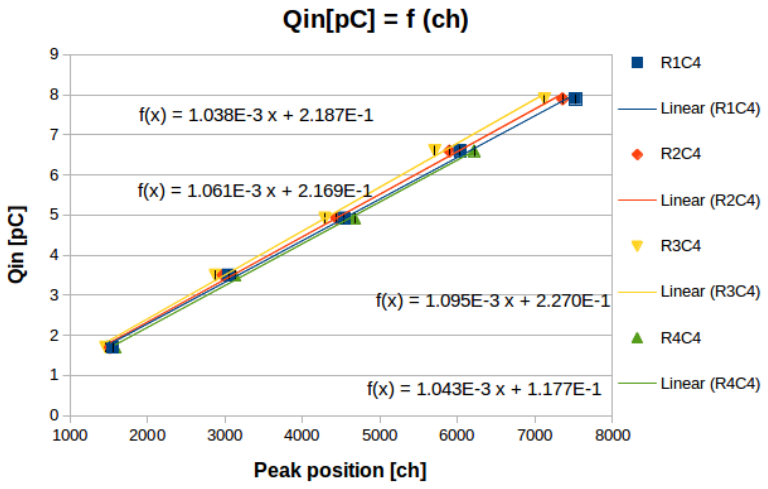

Figure 4.5: Calibration plot showing the pulser data for the central pads and the respective linear calibrations when the shaper gain is 8. The X-axis error bars indicate statistical uncertainties. There is a vertical scale uncertainty of 10% due to the capacitor tolerance.

source could not be used to thoroughly test every pad as there was no location inside the detector where it could be safely mounted. The closest possible position was at the rear of the chamber but even there, the back bank of wires that are part of the Faraday cage made it such that the source was still ∼4 cm from the edge of row 4 of pads.

Therefore, the source was used to see if the Micromegas anode would work at a minimal level under the conditions required for beam testing. The Oxford detector was filled with isobutane gas at 100 Torr, the starting pressure for the on-line testing. The alpha particles emitted by the source have energies between 3 and 6 MeV, leading to energy losses in the pad region, from 0 to 3 MeV, similar to what is expected with the beams. The source was placed in a central position vertically, as well as horizontally, and was collimated with a 2 mm (diameter) circular opening.

The cathode was biased to -1000 V. As part of the voltage divider, the FG received a voltage of ∼300 V, creating a drift field just below the mesh of ∼200 V/cm. The shaper gain was set to 2 and the electronic shaping time was 1 µs. The response of pad R4-C4

with increasing bias is shown in Figure 4.6. It can be seen that avalanches start forming in the amplification gap around 250 V – 270 V.

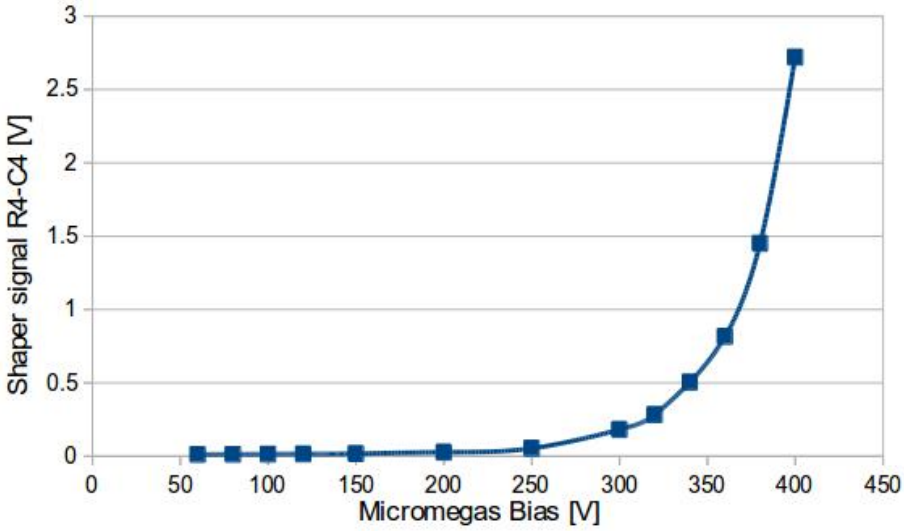

Figure 4.6: Plot showing the variation of the electronic shaper output signal with anode bias for pad R4-C4.

The final voltage on the pads was +400 V and the amplification field was ∼16 kV/cm. Figure 4.7 shows the Hitmap histogram after ∼30 minutes of data acquisition, as well as an approximate position of the source (indicated in gray). The asymmetry in the pads response indicates that pad R3-C5 may not be working properly.

It can be seen that the alpha particles lose their energy before reaching row 1 and only the ones traveling the shortest path reach row 2 (only those along column 4). Calculations done with SRIM for the 4 main peaks agree with this finding. Specifically, Figure 4.8 shows the corresponding plots for the energy lost at each depth in the detector, beginning with the dead region between the source and the active Micromegas area and ending with row 1.

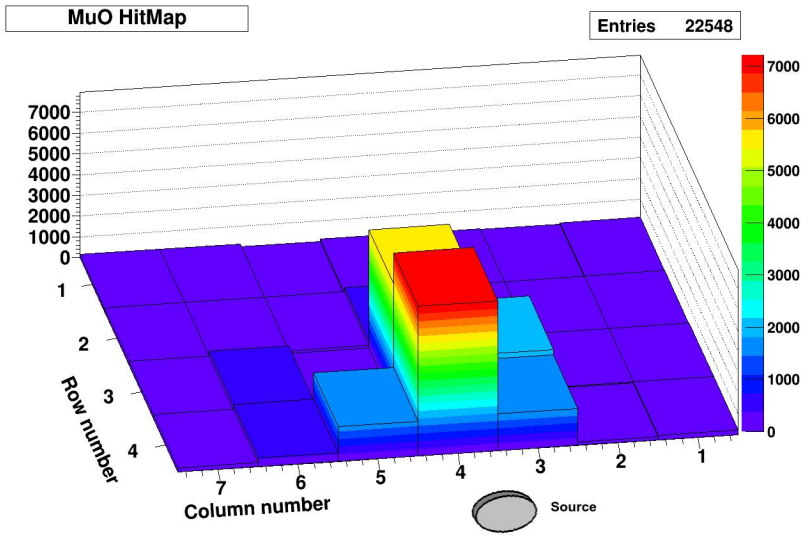

Figure 4.7: 2-D histogram showing the pads that detect alpha particles as well as an approximate position of the source.

The dashed lines in these plots denote the borders between regions for a path that is perpendicular to the rows. However, particles are emitted in a $\sim$30° cone. Consequently, for each alpha particle energy there will be a range of path lengths in each pad that is 'hit'. Figure 4.9 illustrates this phenomenon more clearly. The four different colors, black, green, orange and blue, correspond to the four most intense alpha particle lines. Each of the arcs indicates the stopping range for its respective energy, for the angular opening of the collimator.

The 5.8 MeV (black) alpha particles that reach row 2 lose energies between 0 and 1 MeV in that region of the gas. For row 3, the range is 2.1 – 2.5 MeV and for row 4, it is 1.4 – 1.8 MeV. These ranges are similar for the 5.5 MeV and 5.2 MeV alpha particles as well. The 3.2 MeV decays from ^{148}Gd barely reach row 4 as can be seen in Figure 4.8 (a) and Figure 4.9. Having these calculations helps us better understand the individual pad histograms obtained. Specifically, for pad R3-C4 (Figure 4.10, (a)), where most alpha particles stop, this variation in path length results in a tail on the low energy side for each

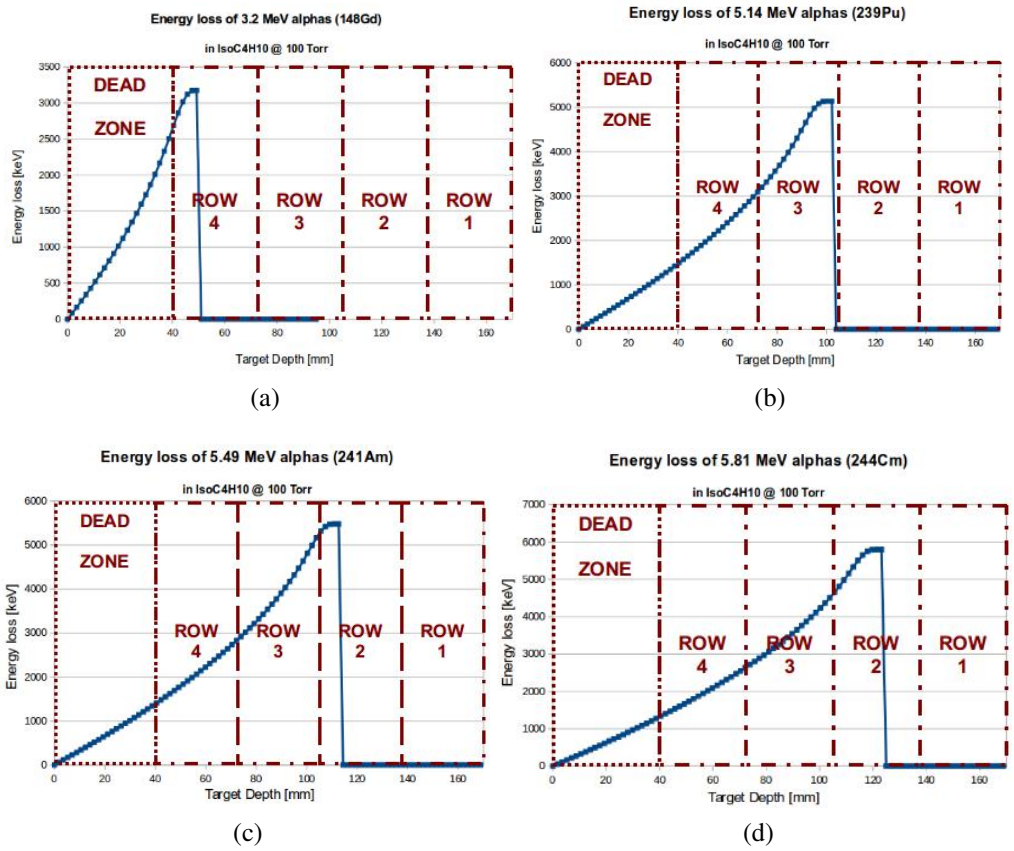

Figure 4.8: (a-d) SRIM simulations of energy loss in the Micromegas anode for the 4 alpha energies needed. The X-axis denotes the depth inside the detector. The Y-axis indicates the energy lost by the time particles reach each depth point.

peak. For pad R4-C4 (Figure 4.10, (b)), where the higher energy alpha particles (5-6 MeV) pass through without exception, the peaks are close together and overlap. On the other hand, the 3.2 MeV alphas appear as a trail in the low channel region.

In order to minimize this effect, a gate can be set in the analysis software to contain only 'events' with multiplicity 1 per row. These are the particles that leave energy only in one pad as they cross a row. Figure 4.11 shows the histogram for pad R3-C4 with this condition.

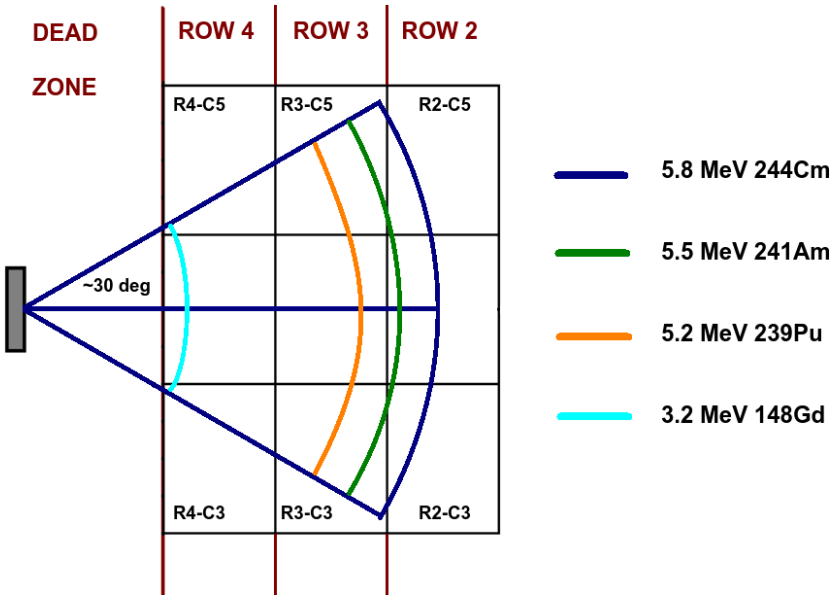

Figure 4.9: Schematic drawing of the source position with respect to the central pads showing the paths of the alpha particles. The circular arcs indicate the stopping range for the different energies as indicated in the color legend.

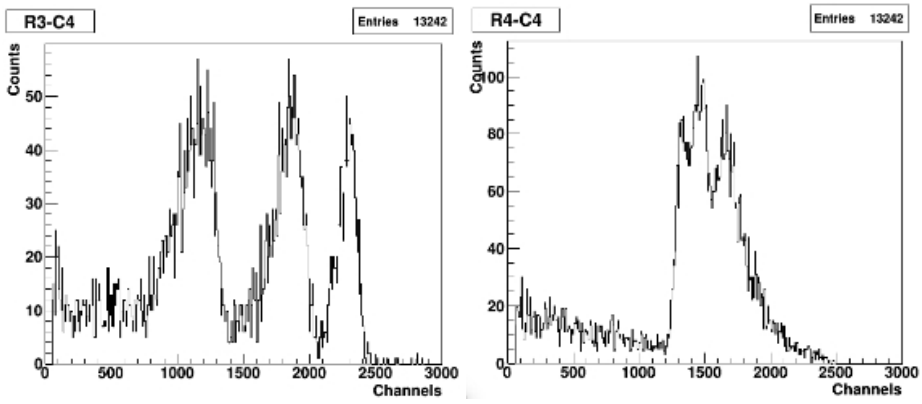

(a) (b)

Figure 4.10: (a) Raw energy loss data collected by the pad R3-C4. (b) Raw energy loss data collected by the pad R4-C4.

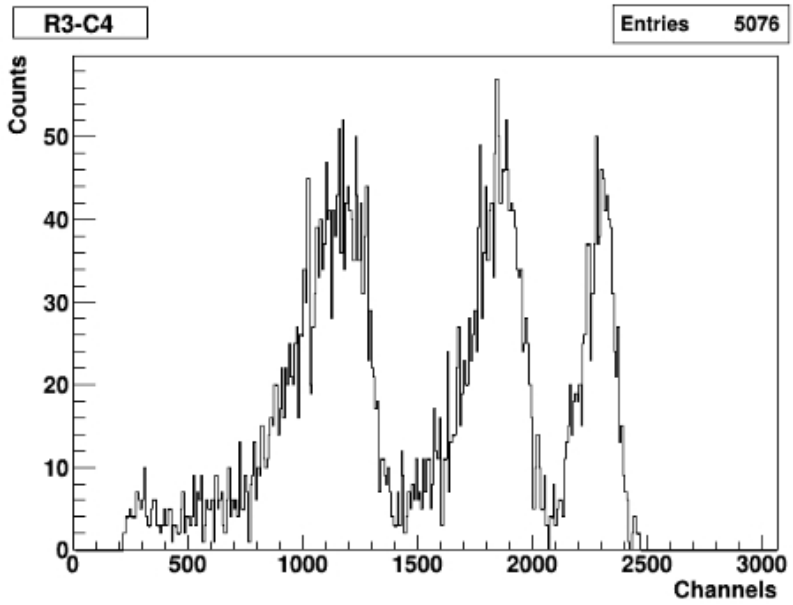

Figure 4.11: Pad R3-C4 histogram after setting a condition for multiplicity=1.

4.2 On-line Tests

The signal induced on the Micromegas pads has two components, the ion and electron signals. The main contribution comes from the drifting motion of the positive ions towards the micromesh in the amplification gap. Looking at the signal through the charge preamplifier (MPR-16, 12 ns rise time) we found that the rise time for the gas signal is $\sim$100–150 ns, as expected for isobutane and a 256 μm gap. Further shaping with a charge amplifier (1 μs) gave signals as in Figure 4.12. The output signals from each of the two amplifiers used are shown in cyan and green. An example of the distributions produced after the analog-to-digital conversion is shown in Figure 4.13. Each histogram shows the response of pad R1-C4 to different ionizing particles. The specific voltage and gas settings in each case are indicated in their picture.

It can be seen that histograms (a) and (b) show peaks that can be fit very well with a Gaussian distribution. On the other hand histograms (c) and (d) show peaks with a tail on

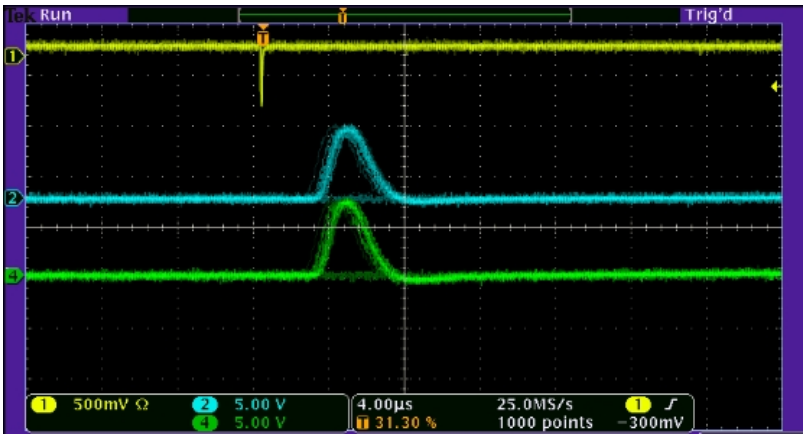

Figure 4.12: Oscilloscope screenshot taken on-line (from a ^{28}Si beam) showing an example of the two output signals from the two charge amplifiers, specifically representing pads R1-C4 and R4-C4.

the low energy side. This could be a sign of incomplete charge collection which could be due to recombination or a consequence of the support pillars placed between the mesh and the anode pads.

However, since the Micromegas anode plate used in all the experiments was the same and the top two histograms in Figure 4.13 do not show a tail, the pillars can be excluded as the cause. By process of elimination, the only difference found between the four setups was the bottle of isobutane gas used and the time available to outgas the Oxford chamber prior to the experiment. Therefore, the low-energy tail is most likely an effect of recombination due to a larger amount of oxygen contaminating the gas.

For reference purposes in the remaining results section, Table 4.1 contains the average energy lost per pad in the gas area of the Micromegas by every beam used according to the pressure conditions. These values were obtained with LISE and they take into account the energy lost in the Oxford detector elements that precede the Micromegas.

Beam	Pressure [Torr]				
	30	50	70	85	100
	Energy loss [MeV]				
^{16}O	-	-	-	-	3.82
^{22}Ne	1.52	2.64	3.88	4.92	6.16
^{26}Mg	2.19	-	-	-	-
^{27}Al	-	4.51	-	-	-
^{28}Si	2.92	-	8.09	-	-
^{32}S	3.91	6.72	-	-	-

Table 4.1: Average energy loss per pad in the Micromegas section for the different test beams used and the different pressure conditions.

4.2.1 *Efficiency*

The detection efficiency was evaluated as the ratio between the counts recorded by the Micromegas pads and the counts detected by dE1 (the ionization detection region of the Oxford detector). Noise related counts are excluded. This ratio can be seen as a relative efficiency since it depends on the performance of the dE1 component of the Oxford detector.

Figure 4.14 shows the efficiency of pad R1-C4 as a function of the bias voltage for two different situations, elastically scattered ^{16}O particles passing through isobutane at 100 Torr and ^{28}Si particles passing through isobutane at 70 Torr. It can be seen that the efficiency is close to 100% for the large range of 100–300 V, independent of the gas pressure. The Y-axis error bars indicate statistical uncertainties. When the error bars are positive and the efficiency exceeds 100%, it can indicate a situation where dE1 is less efficient than the Micromegas pads.

4.2.2 *Uniformity*

The uniformity of the detector response across the Micromegas anode was done by sweeping the beam: changing the magnetic field from higher values to lower values such

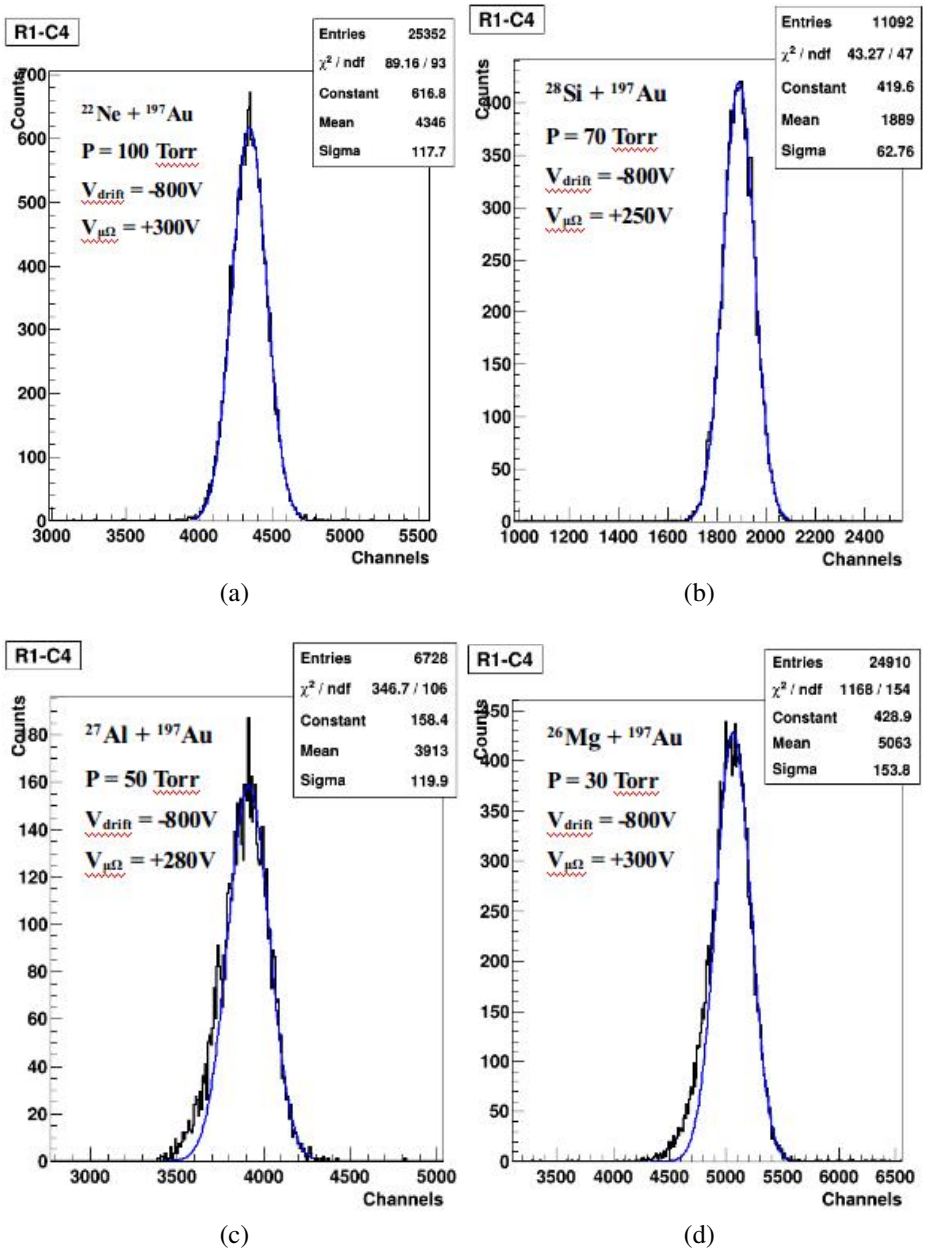

Figure 4.13: R1-C4 pad response for different ionizing particles and different pressures.

that the collimated beam would pass through the gas region corresponding to a single column at a time. For each of the 4 rows, the peak position in each of the 7 pads was

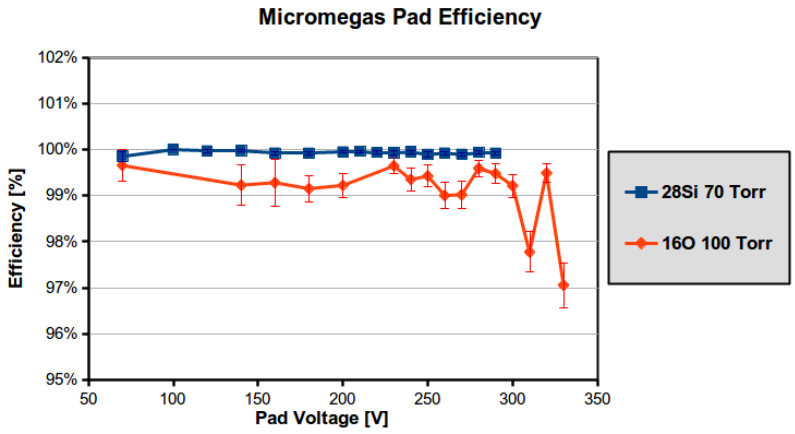

Figure 4.14: Detection efficiency of pad R1-C4 depending on bias voltage for 2 different cases, ^{16}O particles in isobutane at 100 Torr and ^{28}Si particles in isobutane at 70 Torr. The Y-axis error bars indicate statistical uncertainties.

recorded and compared to the central pad in the respective row. Figure 4.15 below shows a plot of the differences in individual pad responses for the beams ^{16}O, ^{22}Ne, ^{27}Al and ^{28}Si. The variations in response from pad to pad in each row are within ±8% relative to the center pad for the respective row and could indicate a number of non-uniformity sources. One possibility is that the amplification gap is not constant across the anode leading to variations in the gas gain. Related to that, the gain fluctuations could also be a consequence of incomplete charge collection due to the support pillars. The discrepancies could also be due to slight differences in the chain of electronics from one pad/channel to another.

The least likely source is the gas pressure, as it was constantly monitored during the testing and the fluctuations never exceeded ±0.5 Torr. Moreover, the fluctuations would have affected all the pads across the anode in a consistent manner. Most likely, it is a combination of the other three factors mentioned with gap non-uniformity playing the major role. Since a variation of ±8% can have a significant impact on the resolution of the energy peak corresponding to the entire anode, it is important to correct for this in the

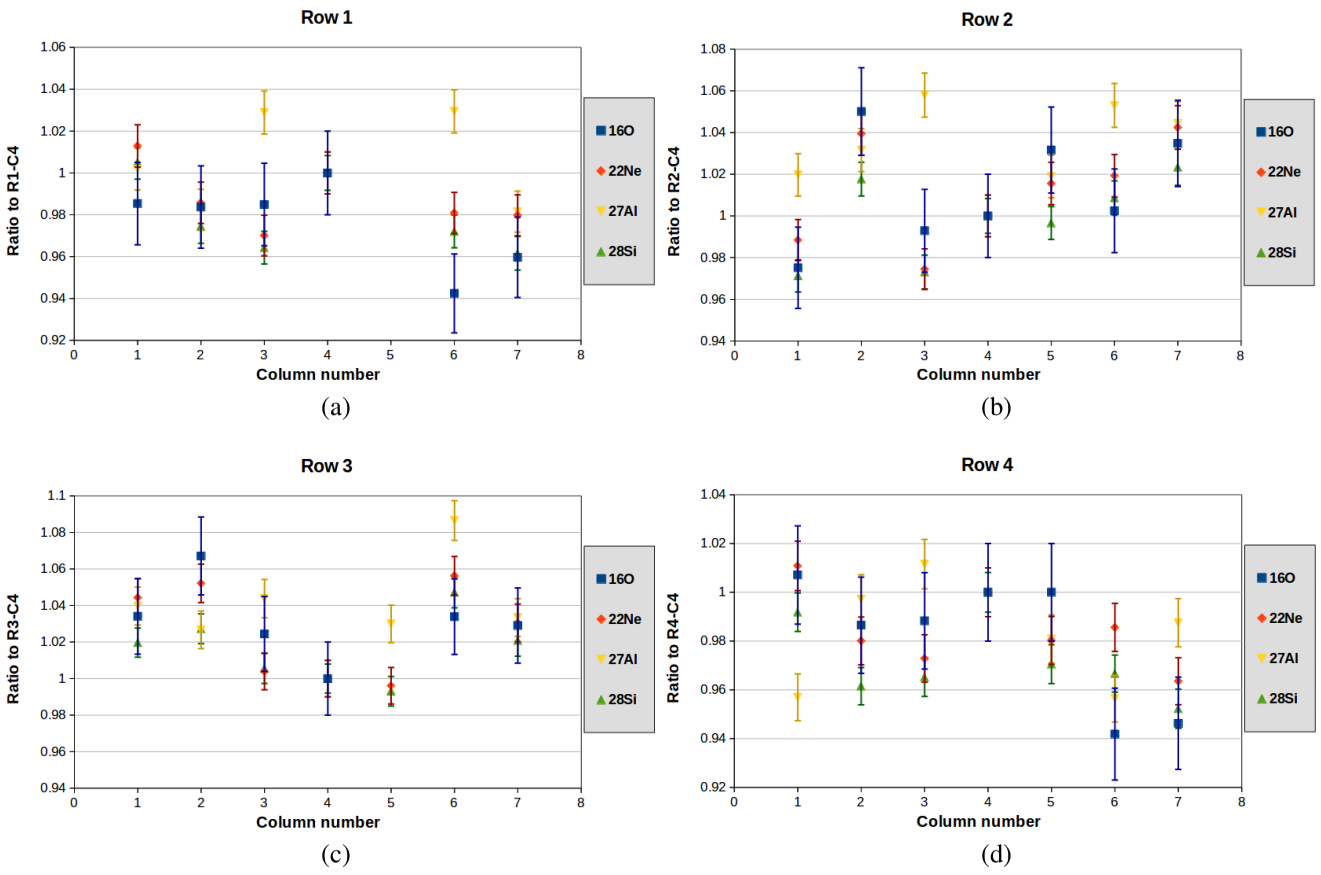

Figure 4.15: (a-d) Variation in pad response across the anode for Row1–Row4 for 4 different beams elastically scattered on gold: (navy) ^{16}O at 100 Torr, (red) ^{22}Ne at 100 Torr, (yellow) ^{27}Al at 50 Torr and (green) ^{28}Si at 30 Torr. The Y-axis error bars indicate statistical uncertainties.

acquisition software. Therefore, the beam sweep is a necessary step in the preliminary stage of an experiment.

4.2.3 *Linearity*

In order to observe the linearity of the Micromegas response, it was necessary to have different amounts of the energy deposited in the gas. The method used to study this characteristic involved impacting the beam on a ^{13}C target. The result was a cocktail of reaction products, as can be seen in Figure 4.16. The left picture shows a 2-D histogram with row 2 response on the Y-axis and residual energy (detected with the photomultipliers) on the X-axis. The right picture shows another 2-D identification plot with row 2 response on the X-axis and position of particle in the focal plane on the Y-axis.

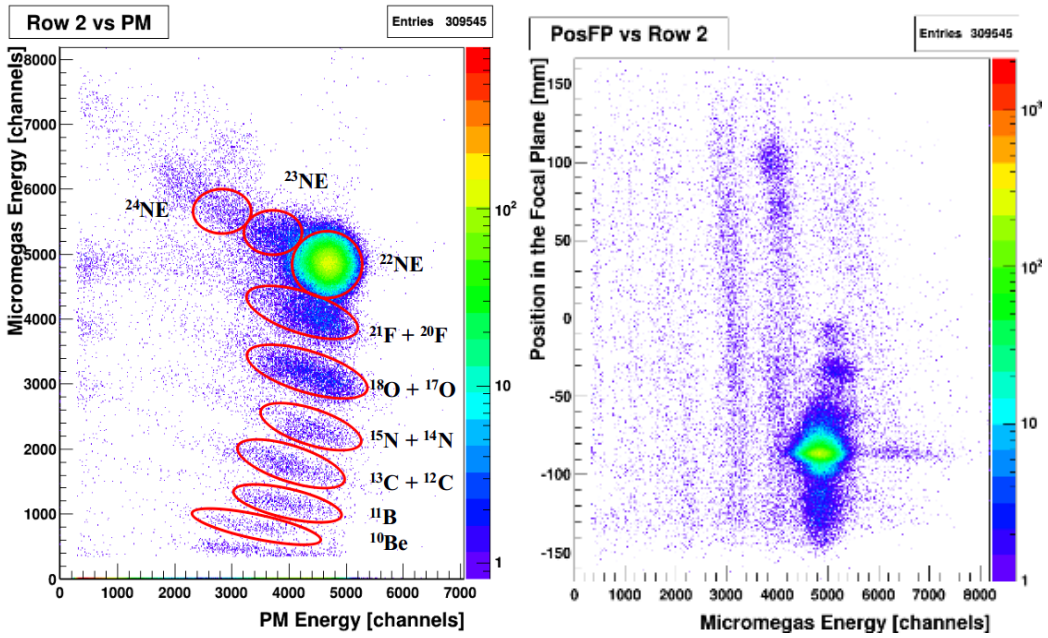

Figure 4.16: (a) Micromegas row 2 energy versus residual energy. (b) Particle position in the focal plane versus particle energy detected with Micromegas row 2.

The primary beam in this specific case was ^{22}Ne and the gas pressure was 30 Torr. The various reaction products are indicated in the pictures. Each circle of events was separated with a software gate and fit with a Gaussian distribution. Those data were then plotted versus position in the focal plane. Specific excitation states were then determined leading to an estimation of energy loss in MeV. In each case, the response of the Micromegas was also determined in channels by fitting the corresponding peaks.

Figure 4.17 shows the theoretically estimated (using the LISE++ software) energy loss on the Y-axis and the response of Row 2 of the new anode on the X-axis. It can be seen that the Micromegas linearity is quite good across the range.

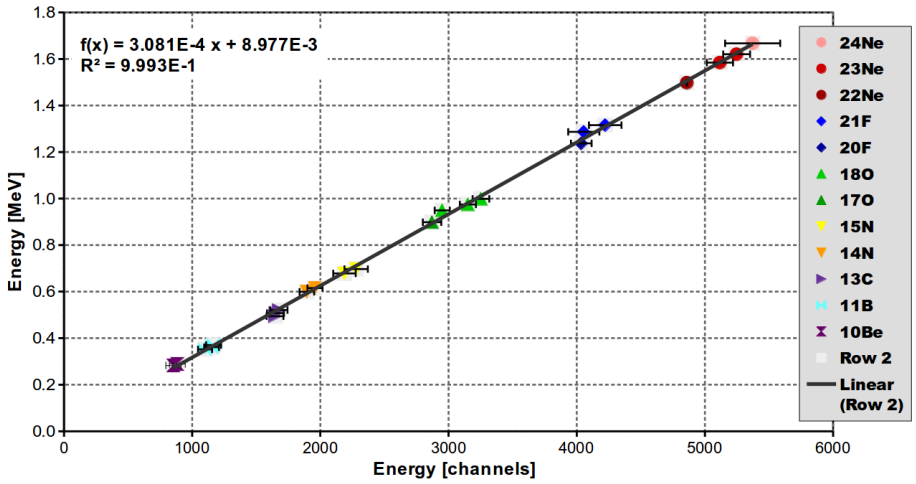

Figure 4.17: Linearity plot for the total energy loss in Row 2. The X-axis error bars indicate statistical uncertainties. The Y-axis error bars indicate the uncertainty in the LISE method of energy loss estimation.

4.2.4 *Gain variation with amplification field, pressure and particle type*

As mentioned previously, the detector gain is defined by the formula below:

$$Gain = \frac{N[\text{total electrons}]}{N[\text{ionization electrons}]} \,. \tag{4.1}$$

The average number of electrons produced in the initial ionization process is given by the ratio between the energy lost to the gas and the effective ionization potential, w, of the gas as shown in the equation:

$$N[\text{ionization electrons}] = \frac{E[eV]}{w} \,. \tag{4.2}$$

This number represents a rough estimate as it is possible that not all of the ionization energy produces ion-pairs. The effective ionization potential of isobutane is 23 eV/electron-ion pair and takes into account the fact that some pairs recombine. This means that an energy of 23 eV is required to produce one electron-ion pair. The total number of electrons collected by the anode was calculated with the formula below:

$$N[\text{total electrons}] = \frac{Q[\text{pad}]}{e} \,. \tag{4.3}$$

Here, $Q[\text{pad}]$ represents the charge induced on each pad and is estimated using the calibration shown in subsection 4.1 and the peak position in the corresponding pad histogram.

The amplification field was varied by changing the Micromegas anode bias, from 0 to V_{max}. The maximum voltage that could be applied depended on the energy loss of the ionizing particle. In all cases, the ADC range limit was reached before the gas breakdown limit. Figure 4.18 shows an example of the gain variation with amplification field. The beam was ^{27}Al and the gas pressure was 50 Torr. The four colors of data points correspond

to the 4 pads in the central column.

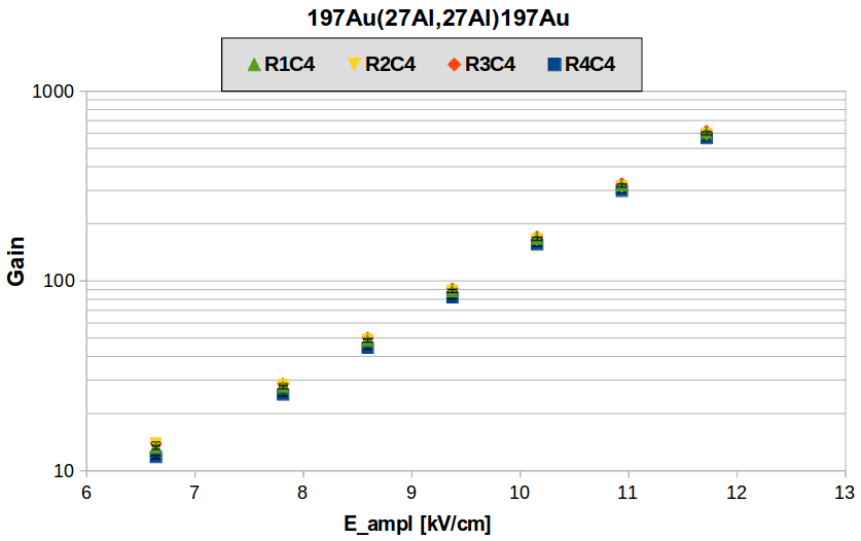

Figure 4.18: Estimated gain of the Micromegas for ^{27}Al particles and 50 Torr pressure. The Y-axis error bars indicate statistical uncertainties.

The procedure above was repeated for the different beams mentioned in the beginning of this chapter, as well as different pressures. Specifically, the collimated beam of elastically scattered ^{22}Ne particles was observed for 5 different gas pressures. Figure 4.19 shows the data curves obtained. The trend indicates an increase in gain with decreasing pressure for the same amplification field. It agrees with the expected theoretical behavior.

Data from different ionizing particles was then compiled for a comparative study of the variation of gain with Z number and amplification field. Figure 4.20 shows the curves obtained for ^{22}Ne, ^{26}Mg, ^{28}Si and ^{32}S. The gas pressure in all 4 cases was 30 Torr and the electronic gain was at minimum. All else being approximately equal, it was expected that the gain would be independent of the type of ionizing particle. Figure 4.20 shows that the experimental data confirms that. Furthermore, Figure 4.21 summarizes the total testing data regarding the Micromegas performance in terms of gain.

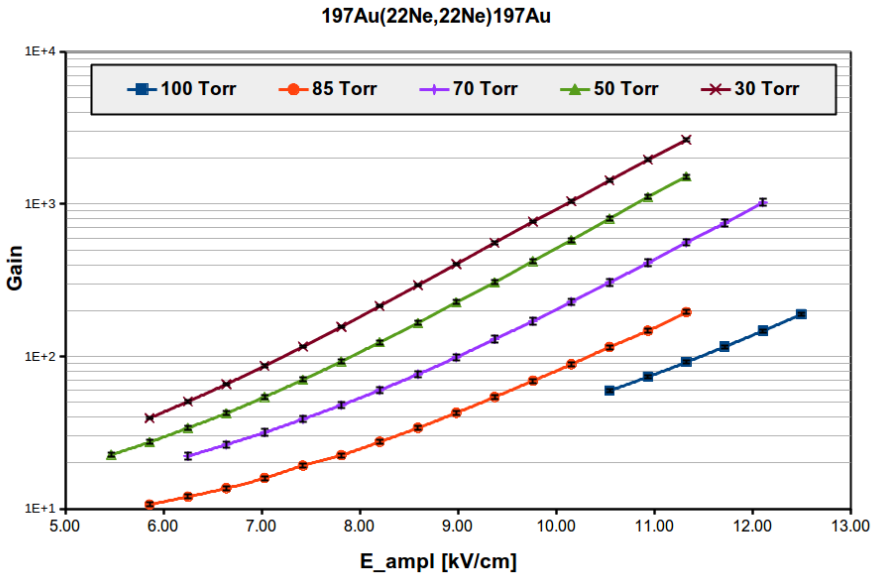

Figure 4.19: Estimated gain of the Micromegas for ^{22}Ne particles and its variation with pressure. The Y-axis error bars indicate statistical uncertainties but are too small to be visible.

While factors greater than 10^3 are desirable in other cases, for the Oxford detector and its experimental purpose, the gain results that have been obtained are very good.

4.2.5 *Energy resolution variation with gain, pressure and particle type*

The energy resolution for each pad was calculated with the formula below:

$$R_{Pad}[\%] = \frac{FWHM}{Position}\,. \tag{4.4}$$

The FWHM and position parameters were determined from fitting the energy peak in each pad with a Gaussian fit. The data used for these calculations were taken in the beam sweep procedure described above.

As an example, Figure 4.22 (a) shows the energy resolution variation with gain (or anode voltage) for the ^{27}Al beam (same data as shown in Figure 4.18). Figure 4.22 (b) shows the observed pulse amplitude for the different bias settings. Both plots exhibit the

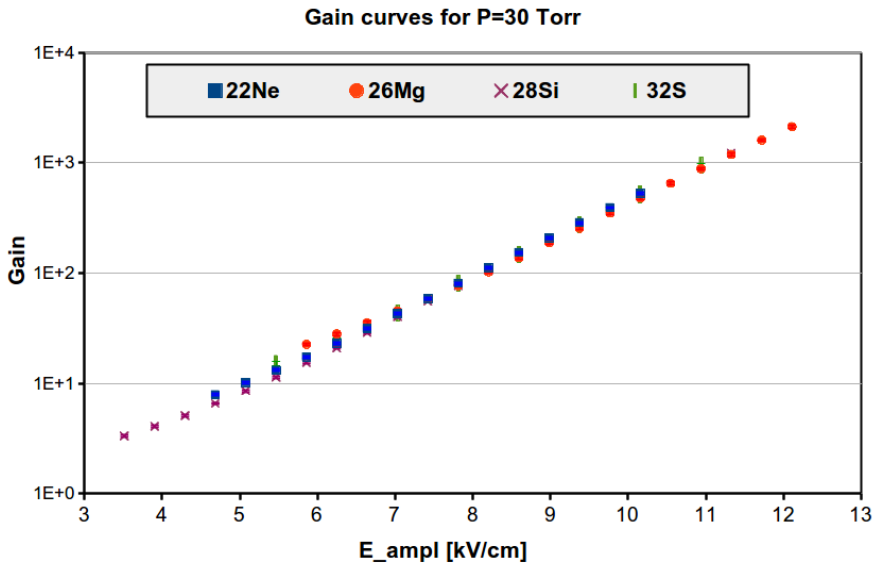

Figure 4.20: Estimated gain of the Micromegas for different ionizing particles at the same gas pressure of 30 Torr. The Y-axis error bars indicate statistical uncertainties but are too small to be visible.

threshold region between proportionality and amplification.

The data points begin at 170 V because the steps before that had signals that were below the ADC threshold. Similarly, there are no points above 300 V because those signals registered partially or totally in the overflow region. From the top plot, for this particular beam, it was decided that the best setting to run at was 280 V. For this bias voltage, Figure 4.23 shows the individual resolutions of all 28 pads.

The pads in row 1 generally have better resolution then the ones in the other rows. This is due to the fact that beam straggling is less in the gas region of that row than in the later ones. Straggling is also affected by gas pressure and Figure 4.24 shows how the resolution of pad R1-C4 varies for the case of ^{22}Ne, for 5 different pressures.

As expected, the resolution becomes worse when the pressure decreases and the energy straggling increases. For a fixed pressure of 30 Torr, but different ionizing particles, the

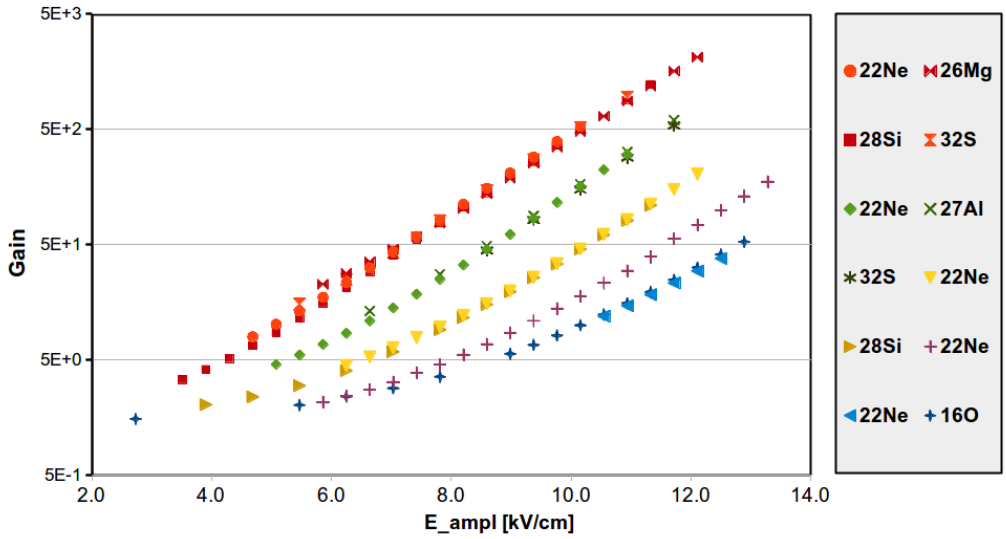

Figure 4.21: Micromegas gain curves for all the ionizing particles used in the testing. The different gas pressures are color coded (Torr): red=30, green=50, yellow=70, purple=85 and blue=100. The Y-axis error bars indicate statistical uncertainties but are too small to be visible.

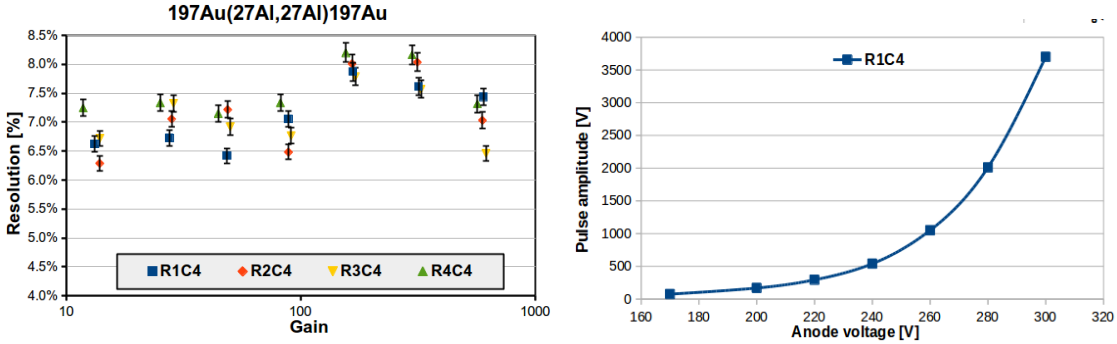

(a) (b)

Figure 4.22: (a) Resolution variation with gain for ^{27}Al at 50 Torr pressure. The Y-axis error bars indicate statistical uncertainties. (b) Shaper output amplitude for different bias voltages for pad R1-C4.

results are presented in Figure 4.25. In the left plot, the data were recorded with preamplifier gain 5 while the data in the right plot had gain 1. It can be seen that in each case, the

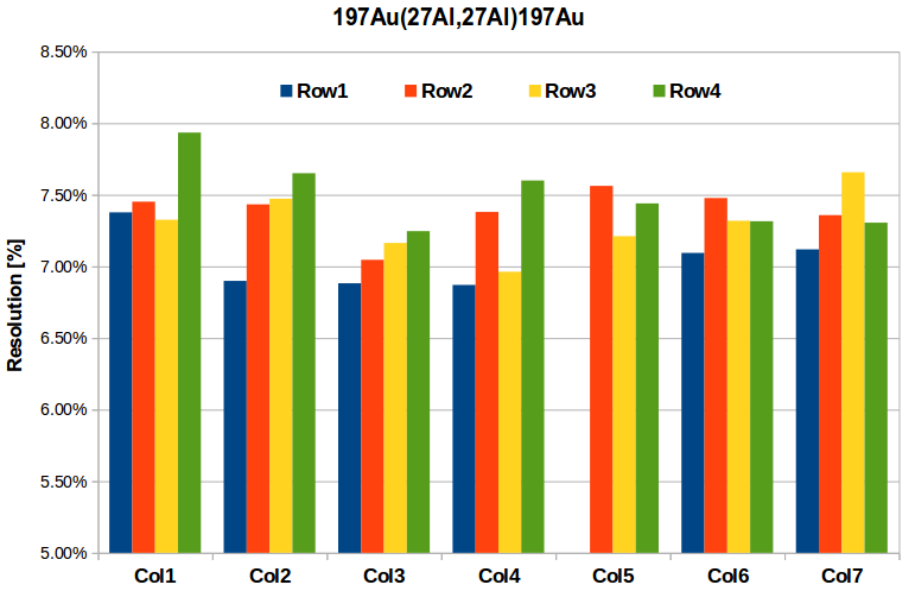

Figure 4.23: Individual pad resolutions for ^{27}Al at 50 Torr pressure.

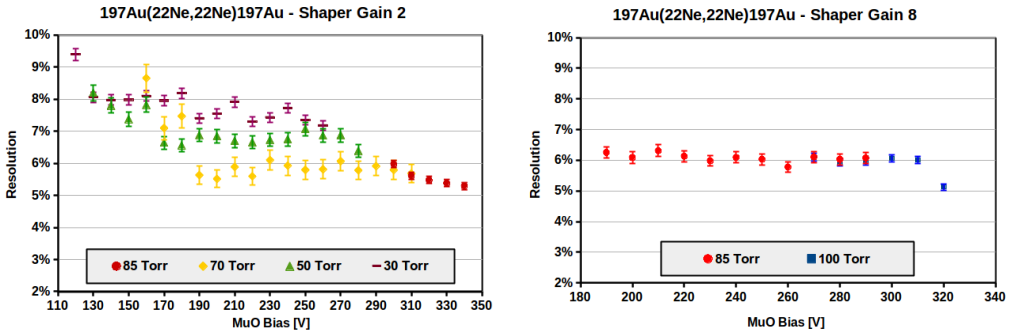

(a) (b)

Figure 4.24: Resolution variation with micromegas bias for pad R1-C4 for (a) pressures of 85, 70, 50 and 30 Torr and shaper gain 2, and (b) pressures of 100 and 85 Torr at gain 8.

resolution worsens with increasing Z.

The resolution varies only slightly with biasing voltage for ^{26}Mg and ^{32}S. However, there is a significant improvement with higher bias for ^{22}Ne than ^{28}Si. The overall range

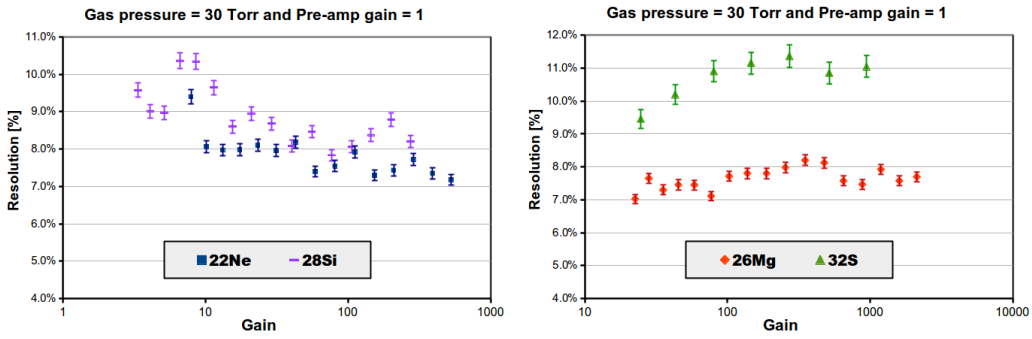

(a) (b)

Figure 4.25: Resolution variation with estimated gain for pad R1-C4 for 4 different ionizing particles, when gain is (a) 5, (b) 1.

of values is 6-11%. Compared to the dE1 resolutions of 13-20% for the original detector that are typical at this pressure, the Micromegas is definitely the better option.

4.3 Charge Sharing

When the beam is tightly collimated, it is simple to make sure that only one column of pads detects the particles. Typically, for nuclear physics experiments, the collimation mask is much wider, specifically the '4 by 1' mask described in the previous chapter. Additionally, the targets used produce a variety of reaction products. As such, the particle paths cover the entire focal plane.

For the Micromegas anode, specifically, this means that often ionization occurs in such a way that the resulting avalanche cloud is split between adjacent pads. Figure 4.26 shows an example of charge sharing, where a beam of ^{22}Ne particles was guided through the gas region between columns 3 and 4. The histogram at the bottom-left is the 3-D hitmap of the Micromegas anode showing which pads detect a signal. The histogram at the top-right shows the charge sharing pads in the first row, with R1-C3 on the Y-axis and R1-C4 on the X-axis. The remaining histograms were placed next to their respective axes to show the

individual pad responses.

In order to obtain an accurate measure of the energy loss of the ionizing particle, the amplified charge needs to be reconstructed properly from these separate individual signals. However, there are two issues that complicate the reconstruction process. The first is that, as shown in the previous subsection, the gain is not uniform across all the pads. The second problem is the danger of losing part of the signal. For example, if the charge sharing is largely uneven, it is possible that one part of the signal is so small as to register below the ADC threshold. In that case, the reconstructed signal amplitude is smaller than it should be and could lead to misinterpretation of the obtained data.

The first issue can be solved by gain-matching the pads. This procedure involves sweeping the beam across the anode as explained in the previous sections. The tightly collimated beam loses approximately the same energy in each column and can be used to relate the pads to each other in each row. Any differences in path length due to the entrance angle into the detector are small enough to be negligible.

The second issue is more difficult to resolve. The biggest obstacle is the electronic noise. In order to reduce the amount of signal lost, the system noise must be as small as possible. Unfortunately, as explained above, some of the noise contributions come from the elements in the beam-line, like the power supplies for the magnets and the vibrations caused by the vacuum cryo-pumps. It is not possible to fully isolate the detector from that.

However, if the noise can be minimized the effects of the lost data are less pronounced. Furthermore, for the purpose of particle identification the significant improvement in resolution compensates for these defects in reconstruction. This can also be helped by setting the dipole magnet such that most, if not all, the particles of interest go through a single column, thereby avoiding the issue altogether.

Taking all this into account, an example of the quality/efficiency of the reconstruction process can be seen in Figure 4.27. The top plots show the response of pads R1-C3

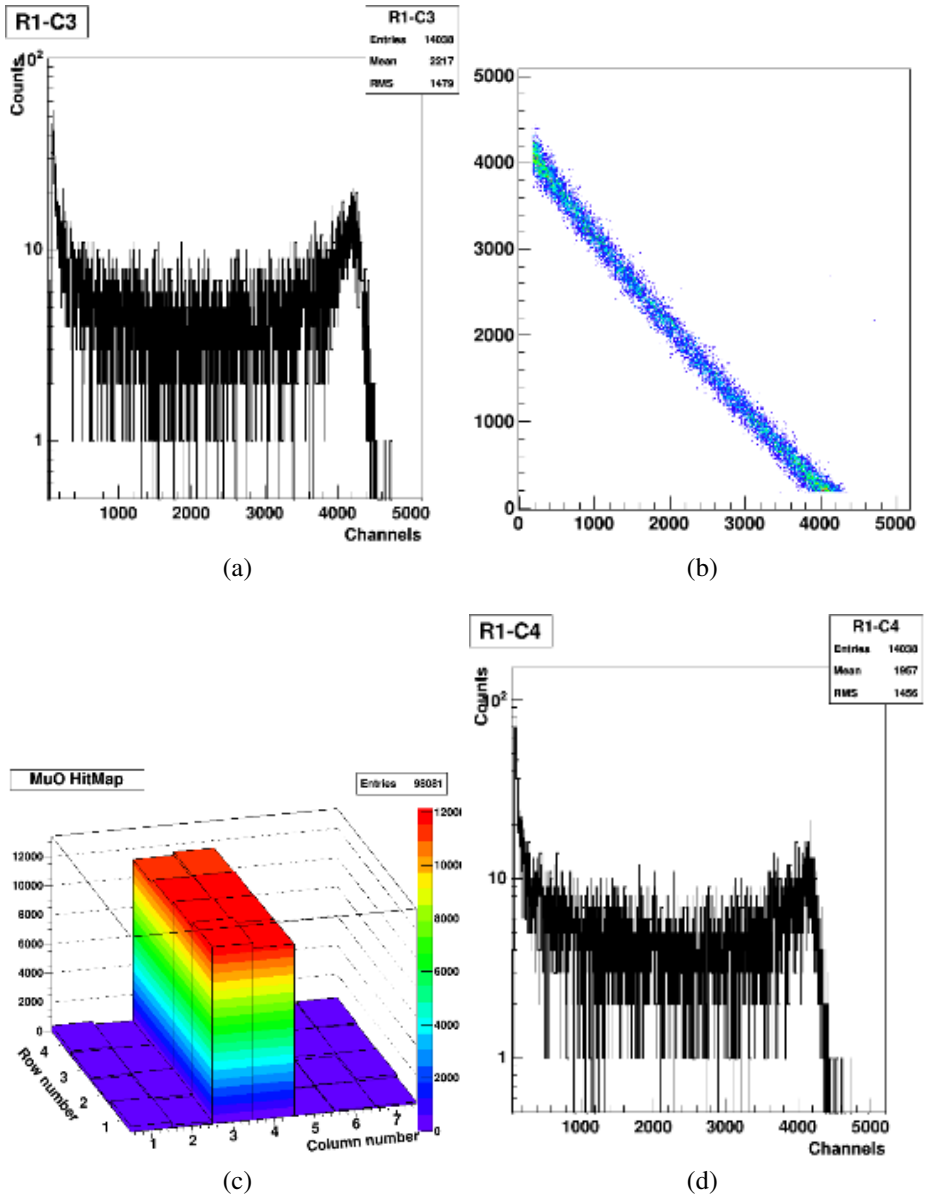

Figure 4.26: (a) Histogram showing raw data for pad R1-C3. (b) 2-D histogram showing data from R1-C3 on Y-axis and data from R1-C4 on X-axis. (c) 3-D hitmap showing the path of the beam. (d) Histogram showing raw data for pad R1-C4.

(resolution $\approx$ 6.2%) and R1-C4 (resolution $\approx$ 6.4%), when there is no charge sharing.

The bottom-left histogram shows the reconstructed peak when the beam passes between the two pads. As expected, the energy resolution is slightly worse, at 6.9%, and the

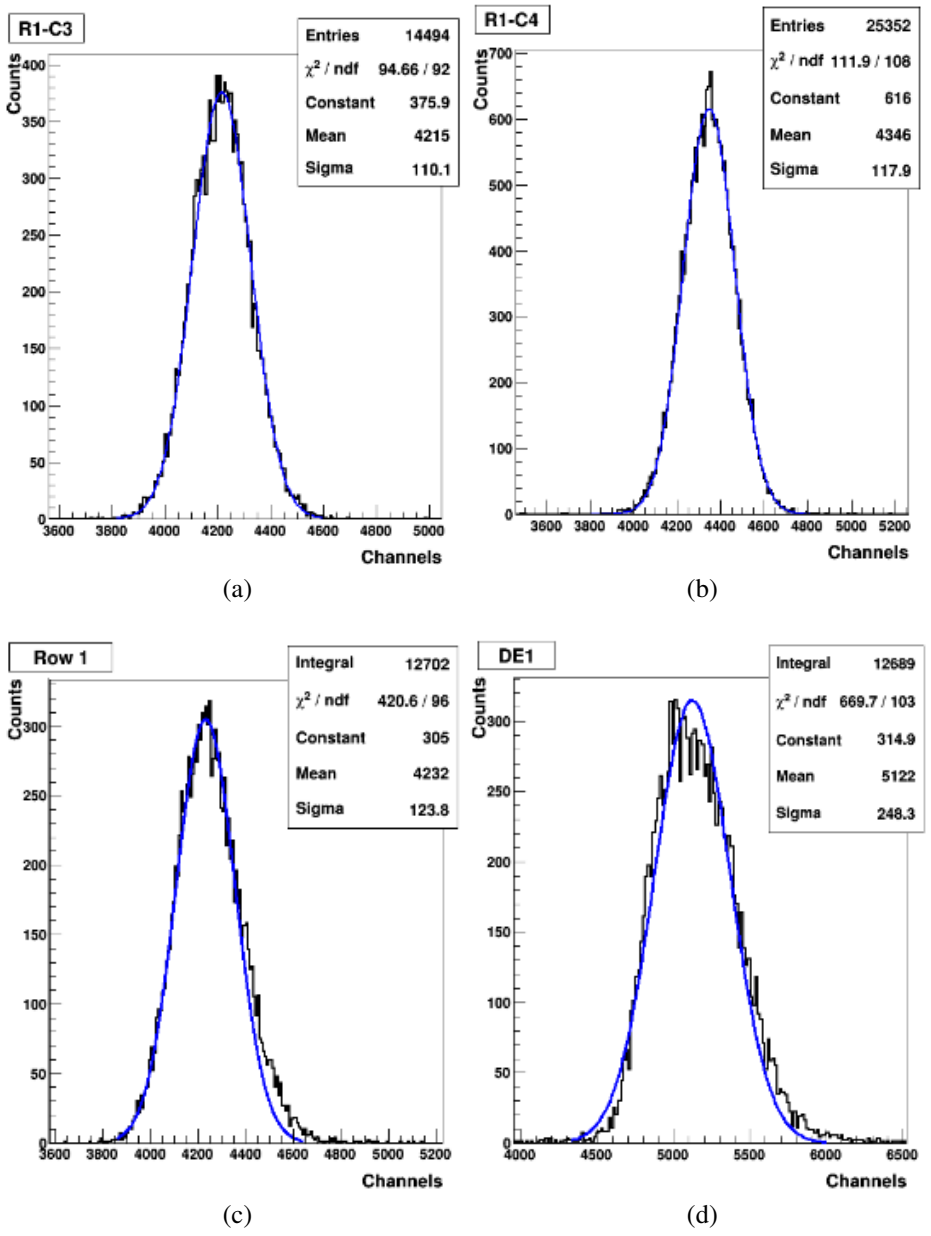

Figure 4.27: (a,b) Energy histograms for pads R1-C3 and R1-C4. (c) Histogram showing the reconstructed energy. (d) Histogram showing energy loss in the ionization chamber.

peak exhibits a small tail on the high energy side. The bottom-right histogram shows the ionization chamber response which is similar in shape but the resolution is significantly

worse, at 11.4%. The number of counts under these two peaks differs by less than 0.1%. As such, the reconstruction method was considered successful and was used throughout the analysis.

4.4 Calculating the Total Anode Energy

The first step in obtaining the total Micromegas anode energy is to gain-match the pads as explained above. The second step is to determine the multiplicity of an event for each row. Since a particle can either 'hit' one pad or 'hit' between two neighboring pads, the multiplicity per row should only be 1 or 2. All other events are excluded.

Under these circumstances, the energy detected by each row is determined from the sum of the individual, gain-matched, responses of the pads in each row. The final step in obtaining the total energy is to calculate the average of the 4 rows. During the course of testing, several different methods were tried for 'summing' the 4 row energies. The first was a standard sum which didn't produce any improvement over the single pad resolution. Averaging was attempted next, starting with an arithmetic mean, followed by a weighted arithmetic mean and lastly a geometric mean.

An example of such a comparative analysis can be found in Table 4.2 for some of the scattered beams used, specifically those that were tested at an assumed pressure of 30 Torr. The various notations are defined below:

$$\text{SumR} = E_{R1} + E_{R2} + E_{R3} + E_{R4} \tag{4.5}$$

$$\text{AvgR} = \frac{E_{R1} + E_{R2} + E_{R3} + E_{R4}}{4} \tag{4.6}$$

$$\text{WAvg} = \frac{w_1 E_{R1} + w_2 E_{R2} + w_3 E_{R3} + w_4 E_{R4}}{w_1 + w_2 + w_3 + w_4} \tag{4.7}$$

$$\text{EMuO} = \sqrt[4]{E_{R1} \cdot E_{R2} \cdot E_{R3} \cdot E_{R4}} \tag{4.8}$$

$$\text{dEtot} = dE1 + EMuO\,. \tag{4.9}$$

Beam	R[dE1]	R[Row]	R[SumR]	R[AvgR]	R[WAvg]	R[EMuO]	R[dEtot]
^{22}Ne	12.2%	7.4%	5.0%	5.1%	5.2%	4.7%	6.1%
^{26}Mg	7.5%	7.7%	5.1%	5.0%	4.9%	4.4%	4.3%
^{28}Si	7.9%	8.8%	6.5%	6.4%	6.4%	6.1%	4.6%
^{32}S	14.9%	11.0%	7.2%	7.2%	7.1%	6.9%	7.0%

Table 4.2: Energy loss resolutions for different combinations of the detection elements and for the different test beams used.

It can be seen that the weighted arithmetic and geometric means give similar results, best among the 4 'summation' methods. In the end, the geometric average was chosen over the other, because it shortened the analysis time by bypassing the need to determine the 'weight' of each row energy.

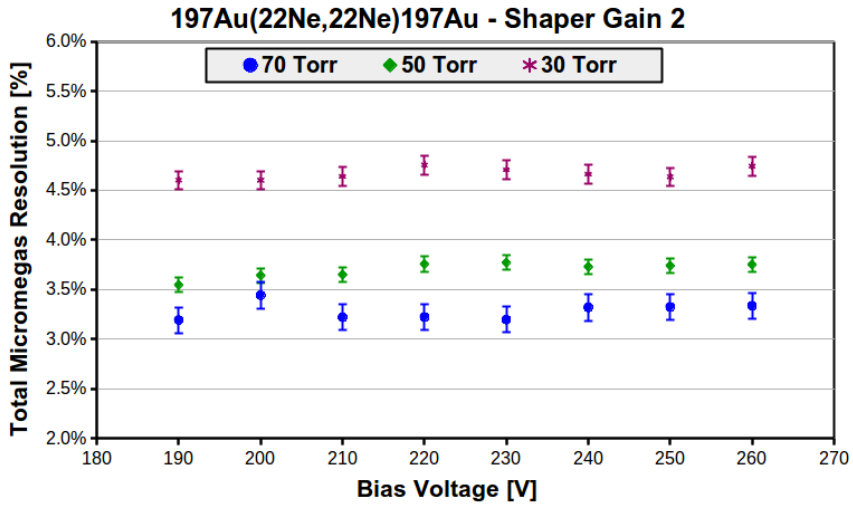

Figure 4.28: Total energy resolution for different bias voltages and 3 different pressures (colors labeled in the legend).

It can also be seen from the table that being able to multi-sample the energy in this way allows for significant improvements in the energy resolution. Figure 4.28 shows the total

Micromegas energy (called henceforth EMuO) resolution for different bias voltages and pressures. Comparing these with the numbers in Figure 4.23 shows that the improvement in resolution by a factor of $\sim$2 due to multi-sampling affects a wide range of bias voltages. This in turn means that the choice of bias doesn't affect the total anode energy as much as much as it does, individual pads, therefore allowing a larger optimal operational range for the Micromegas.

Moreover, as shown with the last column in Table 4.2, adding the Micromegas energy with the dE1 energy results in another significant improvement in the overall energy loss resolution of the Oxford detector.

5. ASTROPHYSICAL DATA ANALYSIS AND RESULTS

In order to determine the rate of occurrence of a reaction, we need to know the cross-section of that reaction. This was defined in Chapter 2, Eq. 2.17, as the ratio between the outgoing flux and the incoming flux. In particular, in an experiment it is useful to determine the differential cross-section for outgoing angles. For an incident beam of particles impacting a target, the cross-section can be calculated with the following formula:

$$\frac{d\sigma}{d\Omega}(\theta) = \frac{Y(\theta)}{N_{\text{beam}} \cdot N_{\text{target}} \cdot \Delta\Omega(\theta)} \,. \tag{5.1}$$

$Y(\theta)$ is called the yield and it represents the number of outgoing particles detected at angle $\theta \pm \Delta\theta/2$. In this study, $\Delta\theta$ was chosen as 0.25° for smaller reaction angles, where counting statistics were high. At larger angles, $\Delta\theta$ was chosen as 0.5°or even 1°(if counting statistics were particularly low). N_{beam} refers to the number of incident particles and is determined from the total beam charge (which is calculated with Eq.3.3).

$$N_{\text{beam}} = \frac{Q_{\text{beam}}}{Ze} = \frac{I_{\text{beam}} * FC_{\text{corr}}}{Ze} \,, \tag{5.2}$$

where FC_{corr} represents the number of counts measured by the Faraday Cup after calibration (see section 3.2.5) and dead time corrections. Similarly, N_{target} represents the number of atoms per area in the target. Since the differential cross-section is generally expressed in millibarns per steradian (1 mb/sr = 10^{-27} cm^2), N_{target} is expressed with the formula:

$$N_{\text{target}} = \frac{\text{Thickness}[mg/cm^2]}{A_{\text{target}} \cdot \text{a.m.u}[mg]} \,. \tag{5.3}$$

Here, A_{target} is the target mass number and a.m.u is the atomic mass unit. The last

Target	^{13}C	^{27}Al (#1)	^{27}Al (#2)	^{27}Al (#3)	^{197}Au
Thickness [$\mu g/cm^2$]	91.8	88.3	247.0	979.8	200.1
Absolute error [$\mu g/cm^2$]	6.9	6.8	13.8	52.9	16.6
Percentage error	7.5%	7.7%	5.6%	5.4%	8.3%

Table 5.1: Adopted thicknesses of the targets used for the experiments in this study.

element in the denominator of Eq. 5.1, $\Delta\Omega(\theta)$, refers to the solid angle containing the particles counted in $Y(\theta)$. Data for the cross-section angular distribution was taken with the 'wide' or '4-by-1' mask. This aperture subtends a solid angle of 1.25 msr, but was later divided by 16, 8 or 4 according the choice of $\Delta\theta$ explained above. Taking all this into account, the final formula that was used in the determination of the differential cross-section was:

$$\frac{d\sigma}{d\Omega}(\theta)\left[\frac{mb}{sr}\right] = \frac{Y(\theta)[cts]}{3.76 \cdot I_{\text{beam}}[pC] \cdot \frac{FC_{\text{corr}}}{Z} \cdot \left(\frac{T[mg/cm^2]}{A_T}\right) \cdot \Delta\Omega(\theta)[sr]} \,. \tag{5.4}$$

The thickness of each target used was determined either on-line (with beam), off-line (with alpha source) or both, using the procedures described in the previous chapter (Section 3.2.6). The values obtained are shown in Table 3.7. The values adopted throughout the following analysis are presented in the table below along with the corresponding absolute and percentage uncertainties.

5.1 The ^{27}Al(^{13}C, ^{12}C)^{28}Al Experiment

The reaction was measured in 2 experiments. A beam of ^{13}C was accelerated to E_{Lab} $\approx$ 11.8 MeV/A and impinged on a target of ^{27}Al. Targets of three thicknesses were used, as presented in Table 5.1. The increase in thickness was intended to help with the low statistics expected at larger reaction angles. A target of ^{197}Au was also used, but only for calibration purposes following the procedures outlined in sections 3.2.3 and 3.2.5 for po-

sition calibration and FC normalization. The results of the position and angle calibrations can be seen in Figure 5.1. On the left, (a), is a histogram of the reconstructed focal plane showing the elastic scattering peak in the center where it was expected to be. On the right, (b), is a histogram of the target angle showing the 5 fingers corresponding to the slits in the 5-finger mask.

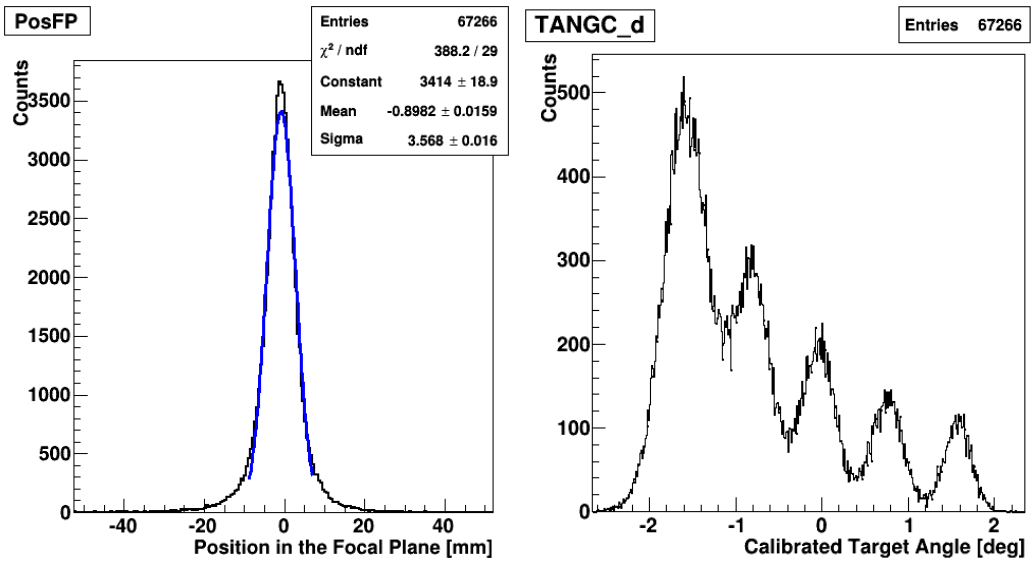

(a) (b)

Figure 5.1: Spectra showing calibration data from the scattering of the ^{13}C beam on ^{197}Au at 6° lab. (a) Histogram of the reconstructed focal plane. (b) Histogram of the target angle showing the 5 fingers corresponding to the slits in the 5-finger mask.

The resolution of the position peak was ∼7 mm (equivalent to ∼600 keV) and the resolution in angle was 0.35°-0.65° over the measured angular range. The FC normalization factor was obtained with the procedure from section 3.2.5, using the data in Figure 5.1, (b), and found to be ≈0.8. Figure 5.2 shows the calculated and experimental Rutherford cross-sections obtained at 6°, as well as the renormalized data to account for the FC correction.

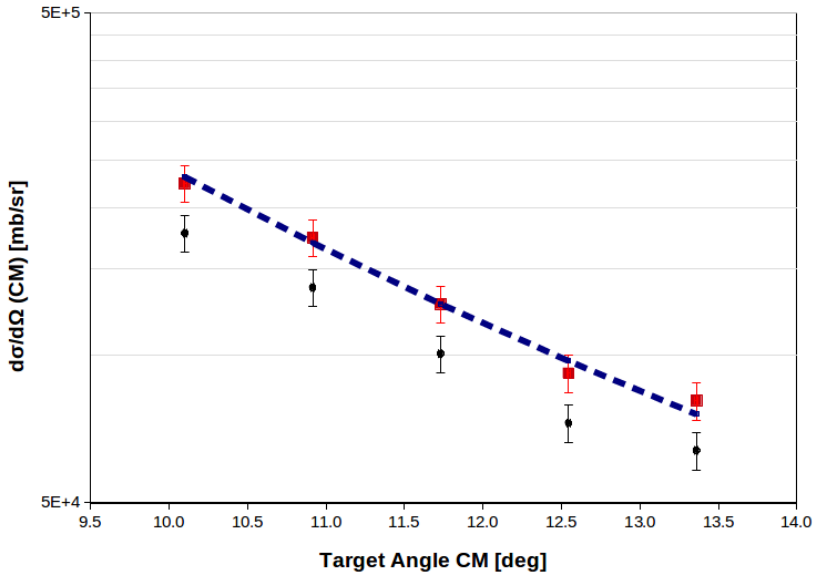

Figure 5.2: Comparison between scattering data and Rutherford calculations for ^{13}C on ^{197}Au. Black dots represent cross-section estimations with a 1.0 normalization factor. The blue line shows the Rutherford curve. Red squares show the data renormalized to fit the curve. The X-axis error bars in the experimental data are given by the detector angular resolution multiplied by the statistical percentage error. The Y-axis error bars indicate the uncertainty in the experimental cross-section which is dominated by the target thickness error.

The resolutions for energy loss in the gas and stopping energy were extracted from the same data. For the ionization chamber, dE1, the resolution was $\approx$ 10.8%. For the avalanche counters, only wires 1 and 4 were included in the calculation of the total wire energy, TwireE, and its resolution was found to be $\approx$ 12%. For the residual energy, PM, the resolution was $\approx$ 13.5%. The total energy loss, dEtot, was calculated as well by summing arithmetically dE1 and TWireE and its resolution was found to be $\approx$ 8%.

5.1.1 *The elastic scattering data*

The data for the elastic cross-section distribution were obtained over an angular range of 4°-38° in the laboratory system, equivalent to 6°-54° in center of mass. Up to an angle of 20° lab, there was an overlap of 1 or 2° between each two consecutive MDM angles to ensure consistency. At larger angles, it was not possible to have this check due to time constraints and reduced cross-sections. The data analysis consisted of three major steps that were followed for each MDM angle.

The first step was the PID, i.e. isolating the data representing only elastic and inelastic scattering on ^{27}Al. This involved 2 analysis gates placed as shown in Figure 5.3. Specifically, the first gate was placed in the dEtot–PM histogram shown on the left (Figure 5.3, (a)) around the Z=6 line, corresponding to C isotopes. The second gate was placed in the PosFP–dEtot histogram shown on the right (Figure 5.3, (b)) around the ^{13}C events.

In order to make sure that the identification was correct, RAYTRACE was used to estimate the expected position of the elastic scattering peak in the focal plane, as well as possible inelastic states. For the MDM at 6°, the position of the ground state of ^{13}C was at $\approx$15 mm. Figures 5.4, (a) and (b) agree with this prediction. In Figure 5.4, (a) this state shows as a horizontal band of high statistics. In Figure 5.4, (b) one can see the expected Gaussian peak in the focal plane spectrum. Figure 5.4, (c) shows calibrated target angle information. All three plots display only the data included in the two gates described above. Given the low statistics for inelastic contributions, Figure 5.4, (c) can be considered a rough preview of the cross-section distribution for this angular region, showing a clear dip in the distribution.

Having separated the events of interest from the rest, the second step in the analysis was to put angular gates (or conditions) of specific width on the target angle. This was similar to drawing vertical lines in Figure 5.4, (c) to further separate the data, only in

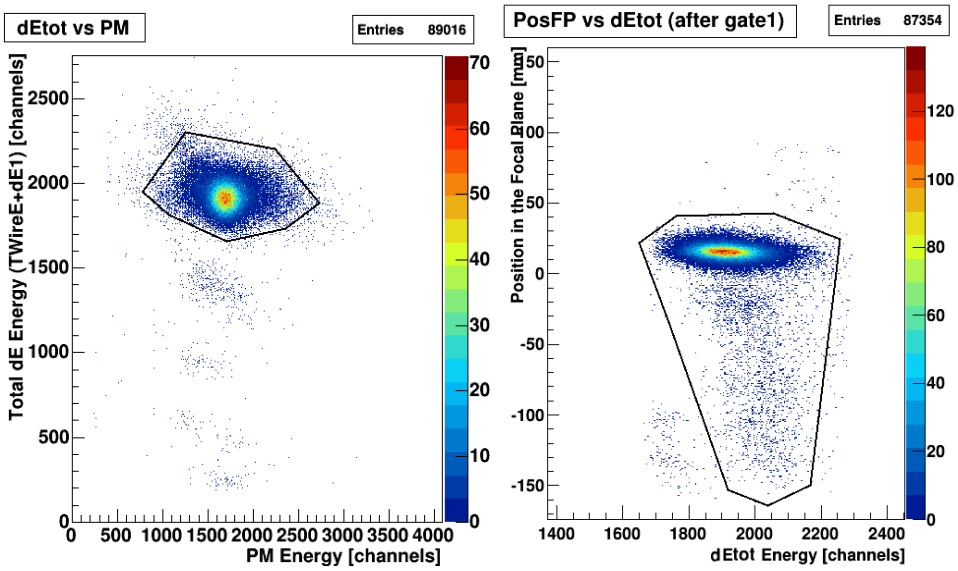

(a) (b)

Figure 5.3: 2-D particle identification spectra for ^{27}Al(^{13}C,^{13}C)^{27}Al at 4°-8° in the lab frame. (a) Ungated data plotted in a dEtot versus PM energy histogram showing the first gate that is to be placed for analysis. (b) Data from the gate in spectrum (a) plotted in a Position versus dEtot histogram showing the second gate that is to be used for analysis.

angular bins now. The chosen bin width was 0.5° and the data in each bin were plotted by position in the focal plane. The final step in extracting the cross-section distribution was to determine the number of events in the elastic peak present in each angular bin spectrum.

The full results can be seen in Figure 5.5, which shows the angular distribution of the differential cross-section, color-coded by MDM angle. Some of the points corresponding to the edges of the 4° angular opening had to be excluded due to underestimation or overestimation of the number of elastic events. In general, where there was overlap between MDM angles, the cross-section was averaged. Figure 5.6 shows the final experimental angular distribution for the elastic scattering data.

The uncertainties of the cross-section distribution points shown in Figures 5.5 and 5.6 were given by: statistical uncertainties (0.6%-20%), the target thickness uncertainty

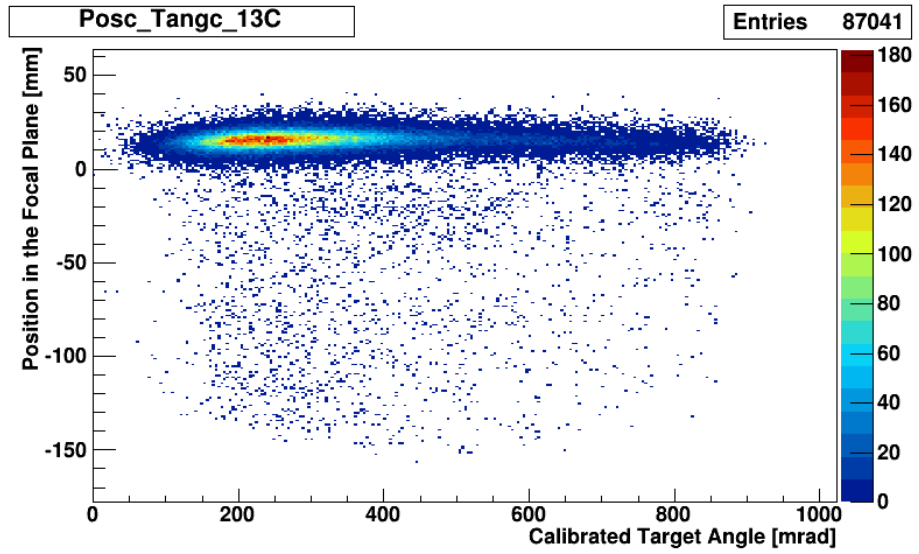

(a)

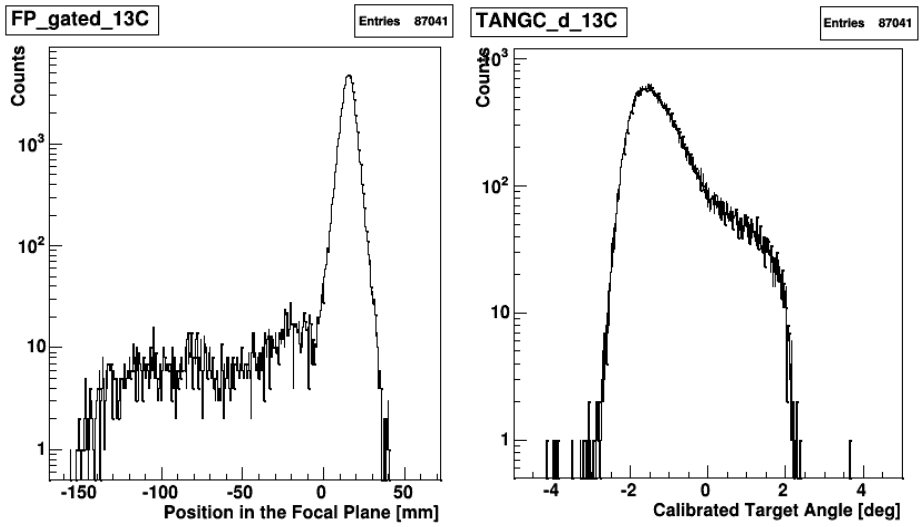

(b) (c)

Figure 5.4: Gated spectra for ^{27}Al(^{13}C,^{13}C)^{27}Al at 4°-8° in the lab frame. (a) 2-D histogram showing data by position in the focal plane versus calibrated target angle. (b) 1-D spectrum showing the position of elastic and inelastic events in the focal plane. (c) 1-D spectrum showing the calibrated target angle of elastic and inelastic events.

(7.7%), the FC normalization error (1.3%) and the uncertainty in the estimation of inelastic and impurities contamination (4%).

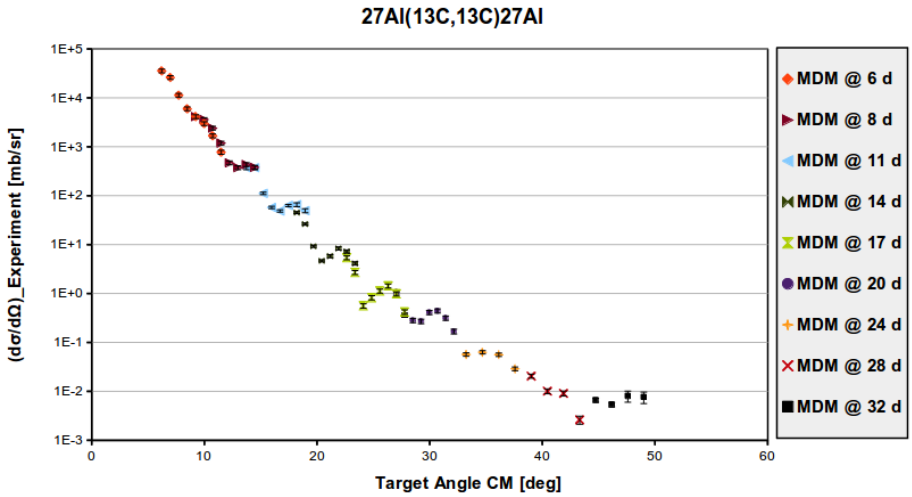

Figure 5.5: Experimental angular distribution for the elastic cross-section. The MDM angles are denoted by different colors as indicated in the chart legend. The X-axis error bars are given by the detector angular resolution multiplied by the statistical percentage error. The Y-axis error bars are explained in the text.

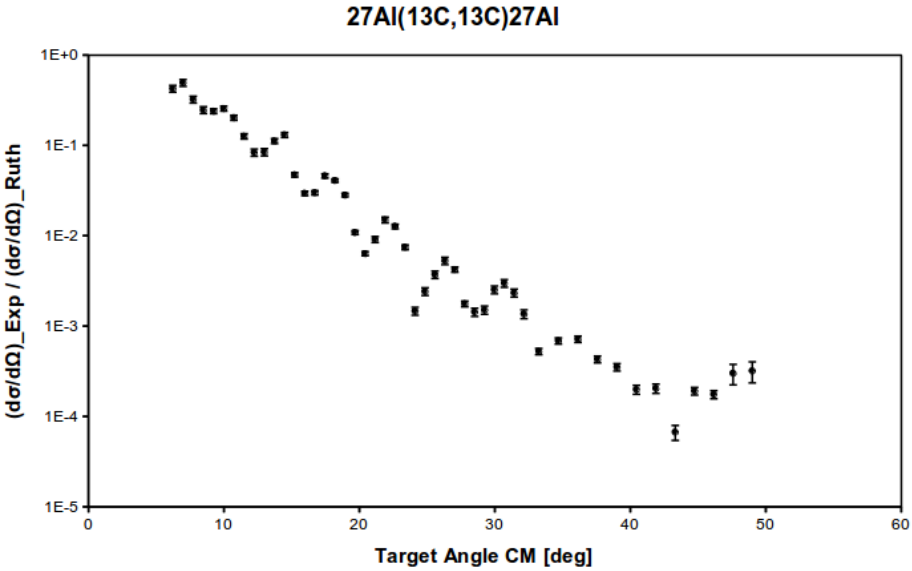

Figure 5.6: Experimental angular distribution for the elastic cross-section of ^{13}C on ^{27}Al target. Cross-section values are C.M. and normalized to the Rutherford cross-section. Error bars are included and explained in the text. The X-axis error bars are given by the detector angular resolution multiplied by the statistical percentage error. The Y-axis error bars are explained in the text.

5.1.2 *The optical model parameters*

The elastic channel of the ^{13}C+^{27}Al reaction was measured in order to determine the corresponding optical model parameters. In order to find these parameters, the data shown in Figure 5.6 was fitted with a Wood-Saxon form, a squared WS form as well as with 2 of the double-folding shapes described in section 2.3. The Wood-Saxon fit was performed using the codes OPTIMINIX [56] and PTOLEMY [57]. The code FRESCO [58] was also used as an extra check. The quality of each fit was determined by χ^2 as defined below:

$$\chi^2 = \frac{1}{N-f}\sum_i \frac{(\sigma_{\text{exp}}(\theta_i) - \sigma_{\text{fit}}(\theta_i))^2}{(\Delta\sigma_{\text{exp}}(\theta_i))^2}\,, \tag{5.5}$$

where N is the number of points involved in the calculation (N = 48), f is the number of free parameters and $\Delta\sigma_{\text{exp}}(\theta_i)$ represents the individual uncertainties estimated as described in the previous subsection. The lowest χ^2 dictated the best fits. The first step in the fitting process was to perform a grid search for the real potential, V. Both codes have the option to read in the experimental data in center of mass (angle, cross-section) pairs and the corresponding uncertainties. The codes then find the closest matching distribution by varying the parameters chosen by the user.

During the grid search, V was varied from 2 MeV to 300 MeV in steps of 2 MeV. The fitting code was ran for each step, with the real depth fixed, while the other 5 parameters were varied to obtain the lowest χ^2 possible under these condition. The Coulomb contribution was accounted for using an uniform charge distribution as shown in Eq. 2.49, with r_C = 1.0 fm. Figure 5.7 shows the results of the grid searches for the WS model (in (a)) and for the WS^2 model (in (b)), zoomed around the unique minima that were found in each case and showing an unusual lack of the typical ambiguities associated with optical model analysis. For those values, the fitting code was run again but with all 6 parameters free. The two OMP sets are presented in Table 5.2.

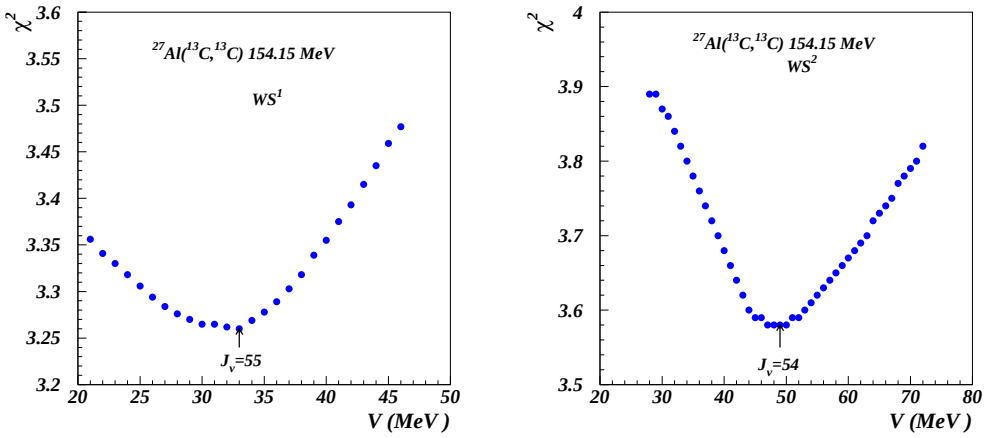

(a) (b)

Figure 5.7: Plots showing the grid searches done for the strength of the real component of the (a) Woods-Saxon optical potential model and (b) Woods-Saxon^2 optical potential model.

It can be seen that the parameters for the two models are roughly similar, with weak real and imaginary potentials. The range and diffuseness parameters are slightly more different but the relationship between each pair is consistent for both parameter sets, $r_V < r_W$ and $a_V > a_W$. Also included in the table and calculated by the fitting code are the root mean square radii of the real and imaginary potentials, R_V and R_W, as well as the respective volume integrals per nucleon pair, J_V and J_W, which were calculated with the formula below. J_W has the same value for the two parameter sets, indicating that the absorption component does not depend on the characteristics of the real part of the OMP.

$$J = J_V + iJ_W = -\frac{4\pi}{A_p A_t}\int_0^\infty (V(r) + iW(r))r^2 dr\,. \tag{5.6}$$

The two Woods-Saxon type fits are shown in Figure 5.8 along with the experimental

OMP Type	V [MeV]	W [MeV]	r_V [fm]	r_W [fm]	a_V [fm]	a_W [fm]	χ^2	σ_R [mb]	J_V [MeV fm^3]	R_V [fm]	J_W [MeV fm^3]	R_W [fm]
WS	33.	8.48	0.8287	1.1401	1.0832	0.4421	3.26	1217.	55.	5.2915	24.	5.0034
WS^2	49.	9.09	0.9221	1.2103	1.7588	0.5888	3.58	1162.	54.	5.1021	24.	4.8767

Table 5.2: The Woods-Saxon OMP parameters obtained from fitting the elastic scattering cross-section distribution of the reaction ^{27}Al(^{13}C,^{13}C)^{27}Al. In both cases, the Coulomb radius was fixed at r_C = 1.0 fm.

OMP Type	N_V	N_W	t_V [fm]	t_W [fm]	χ^2	σ_R [mb]	J_V [MeV fm^3]	R_V [fm]	J_W [MeV fm^3]	R_W [fm]
JLM1	0.1180	0.2827	0.8516	1.1800	7.17	957.	62.97	4.982	32.06	3.791
JLM1	0.2020	0.5954	0.6636	1.0668	8.66	1340.	106.53	6.377	67.07	4.187
JLM3	0.1280	0.3761	0.8461	1.1984	7.64	966.	63.06	4.966	36.32	3.723
JLM3	0.2220	0.7568	0.6558	1.0817	8.73	1346.	108.05	6.391	72.57	4.119

Table 5.3: The Double-Folding OMP parameters obtained from fitting the elastic scattering cross-section distribution of the reaction ^{27}Al(^{13}C,^{13}C)^{27}Al, with two of the double-folding shapes: JLM1 and JLM3.

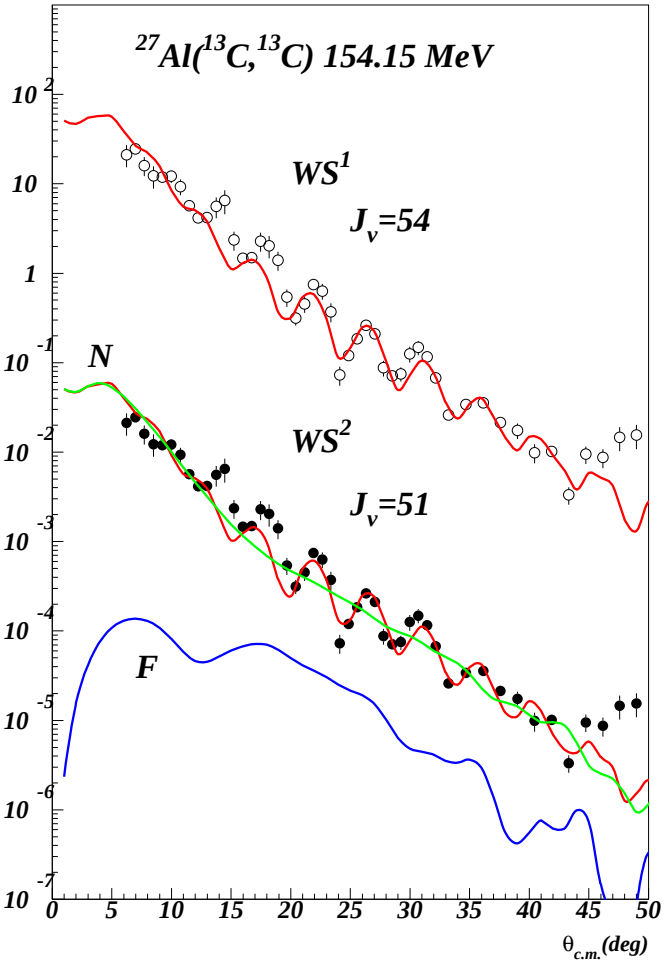

Figure 5.8: Plot showing the experimental cross-section angular distribution of reaction $^{27}Al(^{13}C,^{13}C)^{27}Al$ normalized to the Rutherford cross-section fitted with the optical model potentials (a) WS and (b) WS^2. The empty (full) circles indicate the experimental data multiplied (divided) by a factor of 50 for easier comparison. The red lines denote the OMP fits. Near and Far components are also indicated, in green and blue, respectively.

data for comparison. It can be seen that the fits seem to describe the general shape of the cross-section distribution well. However, there are sections where the discrepancies between theory and experiment do not fall within the uncertainty range. The cause of this is difficult to determine. Part of it could be attributed to normalization errors, like mis-

determined beam charge or incorrect target thickness. However, that is not likely the case as some data points that are in disagreement with the fits were determined under the same conditions (target and beam normalization) as points that do agree with the models.

Another potential cause could be the inaccurate estimation of inelastic contributions from the first ($1/2^+$, 843.8 keV) and second ($3/2^+$, 1014.6 keV) excited states in ^{27}Al and/or scattering off impurities. In particular, it should be noted that scattering off elements with a smaller Z than aluminum (like carbon or oxygen) would be basically impossible to account for. This is because the corresponding band would be tilted downwards in a histogram like Figure 5.4, (a), and as such easy to mistake for inelastic contribution. From Figure 5.8, it can be seen that some of the more significant discrepancies occur at forward angles, where the scattering off impurities is also more likely to happen. In addition to that, there is a slight shift in angle between the model and the experimental data. Both could be consequences of inaccurate estimations.

Last, but not least, it is possible that the optical model is failing to correctly describe the physics of the elastic interaction between ^{13}C and ^{27}Al. To test that, the experimental distribution was also fitted with double-folding models, specifically JLM1 and JLM3. The DF grid searches showed a similar lack of ambiguous solutions to the WS. Each search produced only a pair of potential solutions and the corresponding fitting parameters are presented in Table 5.3. It can be seen from the χ^2 values that the double-folding models are even less successful than the WS ones in describing the cross-section distribution.

Figure 5.9 shows the DF fits along with the experimental distribution. The normalization factor and range for the real part of the potential in each case are roughly close to the standard values mentioned in Ref. [39]. However, the imaginary renormalization factor and range are significantly lower, suggesting that the DF models might not be calculating correctly the imaginary component of the effective interaction and its density dependence.

All the fitting plots include a decomposition of each fit into near-side and far-side

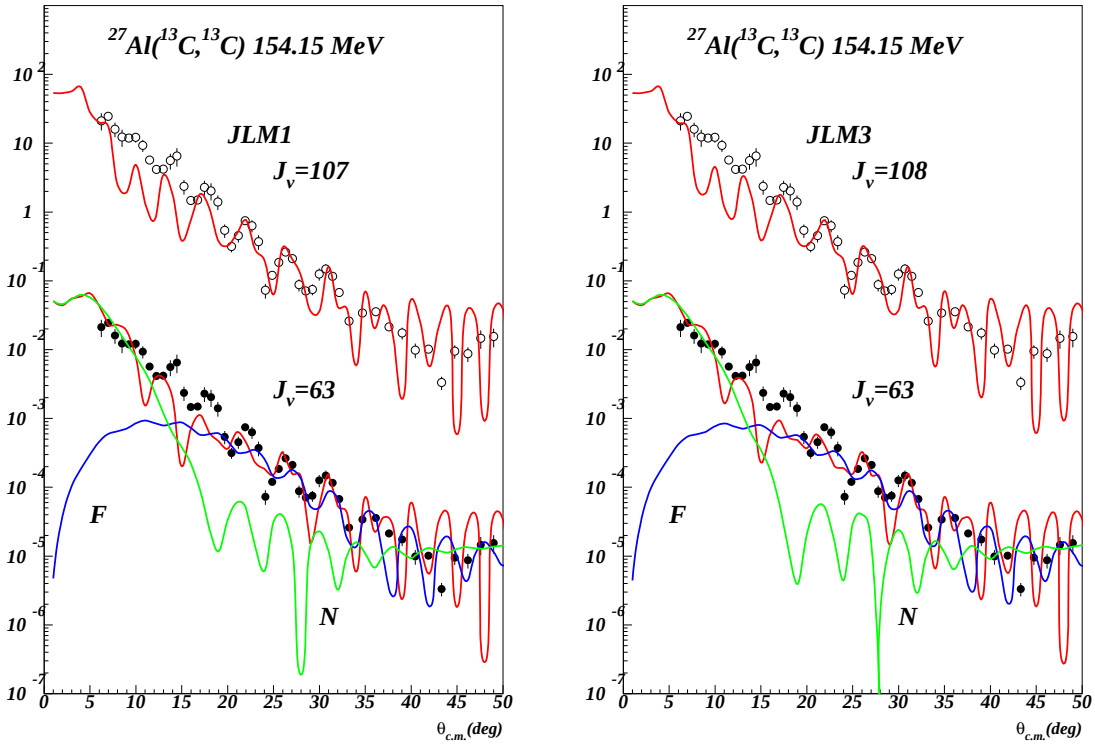

(a) (b)

Figure 5.9: Plot showing the experimental cross-section angular distribution of reaction ^{27}Al(^{13}C,^{13}C)^{27}Al normalized to the Rutherford cross-section fitted with the double folding potentials (a) JLM1 and (b) JLM3. The empty (full) circles indicate the experimental data multiplied (divided) by a factor of 50 for easier comparison. The red lines denote the OMP fits. Near and Far components are also indicated, in green and blue, respectively.

components of the angular distribution using:

$$f(\theta) = f^{+}(\theta) + f^{-}(\theta)\,, \tag{5.7}$$

with $f^{-}(\theta) = f^{+}(-\theta)$. $f^{-}(\theta)$ indicates the near-side component and $f^{+}(\theta)$ the far-side component. The WS fits shown in Figures 5.8 present a very weak far-side component indicating that the reaction is indeed peripheral.

5.1.3 *The neutron transfer data and the ANC determination*

In addition to the elastic channel, data were also taken for the neutron transfer from ^{13}C to ^{27}Al. However the statistics were very limited and only a small number of data points were obtained. The overall angular range measured was 6°-36° in the C.M. system. The analysis procedure was similar to the one used for the elastic data, with the exception of the angular bin widths. Given the low statistics at larger angles, 2° and 4° bins were used.

Figure 5.10 shows an example of the particle identification procedure done for the data taken at 6° in the lab. The histogram in (a) shows the dEtot–PM 2D spectrum with the first gate placed around the Z=6 line, corresponding to C isotopes. The data in this gate are shown in the PosFP–dEtot histogram on the right (Figure 5.10, (b)) with a second gate around the ^{12}C events.

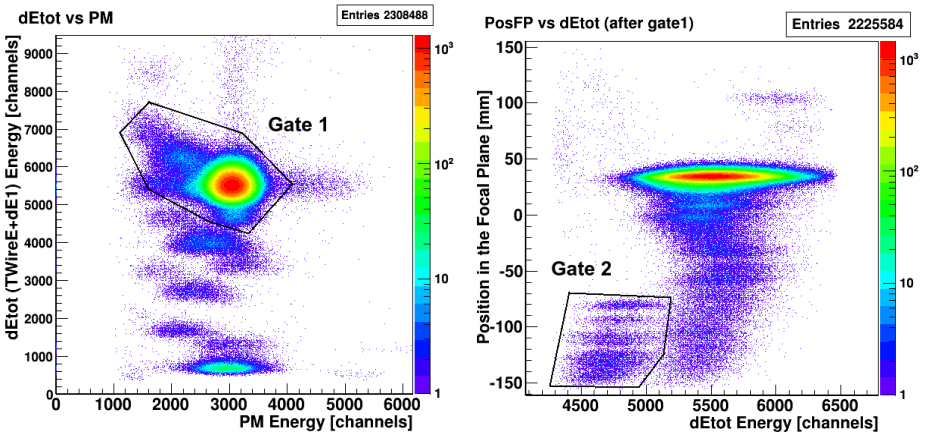

(a) (b)

Figure 5.10: 2-D particle identification spectra for ^{27}Al(^{13}C,^{12}C)^{28}Al at 4°-8° in the lab frame. (a) Ungated data plotted in a dEtot versus PM energy histogram showing the first gate that is to be placed around the C isotopes. (b) Data from the gate in spectrum (a) plotted in a Position versus dEtot histogram showing the second gate that is placed around the ^{12}C particles for the analysis of the transfer channel.

The data inside the two gates can be seen in Figure 5.11 plotted in a focal plane position histogram with the various peaks identified. It can be seen that the position resolution of the detector was good enough to clearly identify the second (0^+, 972 keV) and third (3^+, 1014 keV) excited states grouping in ^{28}Al, but it was impossible to estimate the population of the first (2^+, 30 keV) excited state in the same nucleus.

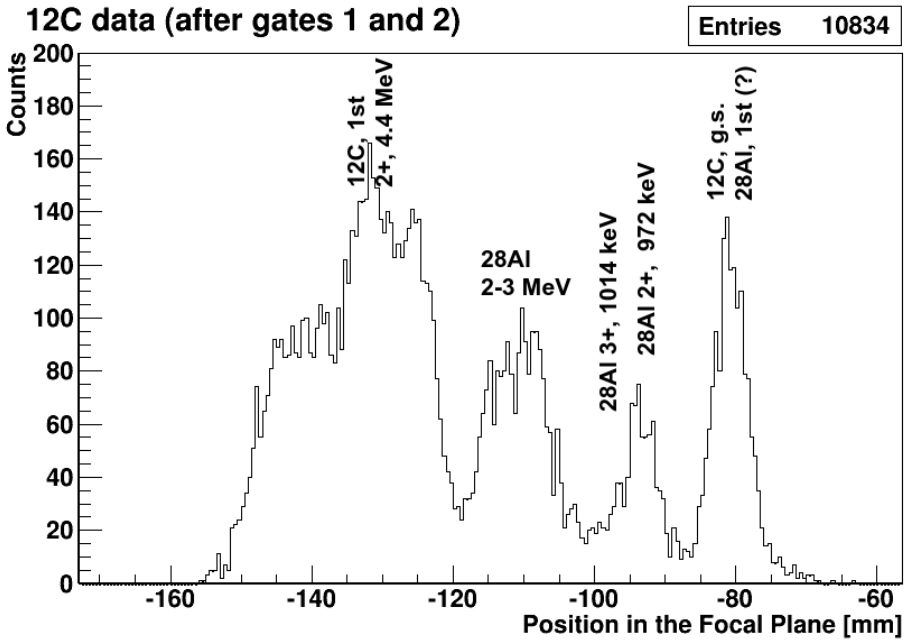

Figure 5.11: Gated 1-D spectrum showing the position of elastic and inelastic states in ^{12}C and ^{28}Al at 4°-8° in the lab.

Eight similar histograms were produced by placing angular gates of 0.5° width on the data in Figure 5.11 and were used in the analysis. These steps were performed over the angular range mentioned above at each MDM angle where the data were sufficient. The final cross-section distribution obtained for the ground-state in ^{28}Al (J^π=3^+) can be seen in Figure 5.12. The uncertainties in the transfer cross-section estimations were given by: statistical uncertainties (6%-20%), the target thickness uncertainty (7.7%), the FC

normalization error (1%) and the uncertainty in the estimation of inelastic contributions (1%).

The theoretical distribution was obtained using PTOLEMY's DWBA procedure. The calculations were performed using the best OMP parameters from Tables 5.2 and 5.3, specifically WS, WS^2 and JLM1 (J_V=63). For each OMP set, the same parameters were used in both the entrance and exit channels, as we could not obtain the elastic OMP parameters for the exit channel. The geometry of the neutron-binding potential was given by r = 1.15 fm and a = 0.60 fm. The normalized DWBA distributions can be seen in Figure 5.12 along with the experimental data.

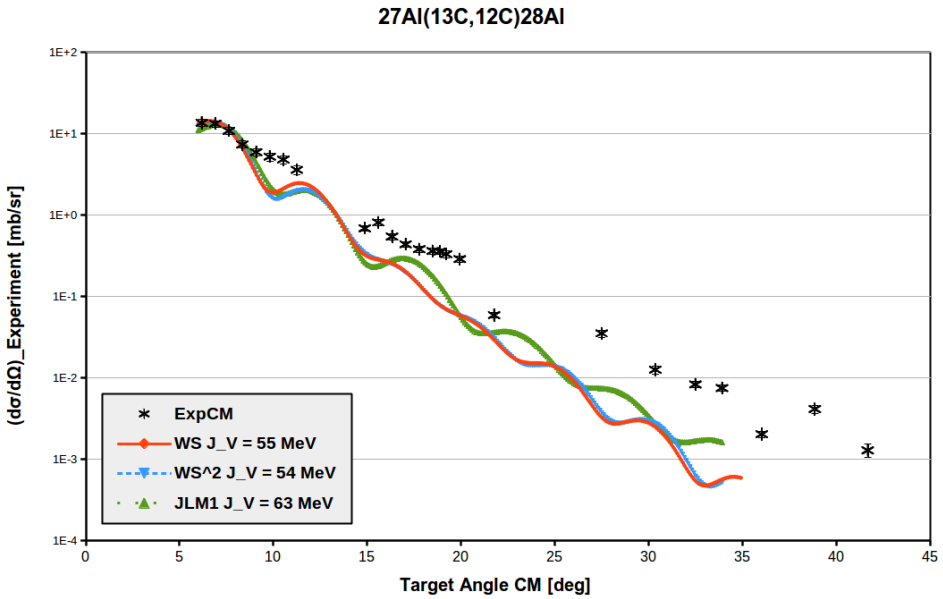

Figure 5.12: Experimental angular distribution for the cross-section of the one-neutron transfer reaction channel of ^{13}C on ^{27}Al target. The X-axis error bars are given by the detector angular resolution multiplied by the statistical percentage error. The Y-axis error bars are explained in the text. DWBA calculations are also plotted for different OMP parameters color-coded as shown in the legend.

It can be seen that all the calculated distributions are similar around the first peak. At

larger angles, the WS-based distributions continue to be similar, while the DF-based shows more pronounced oscillations. However, neither of the distributions manages to describe the transfer data beyond the first 4-5 points. Therefore only these points were used in the ANC determination, along with all three DWBA theoretical distributions. A closer view of this region of the distribution can be seen in Figure 5.13.

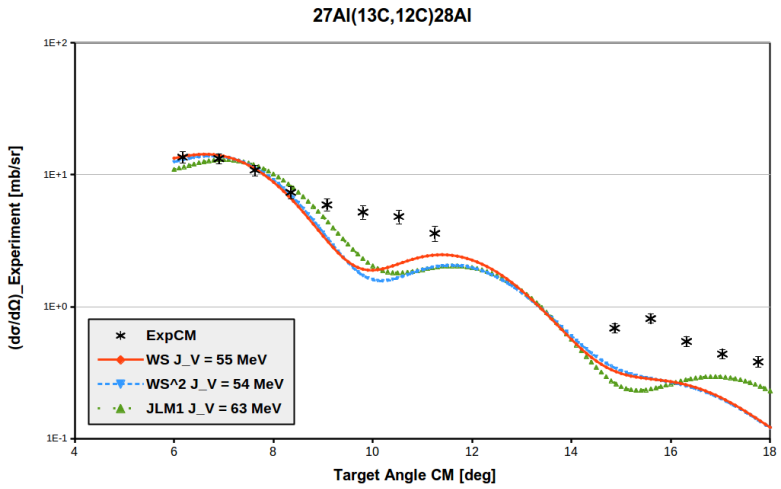

Figure 5.13: A closer view of the 6°-18° region of the transfer cross-section distribution obtained with ^{13}C on ^{27}Al. The DWBA calculations are also plotted for different OMP parameters as shown in the legend. The X-axis error bars are given by the detector angular resolution multiplied by the statistical percentage error. The Y-axis error bars are explained in the text.

Having the calculated and experimental cross-sections, the other parameters that are needed to obtain the ANC of ^{28}Al are the ANC of ^{13}C and the single-particle ANCs, $b(^{13}C)$ and $b(^{28}Al)$. The single-particle ANCs were determined using Eq. 2.70, using PTOLEMY to calculate the bound-state wave-functions and a short FORTRAN code that calculated the ratio of the Whittaker function to the radius. It should be noted that the code takes into account the transferred particle being a neutron and uses the Hankel function instead of Whittaker.

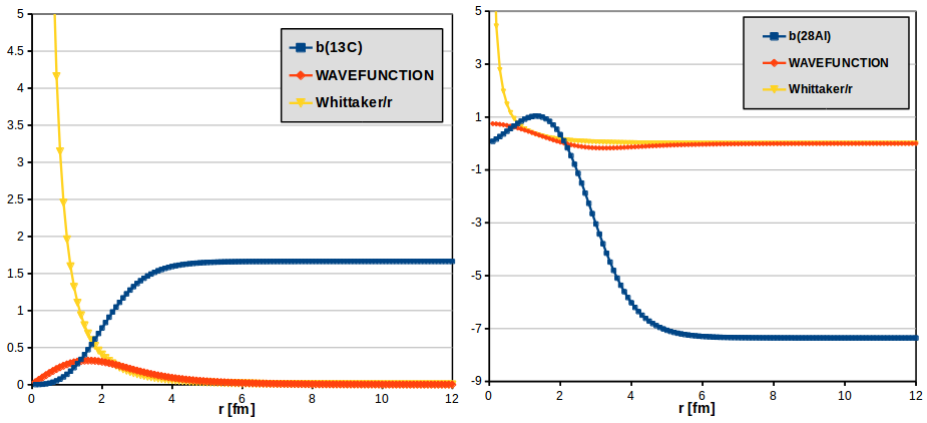

(a) (b)

Figure 5.14: (a) Plot showing the bound-state wave-function (red), Whittaker-to-r ratio (yellow) and single-particle ANC (blue) for ^{13}C. (b) Plot showing the bound-state wave-function (red), Whittaker-to-r ratio (yellow) and single-particle ANC (blue) for ^{28}Al.

For the capture of a neutron into the $1p_{1/2}$ ground state of ^{13}C, l=1 and the Sommerfeld parameter is 0. The wave-function calculated by PTOLEMY can be seen in Figure 5.14, (a) drawn in red. The Whittaker-to-r function can also be seen in (a) drawn in yellow. The ratio between the two functions gives the single-particle ANC and is plotted in (a) in blue. $b(^{13}C)$ was extracted from the asymptotic region as 1.66 fm$^{-1/2}$. For the capture of a neutron into the $2s_{1/2}$ ground state of ^{28}Al, l=0 and the Sommerfeld parameter is 0. Figure 5.14, (b) shows the similarly calculated bound-state wave-function, Whittaker-to-r ratio and single-particle ANC for ^{28}Al. $b(^{28}Al)$ was extracted from the asymptotic region as 7.36 fm$^{-1/2}$. The ANC of ^{13}C, $C^2_{1p_{1/2}}$ = 2.31 ±0.08 fm^{-1}, was taken from Ref. [40].

The extracted values for the $S_{2s_{1/2}}$ and $C^2_{2s_{1/2}}$ using each DWBA calculation can be seen in Table 5.4. The sources of uncertainty in each case include: the uncertainties of the experimental cross-sections, the geometry of the neutron binding potential used in the DWBA calculations (1.5%) and the normalization between the measured and the calculated cross sections (5-10%).

	$S_{2s_{1/2}}$	ΔS	$C^2_{2s_{1/2}}$ [fm^{-1}]	ΔC^2
WS	0.19	0.01	10.22	0.75
WS^2	0.16	0.01	8.76	0.59
JLM1 (J$_V$=65)	0.10	0.01	5.19	0.57
Average	0.18	0.01	9.46	0.47

Table 5.4: Spectroscopic factors and ANCs for ^{28}Al, obtained from a ^{13}C beam on a ^{27}Al target.

The final value for each $S_{2s_{1/2}}$ and $C^2_{2s_{1/2}}$ was determined using an average of the first 2 determinations weighted by their uncertainties. The ANC value extracted using the JLM1-DWBA calculations was too far off from the results obtained with the Woods-Saxon type DWBA models and therefore, it was excluded from the average.

5.2 The ^{13}C(^{27}Al, ^{28}Al)^{12}C Experiment

There were two aims behind the measurement of the reaction ^{13}C(^{27}Al, ^{28}Al)^{12}C. The first was to provide further proof of the success of the Oxford detector upgrade and its new capability to identify nuclei heavier than A = 26. The second purpose was to extract the ANC of the ground state of ^{28}Al, and use it to determine the ANC of the mirror state in ^{28}P. The data analysis procedure follows the same steps that were presented in the previous section. An average of the two final values obtained for the ANC will be used in the determination of the astrophysical rate which will be presented in chapter 6.

The experiment was performed using a beam of ^{27}Al at E$_{\text{Lab}}$ $\approx$11.8 MeV/A. There were only two targets used, ^{197}Au for calibration and ^{13}C for reaction data, with the thicknesses listed in Table 5.1. The Oxford detector was filled with isobutane at 50 Torr pressure. The calibrations in position and angle were done with the MDM at 4° following the procedures described in sections 3.2.3 and 3.2.4. Figure 5.15, (a) shows the calibrated focal plane position spectrum for scattering on the gold target through the 5-finger mask. The resolution of the position peak was $\approx$4 mm. From the same data, Figure 5.15, (b) shows the cali-

brated target angle. The detector angular resolution was extracted from this spectrum and found ≈0.3°.

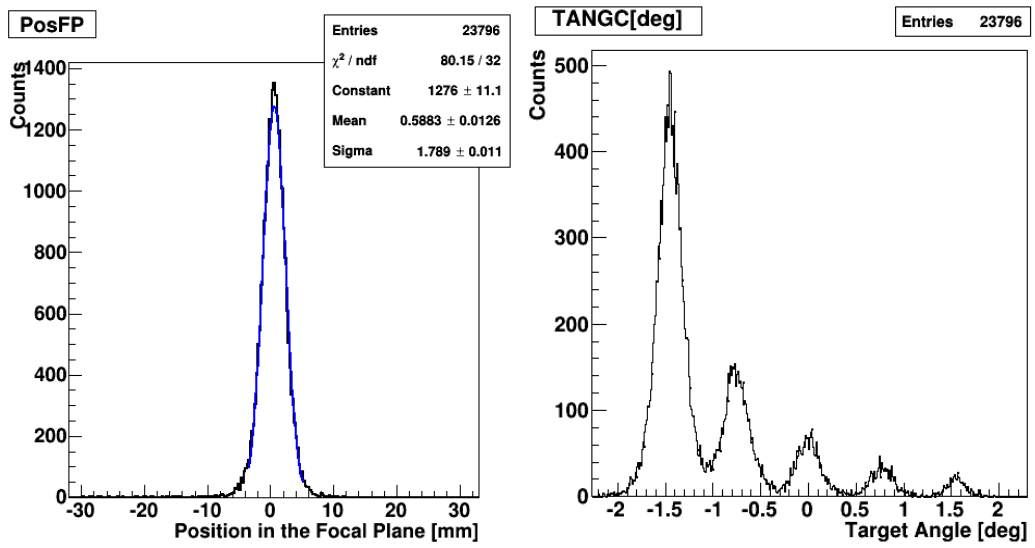

(a) (b)

Figure 5.15: Spectra showing calibration data from the scattering of the ^{27}Al beam on a gold target at 4° lab. (a) Histogram of the reconstructed focal plane. (b) Histogram of the target angle showing the 5 fingers corresponding to the slits in the 5-finger mask.

Also from this spectrum, the peaks were integrated and used to find the FC normalization. Figure 5.16 shows the experimental scattering cross-section on gold fitted with a Rutherford curve. From the five points showed, the normalization factor was found as ≈0.54.

Resolutions of the various energy detection elements were estimated by fitting the corresponding scattering peaks and applying Eq. 4.4. For the ionization chamber, the resolution was ≈ 5.3%. The Micromegas resolution was found to be ≈ 5%. For the residual energy, the resolution was ≈ 13%. The total energy loss was calculated as well

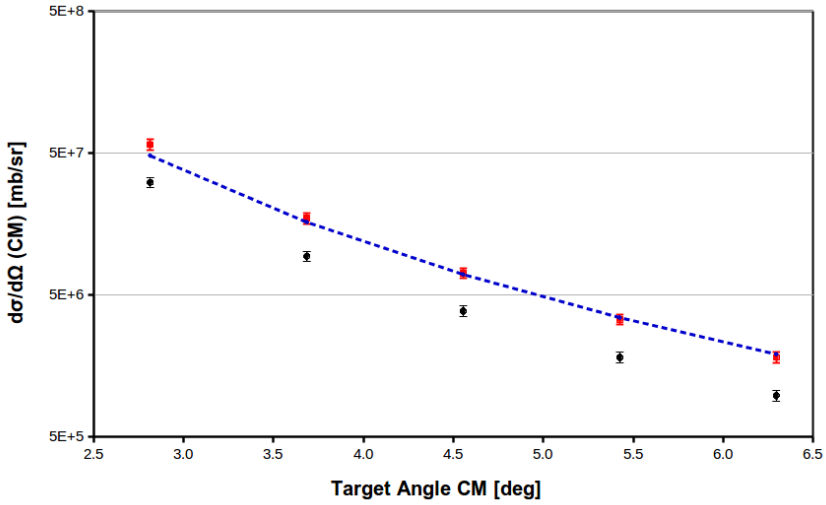

Figure 5.16: Comparison between scattering data and Rutherford calculations for ^{27}Al on ^{197}Au. Black dots represent cross-section estimations with a 1.0 normalization factor. The blue line shows the Rutherford curve. Red squares show the data renormalized to fit the curve.The X-axis error bars in the experimental data are given by the detector angular resolution multiplied by the statistical percentage error. The Y-axis error bars indicate the uncertainty in the experimental cross-section which is dominated by the target thickness error.

by summing arithmetically dE1 and EMuO and its resolution was found as ≈ 3.53%.

5.2.1 *The elastic scattering data*

The differential cross-section for elastic scattering on ^{13}C was measured at 4 different MDM angles: 4°, 7°, 10° and 13°. Using the '4 by 1' mask, the angular range covered was 2°–15° in the laboratory frame and ≈7°–47° in the center of mass frame, with 1° of overlap for consistency checks. In order to obtain the elastic cross-section, it was necessary to first isolate the ^{27}Al data points from the rest. The steps taken for that are similar to those described in the previous section, but will still be presented in a summary here.

Figure 5.17 shows a 2-D (dEtot vs PM) identification spectrum with the various nuclei produced in the different reaction channels that occur. The topmost 'line' corresponds to the primary beam and related isotopes (Z=13). Each of the lines below, with lower dEtot,

represents species with increasingly smaller Z number.

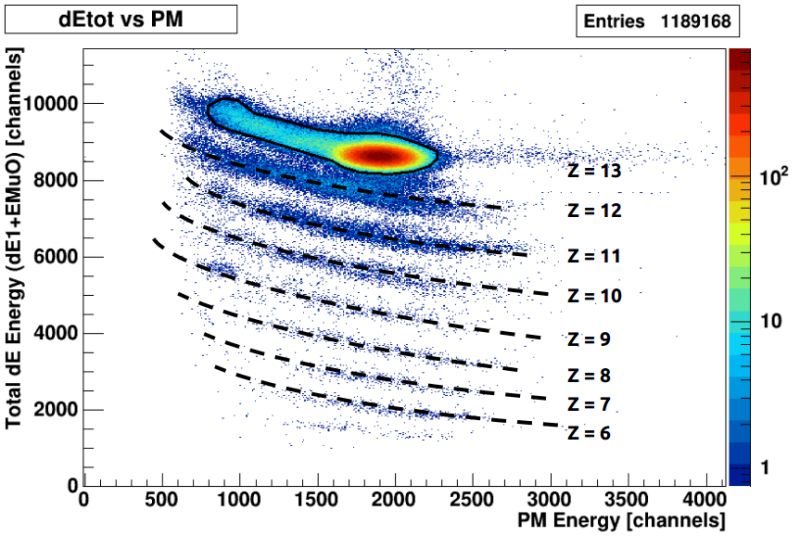

Figure 5.17: 2-D particle identification spectrum for ^{27}Al + ^{13}C at 2°-6° in the lab frame. Dotted lines indicate particles with the same Z. The closed ellipse indicates the software gate placed to isolate the Al nuclei.

Putting a snug gate around the nuclei of interest, in this case Al, and plotting the data in a focal plane position vs residual energy plot gives the distribution shown in Figure 5.18. The different colors of the ellipses indicate different isotopes of Al. Drawing another gate around the data indicated by the black ellipse will isolate the ^{27}Al events.

Figure 5.19 shows the data that is valid under these 2 gating conditions. The horizontal bands correspond to the ground state and first inelastic state ($1/2^+$, 843.8 keV) in ^{27}Al. As seen in the figure, at 2°-4° lab angles, the data around the ground state is contaminated by scattering off impurities (the slanted bands). Analysis with RAYTRACE identified the main contributors as ^{56}Fe and ^{28}Si. It can also be seen that the ground state and first excited state bands overlap. The position resolution of 4 mm mentioned before is equivalent to $\sim$700 keV, which is very close to the energy gap between the two states. Unfortunately,

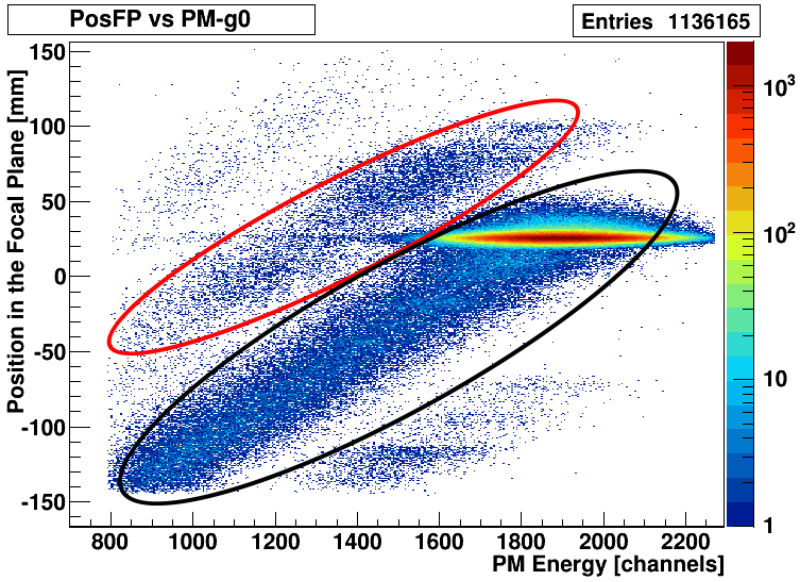

Figure 5.18: 2-D spectrum for ^{27}Al + ^{13}C showing the data inside the gate on Z=13. The red ellipse indicates data points corresponding to ^{28}Al, while black is for ^{27}Al.

this is due to the limited resolution of the avalanche counters and could not be improved any further.

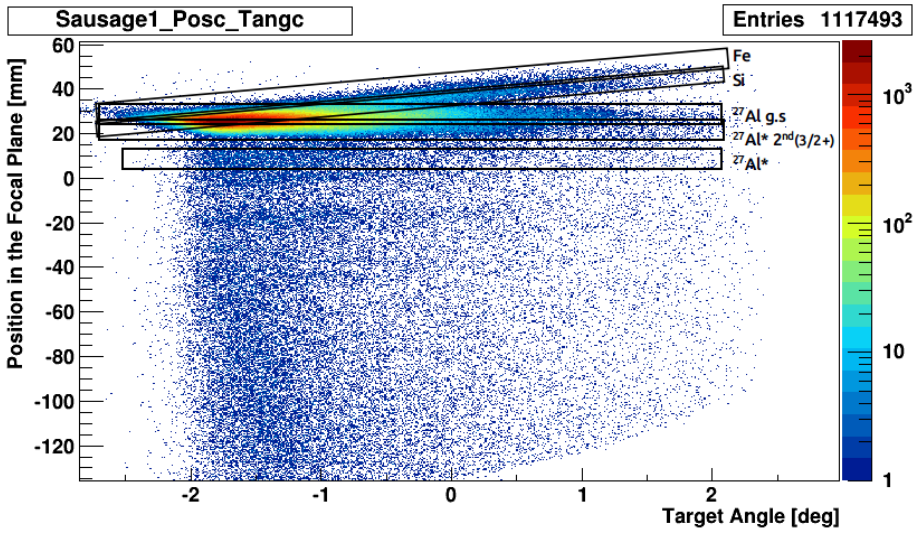

Figure 5.19: Plot of the gated data in focal plane position versus reconstructed target angle. Impurities are identified, as well as the elastic scattering state.

Figure 5.20 shows the data from Figure 5.19 projected on the X and Y axis, with (a) showing the position in the focal plane spectrum and (b) showing the target angle spectrum. In order to resolve the contribution of the impurities, the corresponding scattering was assumed to be Rutherford (up to ≈9° in C.M. for Fe and ≈6° for Si).

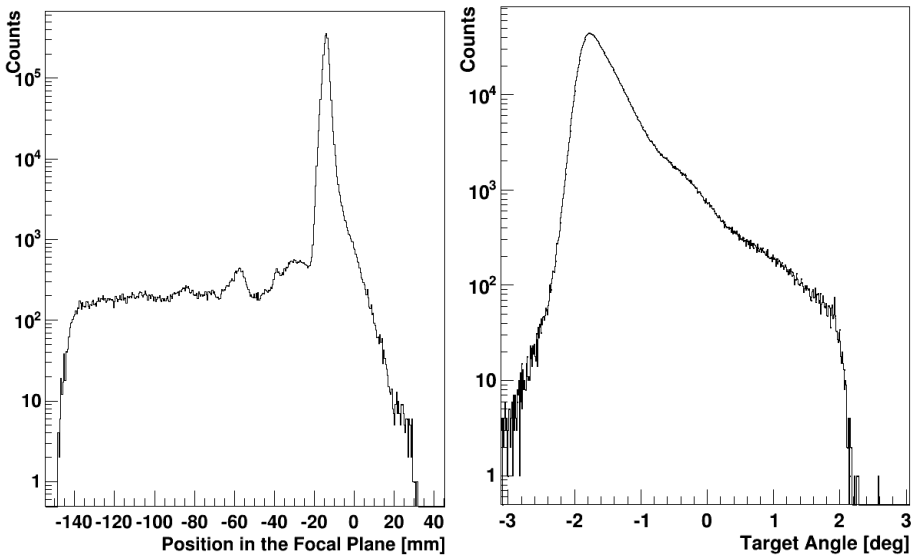

(a) (b)

Figure 5.20: Elastic scattering data plotted in (a) the focal plane spectrum and (b) the target angle spectrum.

The experimental cross-sections for the two nuclei were calculated in the lab range 4°-6° and fitted with corresponding Rutherford curves. The normalization was then used to estimate the impurities' contribution to the angular range of 2°-4°. For this, as well as the elastic cross-section determination, the 4° angular range of the mask was divided into 8 bins of 0.5° width each. Figure 5.21 shows the normalization to Rutherford for Si (red) and Fe (blue). It appears that the contamination in the target is approximately 2% for the former and 0.4% for the latter.

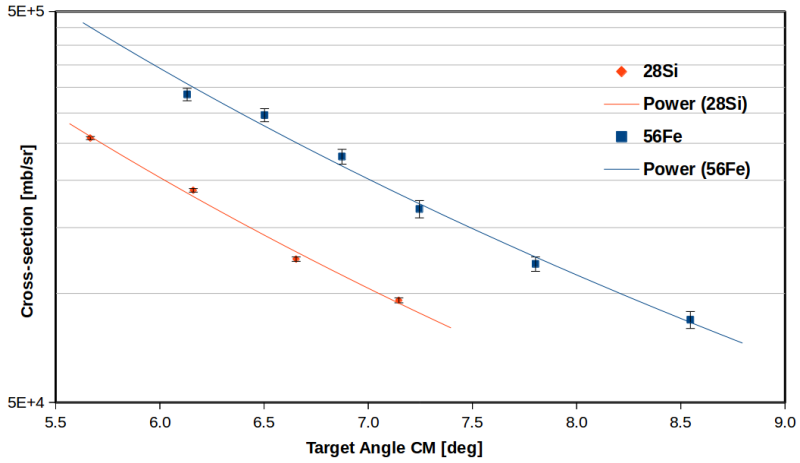

Figure 5.21: Normalization to Rutherford for the calculation of contamination by impurities: Si (red) and Fe (blue). Symbols indicate experimental data and the continuous lines indicate the Rutherford cross-section calculation. The X-axis error bars in the experimental data are given by the detector angular resolution multiplied by the statistical percentage error. The Y-axis error bars are explained in more detail in the text.

At higher angles, the impurities were well separated from the elastics data in the focal plane and they were ignored. The measured elastic cross-section is shown in Figure 5.22. The data points come from 2 separate experiments and they represent the average between the two values for each angle. The different colors indicate the MDM angle for which those specific data points were taken. It should be noted that there are no data points for 13° as the statistics at that angle were not sufficient.

Where there was overlap of data points from different MDM angles, the cross-sections were averaged into one result per angle. In one cases, the data point was removed from the distribution because it belonged to an angle close to the edge of the collimation mask where overestimation or underestimation of the cross-section can occur. Figure 5.23 shows the final distribution of the elastic cross-section. The uncertainties of the cross-section distribution points shown in Figures 5.22 and 5.23 were given by: statistical uncertainties (0.5%-10%), the target thickness uncertainty (7.5%), the FC normalization error (1.1%)

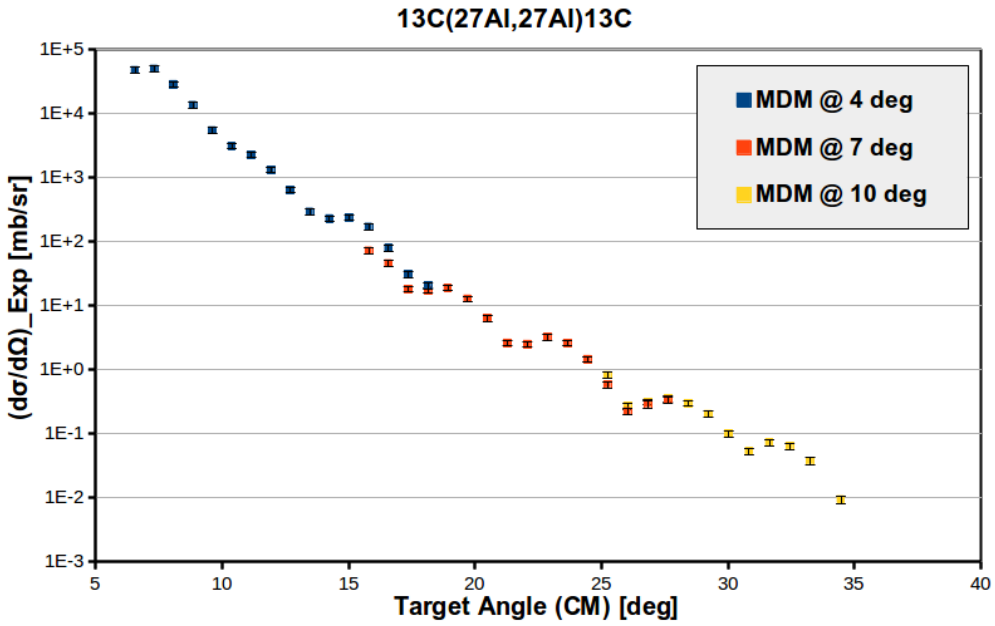

Figure 5.22: Experimental angular distribution for the elastic cross-section. The MDM angles are denoted by different colors: blue for 4°, red for 7° and yellow for 10°. The X-axis error bars are given by the detector angular resolution multiplied by the statistical percentage error. The Y-axis error bars are explained in the text.

and the uncertainty in the estimation of inelastic and impurities contamination (5%).

5.2.2 *The optical model parameters*

As with the direct kinematics reaction, the elastic scattering data were fit using the Wood-Saxon model, a squared WS form, as well as double-folding shapes using the same computer codes. The grid search for the strength of the real component of the WS potential is shown in Figure 5.24. It can be seen that the region below ≈150 MeV has the minimum χ^2 but does not give a discrete set of potentials to try. Above ≈150 MeV there are three distinct minima but the corresponding χ^2 is larger. Six values of V were chosen for the fitting procedure: 10 MeV, 30 MeV, 70 MeV, 170 MeV, 230 MeV and 270 MeV. The 3 best results and the corresponding parameters are shown in Table 5.5. The table also includes the results of the fitting analysis done with the squared form of WS. Figure 5.25 shows the

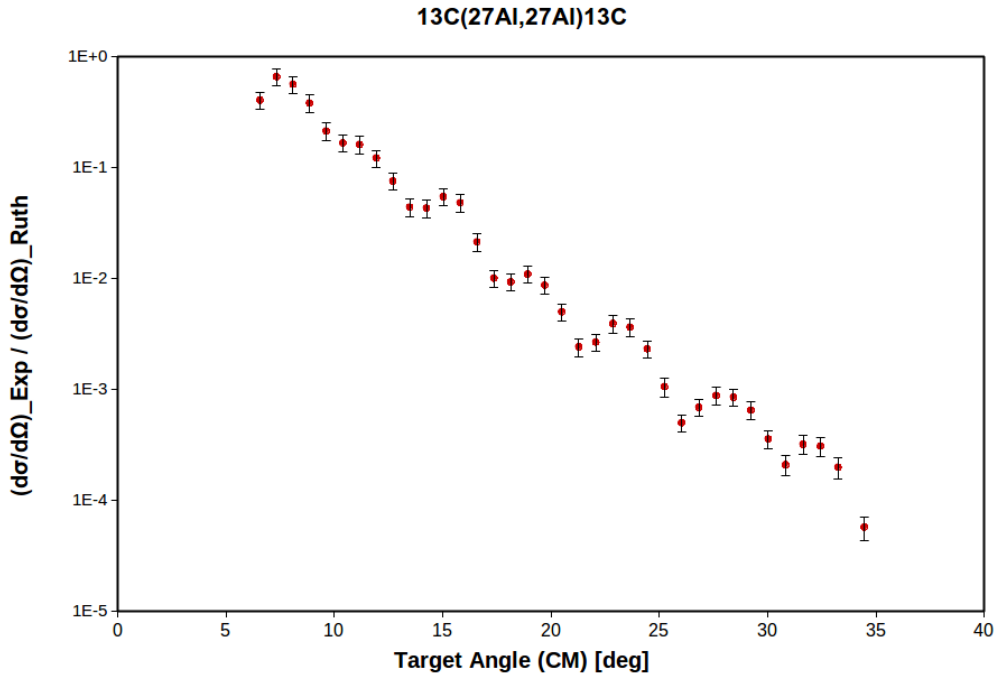

Figure 5.23: Experimental angular distribution for the elastic cross-section of ^{27}Al+^{13}C normalized to the Rutherford cross-section. The X-axis error bars are given by the detector angular resolution multiplied by the statistical percentage error. The Y-axis error bars are explained in the text.

experimental data and the fits with the lowest χ^2. As can be seen, the agreement between the theory and the experiment is excellent.

As mentioned, the data was also fitted with the double-folding form-factors described in Chapter 2. The M3Y model was more successful at describing the elastic cross-section than the JLM interaction, but neither worked as well as the Woods-Saxon OMP. It should be noted that the fitting procedure required the data to be normalized by a factor of 0.57, irrespective of the computer code used or the OMP model. It is uncertain where the discrepancy comes from, but most likely from the FC correction. The parameters obtained for the double-folding fits are shown in Table 5.6, while the fits themselves can be seen in Figure 5.26.

Pot. Type	V [MeV]	W [MeV]	r_V [fm]	r_W [fm]	a_V [fm]	a_W [fm]	χ^2	σ_R [mb]	J_V [MeV fm^3]	R_V [fm]	J_W [MeV fm^3]	R_W [fm]
WS	27.	23.72	0.9783	1.1039	1.0068	0.6958	2.61	1730.	63.	5.5180	66.	5.2562
WS	56.98	25.03	0.7993	1.0990	1.0719	0.7099	4.81	1761.	86.3	5.1807	69.5	5.2645
WS	168.73	13.66	0.8128	1.4616	1.0242	0.7008	8.66	2526	256.6	5.0830	84.2	6.5947
WS^2	20.	27.36	1.2335	1.2041	1.4908	1.0019	2.73	1606.	49.	5.6490	64.	5.0720

Table 5.5: The Woods-Saxon OMP parameters obtained from fitting the elastic scattering cross-section of ^{27}Al + ^{13}C. In all 5 cases, the Coulomb radius was fixed at r_C = 1.0 fm.

Pot. Type	N_V	N_W	t_V [fm]	t_W [fm]	χ^2	σ_R [mb]	J_V [MeV fm^3]	R_V [fm]	J_W [MeV fm^3]	R_W [fm]
M3Y(ZR)	0.1720	0.3497	0.8191	0.9626	4.81	1794.	75.20	5.252	154.29	4.476
M3Y(FR)	0.1400	0.2649	0.8092	0.9346	4.86	1785.	65.88	5.386	125.61	4.671
JLM1	0.1300	0.7901	0.7988	0.9141	5.37	1716.	69.17	5.307	88.23	4.878
JLM3	0.1450	0.9974	0.7960	0.9265	5.41	1722.	71.23	5.276	94.75	4.800

Table 5.6: The Double-Folding OMP parameters obtained from fitting the elastic scattering cross-section of ^{27}Al + ^{13}C with the shapes described in Chapter 2, the M3Y and JLM.

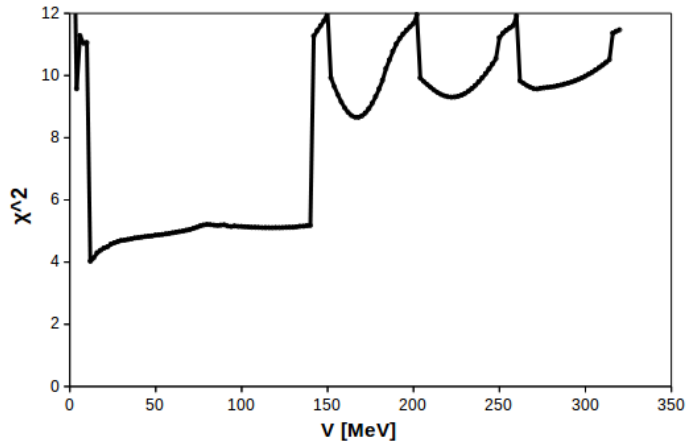

Figure 5.24: Grid search for the strength of the real component of the Woods-Saxon optical potential.

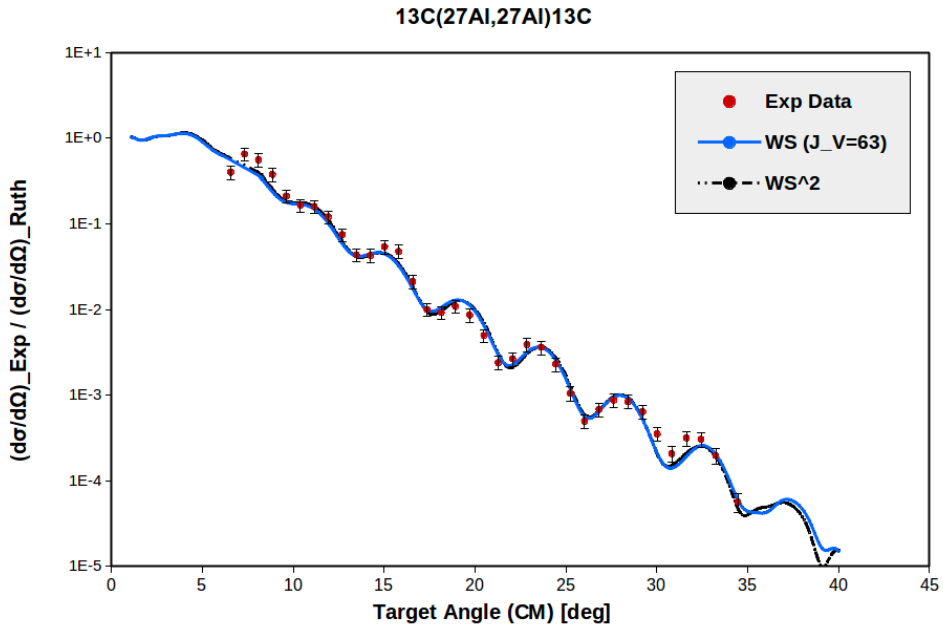

Figure 5.25: Plot showing the experimental cross-section distribution of $^{27}Al+^{13}C$ normalized to the Rutherford cross-section fitted with the optical potentials $WS(A)$, blue continuous line, and WS^2, black dashed line.

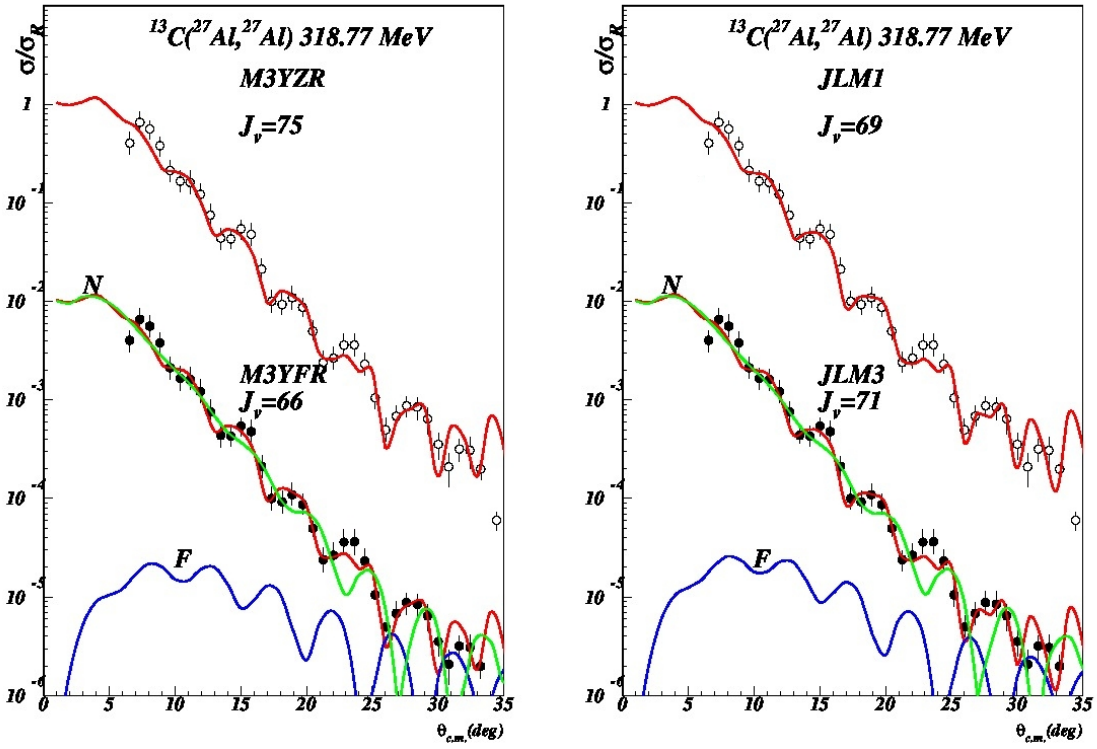

(a) (b)

Figure 5.26: Plot showing the experimental cross-section distribution of ^{27}Al+^{13}C normalized to the Rutherford cross-section fitted with the double folding potentials (a) M3Y(ZR and FR) and (b) JLM (1 and 3). The empty circles indicate experimental data and the red lines denotes the OMP fits. The black circles indicate the same data but divided by a factor of 100 for easier comparison. Near and Far components are also indicated, in green and blue, respectively.

5.2.3 *The neutron transfer data and the ANC determination*

The neutron transfer reaction was measured at the same MDM angles as the elastic scattering, but the very low reaction cross-section at 10° and 13° meant that there was little to no statistics collected for the transfer channel. As such, the angular range covered in C.M. for this channel was 6°-26°. Figure 5.27 shows the PID process for the transfer data collected at 4°. Plotted in (a) is the position versus total energy loss histogram after

a first gate (not shown here) on the Al events. That data in the black gate from (a) were plotted in (b) in a focal plane position histogram.

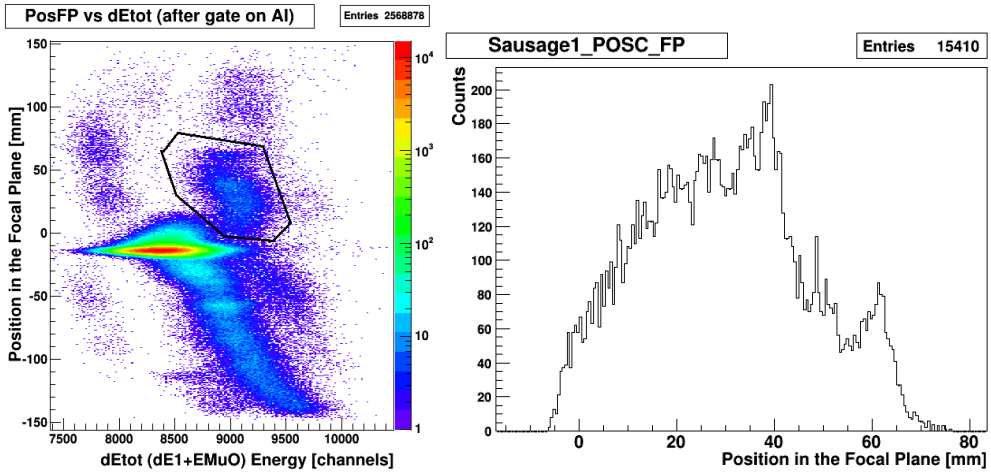

(a) (b)

Figure 5.27: 2-D particle identification spectra for $^{13}C(^{27}Al,^{28}Al)^{12}C$ at 4°-8° in the lab frame. (a) Aluminum events plotted in a Position versus dEtot histogram showing the second gate that is placed around the ^{28}Al particles for the analysis of the transfer channel. (b) Data from the gate in spectrum (a) plotted in a focal plane position histogram.

Angular cuts of 0.5° width were made on the data in Figure 5.27, (b). The resulting 8 position histograms each had to be fitted with a sum of Gaussian functions in order to properly account for the overlap between the 3^+ ground state in ^{28}Al and the second excited state (0^+, 972 keV). The first excited state, 2^+ at 30 keV, could not be clearly identified and it is unknown if it was significantly populated in this experiment.

Figure 5.28 shows the experimental distribution obtained for the ground-state of ^{28}Al. The uncertainties of the transfer cross-section points were given by: statistical uncertainties (3%-20%), the target thickness uncertainty (7.5%), the FC normalization error (1.1%) and the uncertainty in the estimation of inelastic and impurities contamination (5%).

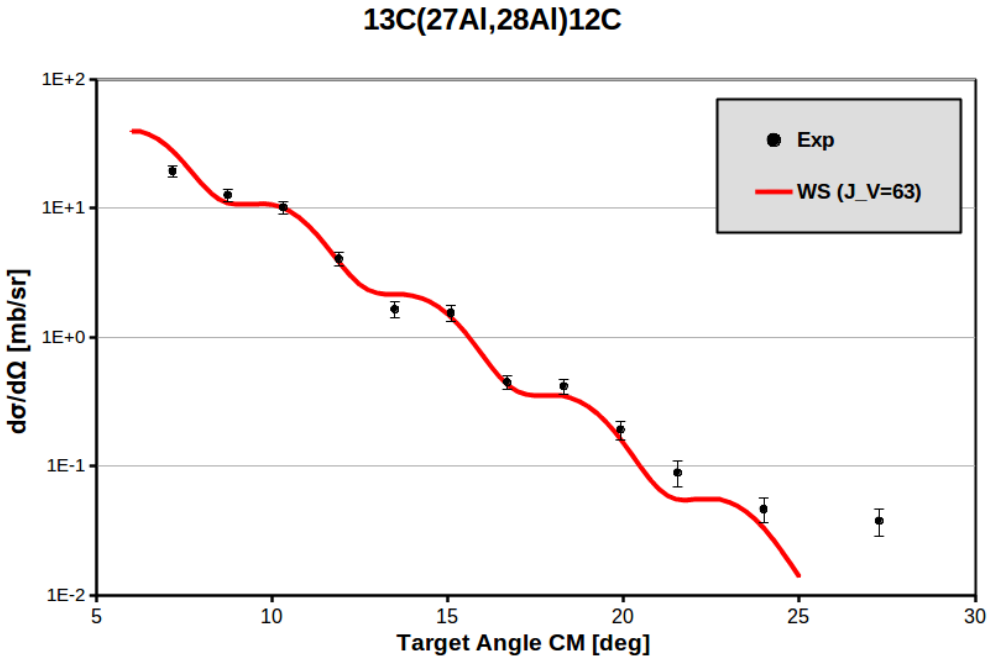

Figure 5.28: Experimental angular distribution for the cross-section of the one-neutron transfer reaction channel of ^{27}Al on ^{13}C target. The DWBA calculations obtained with the WS (J_V=63) OMP parameters are also shown, with the red line. The X-axis error bars are given by the detector angular resolution multiplied by the statistical percentage error. The Y-axis error bars are explained in the text.

The theoretical angular distribution was obtained using PTOLEMY's DWBA procedure. The calculations were performed using the best OMP parameters from Tables 5.5 and 5.6, specifically WS (J_V=63). As for the direct kinematics reaction, these parameters were used in both the entrance and exit channels. The geometry of the neutron-binding potential was given by r = 1.15 fm and a = 0.60 fm. The normalized DWBA distribution can be seen in Figure 5.28 along with the experimental data, showing excellent agreement.

In order to obtain the ANC, $C^2_{2s_{1/2}}$, it was only necessary to apply Eq. 2.72 since the other parameters were already calculated in the direct kinematics section. The spectroscopic factor was found to be $S_{2s_{1/2}}$ = 1.64, while the ANC was $C^2_{2s_{1/2}}$ = 89.00 fm^{-1}. The sources of uncertainty here included: the uncertainties of the experimental cross-sections

as explained above, the geometry of the neutron binding potential used in the DWBA calculations (1.5%) and the normalization between the measured and the calculated cross sections (2-10%). All these lead to an uncertainty of 6.3%. Therefore the final results for the inverse kinematics study are $S_{2s_{1/2}}$ = 1.64 ±0.10 and $C^2_{2s_{1/2}}$ = 89.00 ±5.61 fm^{-1}.

5.3 Comparison of the Analysis Results

As shown so far, the focus of this project was such that it allowed the study of the reaction, ^{13}C + ^{27}Al, in direct as well as inverse kinematics. In each case, the center-of-mass energy of the system was $E_{CM} \approx 104$ MeV and as such, the theory states that the cross-section distributions should be identical in the C.M. system. In general, a reaction is rarely studied in both types of kinematics with such similar C.M. conditions so this presents a rare opportunity for comparison.

Figure 5.29 shows the experimentally determined direct and inverse cross-section distributions for the elastic channel.

Unfortunately, as the figure shows, the two distribution do not agree with each other except for a very small angular region where they intersect. The reasons for this disagreement are not known presently. However, there are various possibilities. For both sets of data, incorrect estimations of the inelastic and impurities contributions could lead to such discrepancies in the results.

Another, very strong, possibility is that in inverse kinematics, the vertical dispersion of the scattered beam is much larger than expected. In this situation, a significant number of particles would not be able to reach the scintillator at the back of the detector. The acquisition system would not be triggered and data would be lost. This effect would be increasingly more significant at larger angles and could account for the sharp drop in the inverse distribution, as well as for the shift in angle.

On the other hand, the OMP analysis would suggest that instead, the problem lies with

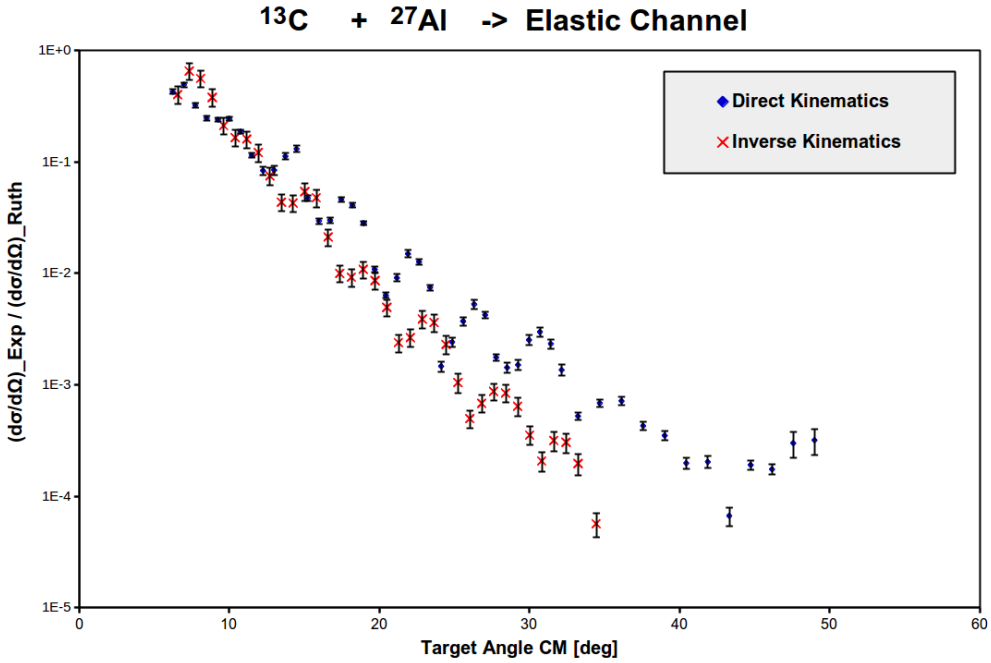

Figure 5.29: Comparison between the elastic cross-section distributions obtained in direct and inverse kinematics for ^{13}C + ^{27}Al.

the direct kinematics distribution. The above mentioned dispersion effect would not be a significant issue with the lighter ^{13}C as a projectile. However, this leaves a big question mark as to the reason behind the disagreement and possible contamination as the main possibility.

In a similar comparison, Figure 5.30 shows the experimentally determined direct and inverse cross-section distributions for the transfer channel.

Once again, the plot shows disagreement between the two sets of data, especially at very forward angles. However, the pattern of differences seems consistent with the one visible in Figure 5.29. This would suggest that there is a systematic effect at work. A more detailed investigation of this issue was outside the scope of this dissertation, but it is recommended that a similar study, involving both direct and kinematics measurements

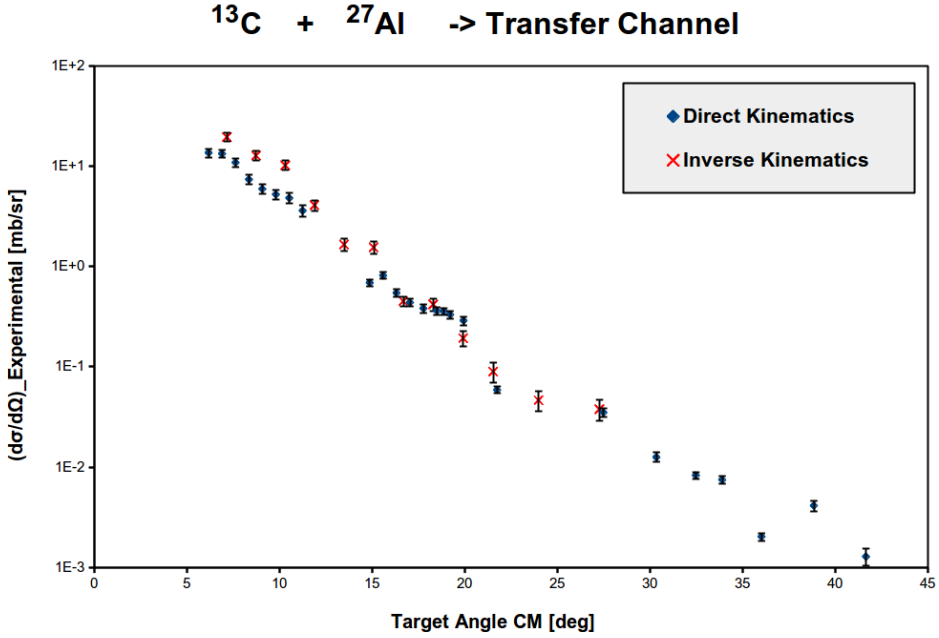

Figure 5.30: Comparison between the transfer cross-section distributions obtained in direct and inverse kinematics for ^{13}C + ^{27}Al.

of the same reaction be performed in the future aimed at identifying the cause of these disagreements.

It is particularly important to determine if the underlying issues lie with the theory. DWBA models are sensitive not just to the choice of optical potential but also to the reaction mechanisms used in the models. Some of them have been developed for lighter ions but could be applied to slightly heavier ones as well. It is possible that ^{27,28}Al is outside the range of nuclei to which these models can be applied.

Given the future plans to expand the ANC studies into the mass region beyond A=28, this issue will need to be understood properly.

	$S_{2s_{1/2}}(^{28}Al)$	$C^2_{2s_{1/2}}(^{28}Al)$ [fm^{-1}]
Direct Kine	0.18 ±0.01	9.46 ±0.47
Inverse Kine	1.64 ±0.10	89.00 ±5.61

Table 5.7: Spectroscopic factors and ANCs for ^{28}Al.

5.4 Extracting the ANC and Spectroscopic Factor of ^{28}P

The final spectroscopic factor and ANC values for ^{28}Al obtained in the two previous sections are summarized in Table 5.7. It can be seen that the values obtained in direct kinematics are approximately a factor of 10 smaller than the results from inverse kinematics.

The possible reasons behind this difference in results have already been discussed in the previous section. In addition to those, it is important to remember that ANCs, as well as spectroscopic factors, depend significantly on the goodness of the agreement between OMP fits and the elastic angular distribution. The elastic and transfer distributions obtained in inverse kinematics agree very well with the theory, which is not the case with the direct kinematics data where the inaccurate OMP parameters throw off the DWBA analysis.

For this reason, the values adopted for use in the next steps of the analysis were chosen as $C^2_{2s_{1/2}}$ = 60. ±30. fm^{-1} and $S_{2s_{1/2}}$ = 1.11 ±0.56. An uncertainty of 50% was necessary to account for the systematic effects that are producing the discrepancies in the data and in the results of the DWBA analysis.

Having the spectroscopic factor and ANC of ^{28}Al, the same parameters could be extracted for the mirror nucleus, ^{28}P, using the following equality relations for mirror nuclei.

$$S_{2s_{1/2}}(^{28}P) = S_{2s_{1/2}}(^{28}Al) = 1.11 \pm 0.56 \tag{5.8}$$

$$\frac{C^2_{2s_{1/2}}}{b^2_{2s_{1/2}}}(^{28}P) = \frac{C^2_{2s_{1/2}}}{b^2_{2s_{1/2}}}(^{28}Al) \tag{5.9}$$

The single-particle ANC, $b^2_{2s_{1/2}}(^{28}P)$, was determined from Eq. 2.70 following the procedure described previously for $b^2_{2s_{1/2}}(^{13}C)$. The code PTOLEMY was used to generate the bound-state wave-function for a proton captured in a Woods-Saxon potential with the same parameters used for the neutron captured in ^{28}Al. The sole exception was the strength of the central potential, which was adjusted to reproduce the experimental proton binding energy in ^{28}P, E_p = 2.0523 MeV. The parameters, l=0, η=1.518 and κ=0.30933 were used in the Whittaker code to calculate the Whittaker-to-r function.

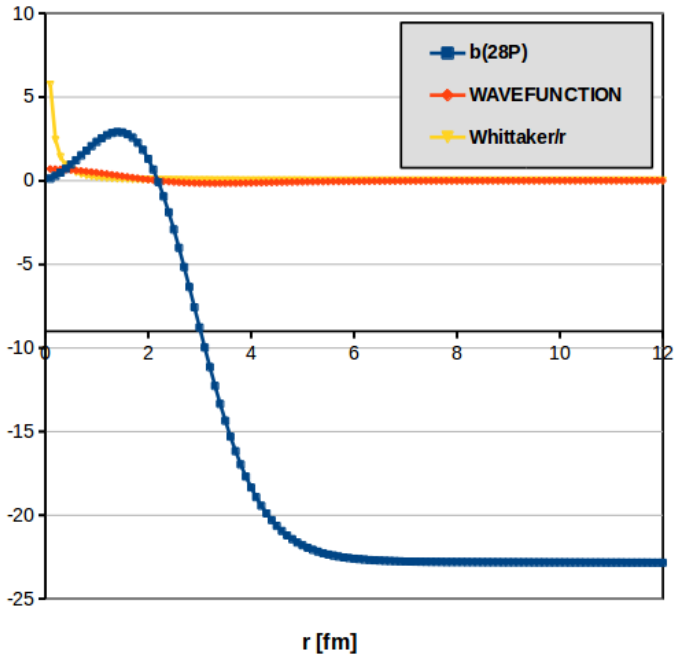

Figure 5.31: Plot showing the bound-state wave-function (red), Whittaker-to-r ratio (yellow) and single-particle ANC (blue) for ^{28}P.

Figure 5.31 shows the plots of the wave-function, the Whittaker-to-r function and the single-particle ANC. $b_{2s_{1/2}}(^{28}P)$ was extracted from the asymptotic region of the plot, where the value has stabilized at 22.85 fm$^{-1/2}$. Plugging this number in Eq. 5.9 leads to

the ANC of ^{28}P, $C^2_{2s_{1/2}}(^{28}P)$=(5.8 ±2.9) $\times$ 10^2 fm^{-1}. An uncertainty of 3% was added to account for possible charge-symmetry breaking effects [59].

The ANC and the spectroscopic factor will be used in Chapter 6 in the determination of the astrophysical proton capture rate.

6. THE ASTROPHYSICAL REACTION RATE AND CONCLUSIONS

6.1 The ^{27}Si$(p,\gamma)^{28}$P Reaction Rate

The total astrophysical rate of the ^{27}Si$(p,\gamma)^{28}$P reaction is given by the sum of the direct capture component and the resonant component. The direct capture reaction rate is given by Eq. 2.84 and requires knowledge of the effective astrophysical S-factor. $S_{\text{eff}}(E)$ was determined with the computer code RADCAP [60].

The FORTRAN program has 5 modules to calculate potentials (1), bound state energies (2), transition probabilities (3), phase-shifts (4), photo-dissociation cross-sections and astrophysical S-factors (5). Module 2 was used first to generate the ground-state wave-function file GSWF.INP based on the specific geometry of the potential requested by the user. In this case, the parameters described the proton binding Woods-Saxon potential used to calculate the single-particle ANC in the previous chapter. The depth of the central potential was adjusted to reproduce the proton binding energy to the ground-state of ^{28}P. Module 5 was then used to calculate the direct capture rate and the astrophysical S-factor for an energy range from 0.01 MeV to 2.0 MeV. Since RADCAP assumes that the spectroscopic factor of the capture reaction is 1.0, the results were multiplied by the experimentally-determined factor, $S_{2s_{1/2}}(^{28}\text{P})$ = 1.11 ±0.56. A plot of the astrophysical S-factor as a function of energy can be seen in Figure 6.1.

The points were fitted with a second degree polynomial function as drawn in Figure 6.1 with a red dashed line. The corresponding equation is shown in the figure. The coefficients represent the S-factor, its first derivative and its second derivative and can be found in Table 6.1 along with similar values estimated theoretically by Iliadis *et al.*. It can be seen that the value for S(0) is almost in agreement with the theoretical prediction.

These coefficients in Table 6.1 were then used in Eq. 2.82 to determine $S_{\text{eff}}(E)$. The

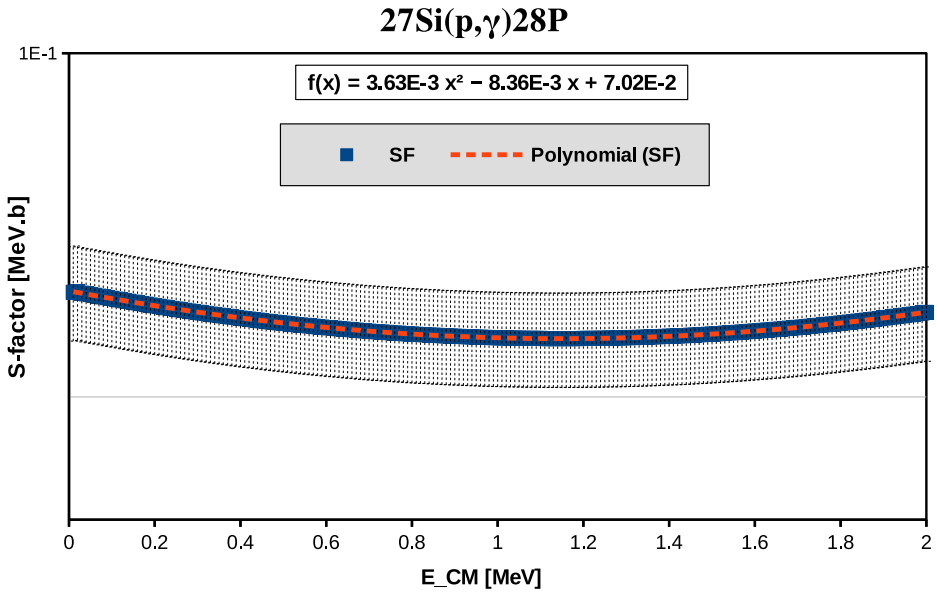

Figure 6.1: Plot showing the calculated S-factor for the reaction $^{27}Si(p,\gamma)^{28}P$ (blue squares) fitted with a polynomial function (red dashed line). The gray band above and below the calculations represents the uncertainty region and is given by the error of the spectroscopic factor.

conversion to T_9 was done based on Eq. 2.78 and $S_{\text{eff}}(T_9)$ was plotted in 6.2, (a). Having the effective astrophysical S-factor, the direct capture reaction rate per particle pair was calculated with Eq. 2.84 and plotted in 6.2, (b).

Since this rate has not been presented numerically in past literature, the direct capture rate was compared with the resonance rate as determined by Iliadis *et al.* in Ref. [2]. These points are shown in red in Figure 6.2, (b). It can be seen that the presently determined rate is $\sim$5 orders of magnitude lower than the resonance rate and therefore, does not have a significant effect on the total rate of the $^{27}\text{Si}(p,\gamma)^{28}\text{P}$ reaction. This result is in agreement with the most recent evaluations of this reaction [61].

	S(0) [MeV · b]	S'(0) [b]	S"(0) [b/MeV]
Present Work	4.75 ±2.38 × 10^{-2}	-5.66 ±2.83 × 10^{-3}	2.46 ±1.23 × 10^{-3}
Previous Work [2]	7.87 × 10^{-2}	-1.54 × 10^{-2}	1.00 × 10^{-2}

Table 6.1: Expansion coefficients of the total S-factor obtained in this work compared with previously determined values. The gray band above and below the calculations represents the uncertainty region and is given by the error of the spectroscopic factor.

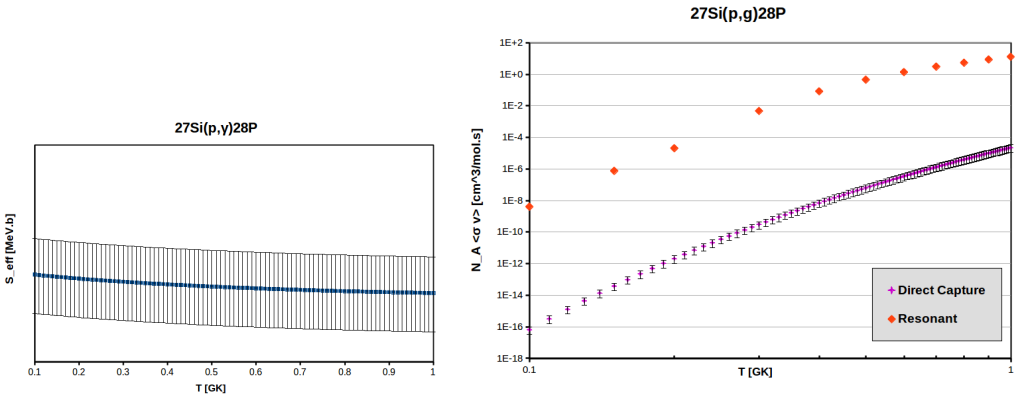

(a) (b)

Figure 6.2: (a) Plot showing the effective S-factor as a function of temperature for the region of interest, $T_9 \leq 1$. The Y-axis error bars are given by the error of the spectroscopic factor. (b) Plot showing the direct capture reaction rate estimated in the present work (magenta) and the resonant reaction rate estimated theoretically by Iliadis et al. in Ref. [2] (red). The Y-axis error bars are given by the error of the spectroscopic factor.

6.2 Conclusions

A two-part study has been completed, aimed at contributing to future studies in the fields of unstable beams and X-ray bursts nucleosynthesis.

The first part involved the upgrade of the Texas A&M Oxford focal-plane detector, an essential component of experiments focused on particle transfer reactions and the Asymptotic Normalization Coefficient method. The addition of Micromegas technology to the

Oxford detector was quick, low-cost and low-risk and was proven to be very successful. The resolution of energy loss in the detector was improved by a factor of $\sim$5 for low mass nuclei (A$\leq$16) and $\sim$3 for higher mass nuclei (A$\geq$28).

This result opens the way for ANC studies of higher mass nuclei of interest in X-ray bursts nucleosynthesis, such as ^{32}Cl and ^{36}K. Additionally, the success of this upgrade provides a different direction for the use of Micromegas technology, i.e. its addition to an existing detection system in lieu of building a new one, which is a more time-consuming and more complicated project.

The second part of the present work involved the use of the upgraded Oxford detector to study a reaction relevant to XRB nucleosynthesis. The direct capture reaction rate of ^{27}Si$(p,\gamma)^{28}$P was determined using the spectroscopic information extracted from the mirror reaction, ^{27}Al$(n,\gamma)^{28}$Al. The neutron capture itself was studied through the peripheral neutron transfer, ^{27}Al(^{13}C,^{12}C)^{28}Al, using the proven ANC indirect method.

The spectroscopic factor and ANC of ^{28}P were estimated experimentally for the first time as $S_{2s_{1/2}}(^{28}\text{P}) = 1.11 \pm 0.56$ and $C^2_{2s_{1/2}}(^{28}\text{P}) = (5.8 \pm 2.9) \times 10^2$ fm^{-1}. The theoretical predictions for the non-resonant reaction rate were confirmed as significantly lower than the resonant contribution.

A study of the resonances populated during the proton capture on ^{27}Si is the next step for future studies in order determine more accurately the effect of the reaction rate of ^{27}Si(p,γ) on the outcome of an X-ray burst.

REFERENCES

[1] J. Winfield, D. Pringle, W. Catford, D. Lewis, N. Jelley, and K. Allen, "Focal plane detector for the oxford mdm-2 spectrometer," *Nuclear Instruments and Methods in Physics Research Section A*, vol. 251, no. 2, pp. 297 – 306, 1986.

[2] C. Iliadis, P. M. Endt, N. Prantzos, and W. J. Thompson, "Explosive Hydrogen Burning of ^{27}Si, ^{31}S, ^{35}Ar, and ^{39}Ca in Novae and X-Ray Bursts," *The Astrophysical Journal*, vol. 524, pp. 434–453, Oct. 1999.

[3] C. E. Rolfs and W. S. Rodney, *Cauldrons in the Cosmos*. The University of Chicago Press, 1988.

[4] Space.com. `http://www.space.com/26218-astrophysics.html`. Accessed: 03-17-2015.

[5] National Nuclear Data Center, "Chart of Nuclides." `http://www.nndc.bnl.gov/chart/`. Accessed: 03-17-2015.

[6] R. Boyd, *An Introduction to Nuclear Astrophysics*. University of Chicago Press, 2007.

[7] J. José and C. Iliadis, "Nuclear astrophysics: the unfinished quest for the origin of the elements," *Reports on Progress in Physics*, vol. 74, p. 096901, Sept. 2011.

[8] C. Iliadis, *Nuclear Physics of Stars*. Wiley-VCH, 1 2008.

[9] D. W. Savin, N. S. Brickhouse, J. J. Cowan, R. P. Drake, S. R. Federman, G. J. Ferland, A. Frank, M. S. Gudipati, W. C. Haxton, E. Herbst, S. Profumo, F. Salama, L. M. Ziurys, and E. G. Zweibel, "The impact of recent advances in laboratory astrophysics on our understanding of the cosmos," *Reports on Progress in Physics*, vol. 75, no. 3, p. 036901, 2012.

[10] E. M. Burbidge, G. R. Burbidge, W. A. Fowler, and F. Hoyle, "Synthesis of the Elements in Stars," *Reviews of Modern Physics*, vol. 29, pp. 547–650, 1957.

[11] CHANDRA X-ray Observatory Website, "Stellar Evolution." `http://chandra.harvard.edu/edu/formal/stellar_ev/`. Accessed: 03-17-2015.

[12] A. Parikh, J. José, G. Sala, and C. Iliadis, "Nucleosynthesis in type I X-ray bursts," *Progress in Particle and Nuclear Physics*, vol. 69, pp. 225–253, Mar. 2013.

[13] Georgia Institute of Technology News Center. `http://www.news.gatech.edu/2014/09/19/thermonuclear-x-ray-bursts-neutron-stars-set-speed-record`. Accessed: 03-17-2015.

[14] W. Bloemendal and C. Kramer, "The Netherlands astronomical satellite (ANS).," *Philips Technical Review*, vol. 33, pp. 117–129, 1973.

[15] List of 109 Galactic Type-I X-ray bursters. `https://personal.sron.nl/~jeanz/bursterlist.html`. Accessed: 03-17-2015.

[16] S. E. Woosley and R. E. Taam, "Gamma-ray bursts from thermonuclear explosions on neutron stars," *Nature*, vol. 263, pp. 101–103, Sept. 1976.

[17] A. Parikh, J. José, C. Iliadis, F. Moreno, and T. Rauscher, "Impact of uncertainties in reaction Q values on nucleosynthesis in type I x-ray bursts," *Physical Review C*, vol. 79, p. 045802, Apr. 2009.

[18] R. K. Wallace and S. E. Woosley, "Explosive hydrogen burning," *The Astrophysical Journal Supplement Series*, vol. 45, pp. 389–420, Feb. 1981.

[19] A. Parikh, J. José, and G. Sala, "Classical novae and type I X-ray bursts: Challenges for the 21st century," *AIP Advances*, vol. 4, p. 041002, Apr. 2014.

[20] A. E. Champagne and M. Wiescher, "Explosive hydrogen burning," *Annual Review of Nuclear and Particle Science*, vol. 42, pp. 39–76, 1992.

[21] L. van Wormer, J. Görres, C. Iliadis, M. Wiescher, and F.-K. Thielemann, "Reaction rates and reaction sequences in the rp-process," *The Astrophysical Journal*, vol. 432, pp. 326–350, Sept. 1994.

[22] H. Herndl, J. Görres, M. Wiescher, B. Brown, and L. van Wormer, "Proton capture reaction rates in the rp process," *Physical Review C*, vol. 52, pp. 1078–1094, Aug. 1995.

[23] H. Schatz, A. Aprahamian, J. Görres, M. Wiescher, T. Rauscher, J. F. Rembges, F.-K. Thielemann, B. Pfeiffer, P. Moeller, K.-L. Kratz, H. Herndl, B. Brown, and H. Rebel, "rp-Process Nucleosynthesis at Extreme Temperature and Density Conditions," *Physics Reports*, vol. 294, Feb. 1998.

[24] H. Schatz and K. E. Rehm, "X-ray binaries," *Nuclear Physics A*, vol. 777, pp. 601–622, Oct. 2006.

[25] J. L. Fisker, H. Schatz, and F.-K. Thielemann, "Explosive Hydrogen Burning during Type I X-Ray Bursts," *The Astrophysical Journal Supplement Series*, vol. 174, no. 1, p. 261, 2008.

[26] S. E. Woosley, A. Heger, A. Cumming, R. D. Hoffman, J. Pruet, T. Rauscher, J. L. Fisker, H. Schatz, B. A. Brown, and M. Wiescher, "Models for Type I X-Ray Bursts with Improved Nuclear Physics," *The Astrophysical Journal Supplement*, vol. 151, pp. 75–102, Mar. 2004.

[27] J. L. Fisker, F.-K. Thielemann, and M. Wiescher, "The Nuclear Reaction Waiting Points: ^{22}Mg, ^{26}Si, ^{30}S, and ^{34}Ar and Bolometrically Double-peaked Type I X-Ray Bursts," *The Astrophysical Journal Letters*, vol. 608, pp. L61–L64, June 2004.

[28] J. L. Fisker, J. Görres, M. Wiescher, and B. Davids, "The Importance of ^{15}O(α,γ)^{19}Ne to X-Ray Bursts and Superbursts," *The Astrophysical Journal*, vol. 650, pp. 332–337, Oct. 2006.

[29] A. M. Amthor, D. Galaviz, A. Heger, A. Sakharuk, H. Schatz, and K. Smith, "Sensitivity of Type I X-Ray Bursts to rp-Process Reaction Rates," *ArXiv Astrophysics e-prints*, Aug. 2006.

[30] L. F. Roberts, "Monte Carlo simulations of Type I X-ray burst nucleosyntheis," in *International Symposium on Nuclear Astrophysics - Nuclei in the Cosmos*, p. 202.1, 2006.

[31] M. Wiescher and H. Schatz, "Impact and perspectives of radioactive beam experiments for the rp-process," *Nuclear Physics A*, vol. 693, pp. 269–281, Oct. 2001.

[32] M. Wiescher, J. Gorres, F.-K. Thielemann, and H. Ritter, "Explosive hydrogen burning in novae," *Astronomy and Astrophysics*, vol. 160, pp. 56–72, May 1986.

[33] A. Parikh, J. José, F. Moreno, and C. Iliadis, "The Effects of Variations in Nuclear Processes on Type I X-Ray Burst Nucleosynthesis," *The Astrophysical Journal Supplement*, vol. 178, pp. 110–136, Sept. 2008.

[34] K. L. G. Heyde, *Basic ideas and concepts in nuclear physics: an introductory approach*, vol. Series in fundamental and applied nuclear physics. Institute of Physics Pub, 2004.

[35] I. J. Thompson and F. M. Nunes, *Nuclear Reactions for Astrophysics*. Cambridge University Press, 2009.

[36] N. Glendenning, *Direct Nuclear Reactions*. World Scientific, 2004.

[37] B. Sahu and S. Bhoi, "Potential for α -induced nuclear scattering, reaction and decay, and a resonance-pole-decay model with exact explicit analytical solutions," *Physical Review C*, vol. 96, p. 044602, Oct. 2017.

[38] F. Carstoiu and R. J. Lombard, "A new method of evaluating folding type integrals," *Annals of Physics*, vol. 217, pp. 279–303, Aug. 1992.

[39] L. Trache, A. Azhari, H. L. Clark, C. A. Gagliardi, Y.-W. Lui, A. M. Mukhamedzhanov, R. E. Tribble, and F. Carstoiu, "Optical model potentials involving loosely bound p-shell nuclei around 10 MeV/nucleon," *Physical Review C*, vol. 61, p. 024612, Feb. 2000.

[40] T. Al-Abdullah, F. Carstoiu, C. A. Gagliardi, G. Tabacaru, L. Trache, and R. E. Tribble, "Peripheral elastic and inelastic scattering of $O^{17,18}$ on light targets at 12 MeV/nucleon," *Physical Review C*, vol. 89, p. 064602, June 2014.

[41] J.-P. Jeukenne, A. Lejeune, and C. Mahaux, "Optical-model potential in finite nuclei from Reid's hard core interaction," *Physical Review C*, vol. 16, pp. 80–96, July 1977.

[42] E. Bauge, J. P. Delaroche, and M. Girod, "Semimicroscopic nucleon-nucleus spherical optical model for nuclei with A$\geq$40 at energies up to 200 MeV," *Physical Review C*, vol. 58, pp. 1118–1145, Aug. 1998.

[43] N. Anantaraman, H. Toki, and G. F. Bertsch, "An effective interaction for inelastic scattering derived from the Paris potential," *Nuclear Physics A*, vol. 398, pp. 269–278, Apr. 1983.

[44] A. M. Mukhamedzhanov, R. P. Schmitt, R. E. Tribble, and A. Sattarov, "Asymptotic normalization coefficients for $^{10}\mathrm{B}\rightarrow{}^{9}\mathrm{Be}$+*p*," *Physical Review C*, vol. 56, pp. 1302–1312, Sep 1997.

[45] C. Bertulani and P. Danielewicz, *Introduction to nuclear reactions*. IOP, 2004.

[46] D. Pringle, W. Catford, J. Winfield, D. Lewis, N. Jelley, K. Allen, and J. Coupland, "The oxford mdm-2 magnetic spectrometer," *Nuclear Instruments and Methods in Physics Research Section A*, vol. 245, no. 2, pp. 230 – 247, 1986.

[47] S. Kowalski and H. A. Enge, *computer code RAYTRACE (unpublished)*. University of Oxford, England, UK, 1986.

[48] A. M. Mukhamedzhanov, R. P. Schmitt, R. E. Tribble, and A. Sattarov, "Astrophysical factor for the radiative capture reaction $\alpha + d \rightarrow {}^{6}\mathrm{Li} + \gamma$," *Physical Review C*, vol. 52, pp. 3483–3487, Dec 1995.

[49] A. M. Mukhamedzhanov, A. Azhari, V. Burjan, C. A. Gagliardi, V. Kroha, A. Sattarov, X. Tang, L. Trache, and R. E. Tribble, "Astrophysical *S* factor $\mathrm{for}{}^{13}\mathrm{C}(p,\gamma)^{14}\mathrm{N}$ and asymptotic normalization coefficients," *Physical Review C*, vol. 66, p. 027602, Aug 2002.

[50] R. Tribble, A. Azhari, P. Bem, V. Burjan, F. Carstoiu, C. Gagliardi, V. Kroha, A. Mukhamedzhanov, J. Novák, F. Pirlepesov, Š. Piskoř, A. Sattarov, E. Šimecková, X. Tang, L. Trache, and J. Vincour, "New results for ${}^{8}\mathrm{B}(p,\gamma)^{9}\mathrm{C}, {}^{11}\mathrm{C}(p,\gamma)^{12}\mathrm{N}, {}^{13}\mathrm{C}(p,\gamma)^{14}\mathrm{N}\,\mathrm{and}\,{}^{14}\mathrm{N}(p,\gamma)^{15}\mathrm{O}$ at stellar energies," *Nuclear Physics A*, vol. 718, pp. 147 – 150, 2003.

[51] O. Bunemann, T. E. Cranshaw, and J. A. Harvey, "Design of grid ionization chambers," *Canadian Journal of Research*, vol. 27(A), pp. 191–206, 1949.

[52] C. Grupen and B. Shwartz, *Particle Detectors*. Cambridge University Press, 2008.

[53] P. S. Morrall, "Target preparation method and characterisation," *Nuclear Instruments and Methods in Physics Research A*, vol. 613, pp. 423–424, 2010.

[54] O. B. Tarasov and D. Bazin, "LISE++ : Exotic beam production with fragment separators and their design," *Nuclear Instruments and Methods in Physics Research B*,

vol. 266, p. 4457, 2008.

[55] J. F. Ziegler, M. D. Ziegler, and J. P. Biersack, "SRIM - The stopping and range of ions in matter (2010)," *Nuclear Instruments and Methods in Physics Research B*, vol. 268, pp. 1818–1823, June 2010.

[56] F. Carstoiu, "computer code OPTIMINIX (unpublished)," 1996.

[57] M. Rhoades-Brown, S. Pieper, and M. Macfarlane, "computer code PTOLEMY," *Argonne National Lab Report*, vol. 9, 1978.

[58] I. J. Thompson, "Getting started with FRESCO." `http://www.fresco.org.uk/guide/fresco-starting.html`. Accessed: 03-17-2015.

[59] L. Trache, A. Azhari, F. Carstoiu, H. L. Clark, C. A. Gagliardi, Y.-W. Lui, A. M. Mukhamedzhanov, X. Tang, N. Timofeyuk, and R. E. Tribble, "Asymptotic normalization coefficients for ^{8}B $\rightarrow$ ^{7}Be+p from a study of ^{8}Li $\rightarrow$ ^{7}Li+n," *Physical Review C*, vol. 67, p. 062801, June 2003.

[60] C. A. Bertulani, "RADCAP: A potential model tool for direct capture reactions," *Computer Physics Communications*, vol. 156, pp. 123–141, Dec. 2003.

[61] C. Wrede, J. A. Clark, C. M. Deibel, T. Faestermann, R. Hertenberger, A. Parikh, H.-F. Wirth, S. Bishop, A. A. Chen, K. Eppinger, B. M. Freeman, R. Krücken, O. Lepyoshkina, G. Rugel, and K. Setoodehnia, "Properties of ^{20}Na, ^{24}Al, ^{28}P, ^{32}Cl, and ^{36}K for studies of explosive hydrogen burning," *Physical Review C*, vol. 82, p. 035805, Sept. 2010.

APPENDIX A

COMPUTER CODES

This Appendix contains sample input files for the different codes that were used in the analysis of this study.

A.1 The RAYTRACE Code

```
MDM 13C+27Al @6.0 deg Bhall=6205.5 R10-14 transfer channel
    RAYTRACE
      7   206     1     2     3     0     0
  153.65      2.0          0.          12.001          6.
DRIF
  57.0
COLL
0.0           0.0          0.0         3.              3.
DRIF
  18.075
POLE input multipole (use Bronson calibration of Bhall)
  1.          3.           1.
  1.925       113.2        26.         6.5
-0.33290    0.02477    0.0182     -0.01462   -0.0124    Bq=
    6205.5*1.034
  20.         -10.         -10.        20.
  .1122        6.2671    -1.4982   3.5882      -2.1209   1.723
  .1122        6.2671    -1.4982   3.5882      -2.1209   1.723
```

```
 1.          1.          1.          1.          1.          1.
             1.          1.
DIPO    (Bd=1.034*Bnmr   Bnmr=Bhall)
 1.          6.          1.          1.          3.          60.
            0.
 26.         32.55       11.5        160.        0.64165
 100.        0.          0.
 0.191       -0.04       0.          0.
 46.         -33.        -23.        50.
 .048        3.70        .0125       -.299       .016        .020
            Jeffs frng 800amp
 .048        3.70        .0125       -.299       .016        .020
            Jeffs frng 800amp
 0.          0.          0.          0.          0.          0.
 0.          0.
 1.242       -3.11       4.142       -1.06       0.          0.
             0.          Drawing ent
 -1.579      1.719       -13.43      -24.58      779.35      821.26
         -21410.    Drawing Exit
MULT (L=35 cm 9/7/93)
 1.          2.          0.
 0.2          1.5        35.0        60.         9.6         1.0
 -32.5       32.5
 0.          0.           0.0         0.0        0.          0.
 0.          1.          1.
```

```
COLL
  0.        -0.08        0.          29.61      20.21
DRIF
  63.0
SENT
    6.00      0.000      13.003       26.9815    2.779     0.0000
              7.
   3.00     4.47    5.235     6.00    6.765     7.53     9.00
```

A.2 The OPTIMINIX Code

Fitting the elastic distribution

```
 0 0 0 7 1 0        ! iter,ism,ipot,niter,iordin,imini
13.          6.     ! proj mass and charge
27.         13.     ! targ mass and charge
154.                ! Elab
120.                ! Lmax
0.1        251.     ! H,NPTS1
0.00   0.000  0.00  ! V,Rv,Av
0.00   0.000  0.00  ! W,Rw,Aw
1.000               ! Rc
0.                  ! absolute cs values
48.                 ! Ex1 nr of points
1.                  ! Procent (=0 absolute errors )
*data follow bellow in 3 columns:
angle cross-section error
```

Plotting the elastic distribution

```
1 0 0 0 3 1          ! iter,ism,ipot,niter,iordin,imini
27.        13.       ! proj mass and charge
13.        6.        ! targ mass and charge
318.77               ! Elab
120.                 ! Lmax
0.1      251.        ! H,NPTS1
27.00  0.9783  1.0068   ! V,Rv,Av
23.72  1.1039  0.6958   ! W,Rw,Aw
1.000                ! Rc
1.                   ! Ratio to Rutherford
0.                   ! Ex1 – nr of data points
1. 0.1 430                  ! ang0 step nrangs
0.                   ! Procent (=0 absolute errors )
```

A.3 The PTOLEMY Code

Calculating wave-functions

```
HEADER  bound states calc. for 27Al+n ->28Al 2s1/2 radial
    wf.
CHANNEL: N + 27AL = 28AL


L=0 NODES=1 JP=1/2 SP=1/2
V=55 R0=1.15 VSO=4.65 A=0.60 RC0=1.2
ASYMPTOPIA=50
BOUNDSTATE
```

;

WRITESTEP=0.1

PRINTWAV

WRITENS PHI1

RETURN

DWBA calculations

HEADER: 27AL(13C,12C)28AL for Run0313 exp 13C on 27AL 12 MeV/n

REACTION 27AL(13C,12C)28AL ELAB=154.15

PARAMETERSET ALPHA2

USEPROJECTILE

LMIN=0

TARGET L=0 NODES=1 JP=1/2 SP=1/2

V=55 R0=1.15 VSO=4.65 A=0.60 RC0=1.2

ASYMPTOPIA=20

WRITESTEP= 0.1

;

PROJECTILE L=1 NODES=0 JP=1/2 SP=1/2

V=55 R0=1.15 VSO=4.65 A=0.60 RC0=1.2

ASYMPTOPIA=20

;

```
INCOMING
V=106.0 R0=0.8457 A=0.4791 VI=10.49 RI0=1.3223 AI=0.8347 ;

OUTGOING
V=106.0 R0=0.8457 A=0.4791 VI=10.49 RI0=1.3223 AI=0.8347 ;

ANGLEMIN=0 ANGLEMAX=60 ANGLESTEP=0.25
;
WRITENS CROSSSEC
RETURN
```

A.4 The RADCAP Code

Module 2:EIGEN

```
*****************************************************
*     ********     Input of subroutine EIGEN    *******
*
*                  ******* 28P 2s1/2 here ******
*
* IOPT  = option for potentials: 1 (2) for Woods-Saxon (M3Y
    )
* NPNTS = no. of integration points in radial coordinate (
    < 10000)
* RMAX  = maximum radius size (< 250 fm).
*
* IOPT      NPTS      RMAX
*
```

```
  1         9999      250.
*
* N_0  =  nodes of the Wave Function (exclude origin)
* J0   =  single-particle angular momentum
* L0   =  orbital angular momentum
*
* N_0     J_0       L_0
*
  1        0.5        0
*
* If IOPT = 1, enter:
* V0  =  depth of central pot.
* VS0 =  depth of spin-orbit potential
* R0  =  radius of the potential
* AA  =  diffuseness of the pot.
* RS0 =  radius of the spin-orbit pot.
* AAS =  diffuseness of the spin-orbit pot.
* RC  =  Coulomb radius (usually, RC = R0)
*-----------------------------------------------------------
*  WS =  V_0 f(r,R0,AA) - V_S0 (l.s) (r_0^2/r) d/dr f(r,RS0
   ,AAS)
*
*  f(r,R0,a) = [ 1 + exp((r-R_0)/a) ]^(-1)
*
*  r_0 = 1.4138 fm is the Compton wavelength of the pion.
```

```
*-------------------------------------------------------
* V0          R0          AA        VS0       RS0       AAS       RC
*
-55.949     3.45        0.60      -4.65     3.45      0.60      3.6
*
* If IOPT = 2, or else (but not 1), enter FC, FSO and RC:
*     (in this case, insert a '*' sign in above row, or
   delete it)
* FC        = multiplicative factor of central part of M3Y
   potential
* FSO       = multiplicat. factor of spin-orbit part of M3Y
   potential
* RC        =  Coulomb radius
*
*  FC          FSO         RC
*    1.5         0.2         2.391
*
* Z1, Z2   =  charges of the nuclei
* A1, A2   =  masses of the nuclei (in nucleon mass units)
*
* Z1        A1        Z2        A2
*
    1.        1.        14.       27.
*
**************************************************
```

Module 5:DICAP

```
************************************************
*    ********     Input of program DICAP  ****
*                *****  27si+p=28P  *****
*
* IOPT   = option for potentials: 1 (2) for Woods-Saxon (
   M3Y)
* NPNTS = no. of integration points in radial coordinate (
   < 10000)
* RMAX = maximum radius size (< 250 fm).
* NEPTS = number of points in energy ( < 1000)
*
* IOPT     NPNTS     RMAX      NEPTS
*
  1        9999      250.       199
*
* N_0  =  nodes of the G.S. wave function
* AIA  =  spin of the particle A (core)
* AIB  =  intrinsic spin of the particle B
* AIC  =  total angular momentum of the ground state of C =
    A + B - (channel spin)
* J0   =  single-particle angular momentum
* L0   =  orbital angular momentum
* EBOUND = binding energy of the ground state (absolute
   value)
```

```
*
* N_0     AIA       AIB       AIC       AJ0       L_0       EBOUND
*
  1         2.5       0.5       3         0.5       0         2.052
*
* JOPT = 1 (0) if final state ang. mom., AICF, is (is not)
   to be
*         summed over all possible values. If JOPT=1, AICF
   can be
*         entered as any value.
* AICF =  spin of the excited state after all ang. mom.
   coupling
*
* JOPT      AICF
*
  1          1.
*
* Z1, Z2 = charges of the nuclei
* A1, A2 = masses of the nuclei (in nucleon mass units)
*
* Z1        A1       Z2       A2
*
    1.       1.       14.      27.
*
* V0   =  depth of central potential
```

```
* R0   =  radius of the central potential
* AA   =  diffuseness of the central potential
* VS0  =  depth of spin-orbit potential
* RS0  =  radius of the spin-orbit potential
* AAS  =  diffuseness of the spin-orbit potential
* RC   =  Coulomb radius (usually, RC = R0)
*-----------------------------------------------------------------
*  WS  =  V_0 f(r,R0,AA) - V_S0 (l.s) (r_0^2/r) d/dr f(r,
   RS0,AAS)
*
*  f(r,R0,a) = [ 1 + exp((r-R_0)/a) ]^(-1)
*
*  r_0 = 1.4138 fm is the Compton wavelength of the pion.
*-----------------------------------------------------------------
* V0          R0        AA       VS0       RS0       AAS       RC
*
-55.949    3.45      0.60     -4.65    3.45     0.60    3.6
*
* If IOPT = 2, or else (but not 1), enter FC, FSO and RC:
*    (in this case, insert a '*' sign in above row, or
   delete it)
* FC       = multiplicative factor of central part of M3Y
   potential
* FSO      = multiplicat. factor of spin-orbit part of M3Y
   potential
```

```
* RC       =  Coulomb radius
*
*  FC          FSO         RC
*    1.5         0.2         2.391
*
* EI,EF =  initial relative energy, final relative energy
*
* EI         EF
*
   0.01        2.0
*
* NS1,NP1,NP3,ND3,ND5,NF5,NF7 = (1) [0] for  inclusion [no
    inclusion]
*      of  s1/2, p1/2, p3/2, d3/2, d5/2, f5/2, and f7/2
    partial waves
*
*  NS       NP1       NP3       ND3      ND5      NF5      NF7
*
   0         1         1         0        0        1        1
*
* MP   = multipolarity: 0 (M1),  1 (E1),   2 (E2)
* SF   = Spectroscopic factor
*
*  MP          SF
*
```

```
    1           1.
*
* GA  = magnetic moment (in units of the nuclear magneton)
    of
*          particle A (core)
* GB  = magnetic moment of particle B (proton, neutron,
    alpha, etc.)
*
*    GA            GB
*
      -1.7          5.58
*
*****************************************************
```